

LIBRARIES MICHIGAN STATE UNIVERSITY EAST LANSING, MICH 48824-1048

) 9^M 11159180

This is to certify that the thesis entitled

Numerical Simulations of Partially Premixed Methane Combustion in Laminar and Turbulent Flows

presented by

Hyderuddin Mohammad

has been accepted towards fulfillment of the requirements for the

M.S.	degree in _	Mechanical Engineering		
Major Professor's Signature				
/2//7/04				
		Date		

MSU is an Affirmative Action/Equal Opportunity Institution

PLACE IN RETURN BOX to remove this checkout from your record. TO AVOID FINES return on or before date due. MAY BE RECALLED with earlier due date if requested.

DATE DUE	<u>DATE DUE</u>	<u>DATE DUE</u>
-		

6/01 c:/CIRC/DateDue.p65-p.15

Numerical Simulations of Partially Premixed Methane Combustion in Laminar and Turbulent Flows

By

Hyderuddin Mohammad

A THESIS

Submitted to
Michigan State University
in partial fulfillment of the requirements
for the degree of

MASTER OF SCIENCE

Department of Mechanical Engineering

2004

ABSTRACT

Numerical Simulations of Partially Premixed Methane Combustion in Laminar and Turbulent Flows

By

Hyderuddin Mohammad

The effects of partial premixing of methane fuel with air on the structure of a laminar counterflow flame were studied via various reduced and full chemistry models. Our results indicate that the mechanisms containing both the C_1 and C_2 species perform much better than those involving only C_1 species. Results obtained with the 10-step and 12-step mechanisms compare very well with those of the full GRI mechanisms for all the values of strain rate and premixing, and generate the same ignition and extinction characteristics in all simulated flames. However, the mechanisms with lesser number of species such as the 4-step, 5-step and 6-step perform well in some of the conditions, they were not fully accurate. The performance of these reaction mechanisms were found to deteriorate as the strain rate is decreased or the level of fuel premixing with air is increased.

The 10-step mechanism was used in a direct numerical simulation (DNS) of isotropic turbulent flow interacting with non-premixed and partially-premixed flames. DNS data were used to understand the behavior of the flames in more realistic flow situations. Our results show significant changes in the flame structure embedded in a high intensity turbulent field due to the imposed variable strain field. Deviation from the initial (laminar) flame structure in compositional space has been observed and was accompanied with significant local extinction at the locations where the strain rate was high. At early times, significant vorticity dissipation was observed due to volumetric expansion and increased viscosity near the flame. In the later times, vorticity was generated by the so called baroclinic term near the flame.

Copyright © by
Hyderuddin Mohammad
2004

To my parents and my brother

ACKNOWLEDGEMENTS

I would like to express my gratitude to my thesis advisor Dr. Farhad A. Jaberi for his constant support and brilliant guidance. He sincerely dedicated his time and effort to help me accomplish my goal. Without his incessant encouragement and appreciation this thesis would not be 'complete' in its true sense.

This work was sponsored by the office of Naval Research under Grant N00014-01-1-0843 and National Science Foundation. I am thankful to them for their support. I am also thankful to Dr. Gabriel D. Roy of the office of Naval Research for his continuous support and encouragement during the course of this research.

I would also like to thank my committee members, Dr. Z. J. Wang and Dr. Mei Zhuang, and Dr. Indrek Wichman. They took their time out of their busy schedule and gave me insightful comments and suggestions. I would also like to thank Dr. Sunil James, Mr. Bharatwaj, and Mr. Kian for their valuable help throughout my research.

Most importantly, I would like to thank my parents, brother and my sisters for their love and unconditional support throughout my life. I am grateful to my friends for their help and sharing memorable times during my stay at Michigan State University.

TABLE OF CONTENTS

L	ST (OF TA	BLES	viii
Ll	ST (OF FIG	GURES	ix
1	Lan	ninar I	Flames	1
	1.1	Introd	luction	. 1
	1.2	Mathe	ematical and Numerical Formulation	. 7
		1.2.1	Equations for Gaseous Combustion	. 7
		1.2.2	Flamelet Formulation	. 11
		1.2.3	Counterflow Flames	. 14
		1.2.4	Numerical Method	. 17
	1.3	Result	ts and Discussion	. 19
		1.3.1	Temperature Field	. 20
		1.3.2	Species Field	. 24
		1.3.3	Autoignition	. 30
2	Tur	bulent	Flames	64
	2.1	Introd	luction	. 64
	2.2	Gover	rning Equations for Reacting Flows	. 69
		2.2.1	Conservation Equations	. 69
		2.2.2	Transport Models	. 72
		2.2.3	Chemistry Models	. 75
	2.3	Nume	erical Solution	. 78
		2.3.1	Methodology	. 79
		2.3.2	Simplifying Assumptions	. 80

	2.4	Simula	ations	86
		2.4.1	Initialization	86
		2.4.2	Results	89
3	Con	clusion	ns	120
ві	BIBLIOGRAPHY 124			124

LIST OF TABLES

1.1	Reaction Mechanisms Assessed	19
2.1	Characteristic scales in turbulent non-premixed flames	66
2.2	Differencing sequence foe wxtended Maccormack scheme	79
2.3	CPU time requirements for subroutines before and after approximation	82
2.4	Percentage of CPU time in stress subroutine	83
2.5	Characteristics of developed turbulence field	87
2.6	Dimensional characteristics of turbulence fields	88
2.7	Simulation cases studied	88

LIST OF FIGURES

1.1	Temperature structures in physical and compositional space for various domain sizes, (a) 0.4 cm, (b) 1.0 cm, (c) 2.0 cm	33
1.2	Temperature structure in mixture fraction space with GRI-Mech 2.11 (a) for different strain rates and premixing of 75% air in the fuel stream, (b) for different premixing levels of the fuel stream and strain of $25(1/s)$. Vertical lines indicate stoichiometric mixture fraction	34
1.3	Compositional temperature structure obtained with various mechanisms for 75% premixing of fuel stream and different strain rates, (a) 10 (1/s) (b) 50 (1/s) (c) 150 (1/s) (d) 300 (1/s). Vertical lines indicate the stoichiometric mixture fraction	35
1.4	Compositional temperature structure obtained with different mechanisms for different premixing of fuel stream and a strain rate of 25 (1/s), (a) 0% (b) 25% (c) 50% (d) 75%. Vertical lines indicate the stoichiometric mixture fraction	36
1.5	Production rates of CH_4, O_2 , and CO_2 . (a) 5-step mechanism	37
1.5	[contd] Production rates of CH_4, O_2 , and CO_2 . (b) 10-step mechanism.	38
1.6	Percentage mean of temperature difference from GRI 3.0 for different mechanisms vs. (a) strain rate for premixing of 75% air in fuel stream, (b) premixing level of fuel stream with air for strain rate of 25(1/s).	39
1.7	Maximum temperature deviation from GRI 3.0 predictions for different mechanisms and a strain of 25 (1/s)	40
1.8	Temperature difference from GRI 3.0 for different mechanisms vs. mixture fraction for strain rate of 25(1/s) and (a) 75% air in the fuel stream, (b) 85% air in the fuel stream	41
1.9	Effect of partial premixing on Y_{CH_4} structure. $-\diamondsuit-$, 4-Step; $-\times-$, 5-Step; $-*-$, 6-Step; $-\triangle-$, 10-Step; $-\Box-$, 12-Step; $-\bigcirc-$, GRI 2.11; $-\bigstar-$, GRI 3.0	42

[contd] Effect of strain rate on Y_{CH_4} structure. See Figure 1.9(a) for labeling	43
Effect of partial premixing on Y_{O_2} structure. See Figure 1.9(a) for labeling. Vertical lines indicate the stoichiometric mixture fraction	44
[contd] Effect of strain rate on Y_{O_2} structure. See Figure 1.9(a) for labeling. Vertical lines indicate the stoichiometric mixture fraction	45
Reaction rate of the global reactions in (a) 4-step mechanism	46
[contd] Reaction rate of the global reactions in (b) 5-step mechanism.	47
Effect of partial premixing on Y_{CO_2} structure. See Figure 1.9(a) for labeling. Vertical lines indicate the stoichiometric mixture fraction	48
[contd] Effect of strain rate on Y_{CO_2} structure. See Figure 1.9(a) for labeling. Vertical lines indicate the stoichiometric mixture fraction	49
Effect of partial premixing on Y_{H_2} structure. (a) $A\% = 0$, (b) $A\% = 25$, (c) $A\% = 50$, and (d) $A\% = 75$. See Figure 1.9(a) for labeling. Vertical lines indicate the stoichiometric mixture fraction	50
[contd] Effect of strain rate on Y_{H_2} structure. (a) strain = 10 1/s, (b) strain = 50 1/s, (c) strain = 150 1/s, and (d) strain = 300 1/s. See Figure 1.9(a) for labeling. Vertical lines indicate the stoichiometric mixture fraction	51
Effect of partial premixing on Y_{CO} structure. See Figure 1.9(a) for labeling. Vertical lines indicate the stoichiometric mixture fraction	52
[contd] Effect of strain rate on Y_{CO} structure. See Figure 1.9(a) for labeling. Vertical lines indicate the stoichiometric mixture fraction	53
CO_2 production rate and mass fraction compared for 0% partial premixing and a strain rate of 25 1/s 4-step mechanism	54
[contd] CO_2 production rate and mass fraction compared for 0% partial premixing and a strain rate of 25 1/s 5-step mechanism	55
Effect of partial premixing on Y_H structure. (a) $A\% = 0$, (b) $A\% = 25$, (c) $A\% = 50$, and (d) $A\% = 75$. See Figure 1.9(a) for labeling. Vertical lines indicate stoichiometric mixture fraction	56
(b) strain = 50 1/s, (c) strain = 150 1/s, and (d) strain = 300 1/s. See Figure 1.9(a) for labeling. Vertical lines indicate stoichiometric	57
	Effect of partial premixing on Y_{O_2} structure. See Figure 1.9(a) for labeling. Vertical lines indicate the stoichiometric mixture fraction

1.17	Effect of partial premixing on Y_{NO} structure. $-\times$ -, 5-Step; $-\bigcirc$ -, GRI 2.11; $-\bigstar$ -, GRI 3.0. (a) $A\% = 0$, (b) $A\% = 25$, (c) $A\% = 50$, and (d) $A\% = 75$. Vertical lines indicate stoichiometric mixture fraction 5	
1.17	[contd] Effect of strain rate on Y_{NO} structure. $-\times$ -, 5-Step; $-\bigcirc$ -, GRI 2.11; $-\bigstar$ -, GRI 3.0. (a) strain = 10 1/s, (b) strain = 50 1/s, (c) strain = 150 1/s, and (d) strain = 300 1/s. Vertical lines indicate stoichiometric mixture fraction	59
1.18	(DF) vs. strain rate for different mechanisms and premixing of 75% air in fuel stream. (a) CH_4 , (b) CO	60
1.19	(DF) vs. partial premixing level of fuel with air for different mechanisms and strain rate of $25(1/s)$. (a) CH_4 , (b) CO	61
1.20	Maximum Y_{CO} difference between the GRI 3.0 results with those obtained with other mechanisms	62
1.21	Ignition temperature vs. strain rate for various premixing levels of the fuel with air using GRI 3.0	63
2.1	Combustion regimes for non-premixed flame	65
2.2	Computational Domain	78
2.3	Sequence of temperature contours for turbulence case I and flame No. 3 with time; (a) $t/\tau_t=0.0$, (b) $t/\tau_t=1.0$, (c) $t/\tau_t=1.5$, (d) $t/\tau_t=2.0$.	95
2.4	Mixture Fraction contours for turbulence case I and flame No. 3 with time: (a) $t/\tau_t=0.0$ (b) $t/\tau_t=1.0$ (c) $t/\tau_t=1.5$ (d) $t/\tau_t=2.0$	96
2.5	Y_{OH} contours for turbulence case I and flame No. 3 with time: (a) $t/\tau_t=0.0$ (b) $t/\tau_t=1.0$ (c) $t/\tau_t=1.5$ (d) $t/\tau_t=2.0$	97
2.6	Y_{CO} contours for turbulence case I and flame No. 3 with time: (a) $t/\tau_t=0.0$ (b) $t/\tau_t=1.0$ (c) $t/\tau_t=1.5$ (d) $t/\tau_t=2.0$	98
2.7	Y-averaged plots at different times for (a) Temperature and (b) Y_{OH} .	99
2.8	Flame normal analysis at a burning region of the flame (a) Mixture fraction contours showing the line of section (b) Temperature (c) Strain rate	100
2.9	Flame normal analysis at a about-to-be-quenched region of flame and for $t/\tau_t = 1.0$ (a) Mixture fraction contours showing the line of section (b) Temperature (c) Strain rate	101

2.10	Flame normal analysis at a quenched region of flame and for $t/\tau_t = 1.5$ (a) Mixture fraction contours showing the line of section (b) Temperature (c) Strain rate	102
2.11	Scatter plots in mixture fraction space for turbulence case I and flame No. 1 at one eddy turn-over time. (a) Temperature (b) Y_{CO} (c) Y_{OH} (d) Y_H . Dashed lines shows the initial laminar profile	103
2.12	Scatter plots in mixture space for turbulence case I and flame No. 2 at one eddy turn-over time. (a) Temperature (b) Y_{CO} (c) Y_{OH} (d) Y_{H} . Dashed lines shows the initial laminar profile	104
2.13	Scatter plots in mixture fraction space for turbulence case I and flame No. 3 at one eddy turn-over time. (a) Temperature (b) Y_{CO} (c) Y_{OH} (d) Y_H . Dashed lines shows the initial laminar profile	105
2.14	Temperature scatter plots for turbulence case I and flame No. 3 for (a) $t/\tau_t = 0.0$ (b) $t/\tau_t = 1.0$ (c) $t/\tau_t = 1.5$ (d) $t/\tau_t = 2.0$ in mixture fraction space. Dashed line shows the initial laminar profile	106
2.15	Y_{OH} scatter plots for turbulence case I and flame No. 3 for, (a) $t/\tau_t = 0.0$, (b) $t/\tau_t = 1.0$, (c) $t/\tau_t = 1.5$, (d) $t/\tau_t = 2.0$ in mixture fraction space. Dashed line is the initial laminar profile	107
2.16	Y_{CO} scatter plots for turbulence case I and flame No. 3 for (a) $t/\tau_t = 0.0$, (b) $t/\tau_t = 1.0$, (c) $t/\tau_t = 1.5$, (d) $t/\tau_t = 2.0$ in mixture fraction space. Dashed line is the initial laminar profile	108
2.17	Sequence of vorticity images for turbulence case I and flame No. 3 with time: (a) $t/\tau_t=0.0$, (b) $t/\tau_t=1.0$, (c) $t/\tau_t=1.5$, (d) $t/\tau_t=2.0$	109
2.18	Sequence of enstrophy images for turbulence case I and flame No. 3 with time: (a) $t/\tau_t=0.0$, (b) $t/\tau_t=1.0$, (c) $t/\tau_t=1.5$, (d) $t/\tau_t=2.0$	110
2.19	Sequence of turbulent kinetic energy images for turbulence case I and flame No. 3 with time: (a) $t/\tau_t = 0.0$, (b) $t/\tau_t = 1.0$, (c) $t/\tau_t = 1.5$, (d) $t/\tau_t = 2.0$	111
2.20	Sequence of strain rate images for turbulence case I and flame No. 3 with time: (a) $t/\tau_t=0.0$, (b) $t/\tau_t=1.0$, (c) $t/\tau_t=1.5$, (d) $t/\tau_t=2.0$	112
2.21	Y-averaged vorticity plots at four eddy turn-over times. (a) $t/\tau_t=0$, (b) $t/\tau_t=1.0$, (c) $t/\tau_t=1.5$, and (d) $t/\tau_t=2.0$	113
2.22	Y-averaged enstropy plots at four eddy turn-over times. (a) $t/\tau_t = 0$, (b) $t/\tau_t = 1.0$, (c) $t/\tau_t = 1.5$, and (d) $t/\tau_t = 2.0$	114

2.23	Sequence of vorticity images for turbulence case I and flames of various premixing levels. (a) Initial vorticity, (b) $A\% = 0 \& t/\tau_t = 1.0$, (c) $A\% = 25 \& t/\tau_t = 1.0$, (d) $A\% = 75 \& t/\tau_t = 1.0$	115
2.24	Sequence of enstrophy images for turbulence case I and flames of various premixing levels. (a) Initial enstrophy, (b) $A\% = 0 \& t/\tau_t = 1.0$, (c) $A\% = 25 \& t/\tau_t = 1.0$, (d) $A\% = 75 \& t/\tau_t = 1.0$	116
2.25	Sequence of turbulent kinetic energy images for turbulence case I and flames of various premixing levels. (a) Initial TKE, (b) A% = 0 & $t/\tau_t=1.0$, (c) A% = 25 & $t/\tau_t=1.0$, (d) A% = 75 & $t/\tau_t=1.0$	117
2.26	Y-averaged vorticity for different partial premixing. (a) Initial profile, and (b) At $t/\tau_t=1.0.\ldots$.	118
2.27	Y-averaged enstrophy for different partial premixing. (a)Initial profile, and (b) At $t/\tau_t=1.0.\ldots$	119

CHAPTER 1

Laminar Flames

1.1 Introduction

Many of the applications, where combustion occurs, involve turbulent flow in a complex geometry. Turbulent flow analysis which is itself computationally expensive will be much more expensive with the inclusion of combustion with detailed chemical kinetics model. To circumvent the problems arising in numerical simulations of such flows, researchers have either resorted to generic description of combustion or to the simplified geometries so that the total number of numerical operations become manageable. While the former is prone to serious errors due to the empirical parameters [58] involved in global representation of the fuel combustion, the latter is a serious constraint in the study of realistic configurations.

Reduced chemistry models can be a remedy for the high computational cost problem. They reduce the computational effort in numerical calculations of flames by replacing a number of differential equations for intermediate species by algebraic relations. Apart from reducing the computational expense in numerical simulations, they allow studying the flame structure by asymptotic methods and by that help in identifying the important parameters that influence the global properties of the flame. Typically, a reduced mechanism is reduced from a skeletal mechanism,

which in turn is reduced from a full mechanism. The skeletal mechanism will be formed from the full mechanism by eliminating some of the reactions, which are not influential in predicting a solution (characteristic quantity of interest). Sensitivity analysis of the reactions in full mechanism can be performed to identify the reactions, which are not influential and thus to be eliminated.

Methods of reducing mechanisms were well-known to the chemists from long time especially, using partial equilibrium and steady state species eliminations. The potential of which was not realized until they were applied in reducing mechanisms for hydrocarbon fuel combustion. Since the work of Peters and Williams [40], many have come up with reduced mechanisms, which represent the combustion process in special situations. Even though such reduced mechanisms can represent combustion fairly well in the assumed situations, their performance can deteriorate in other conditions than the assumed. In practice, where there are lots of variations in the operating conditions, these chemistry models can perform poorly. Examples of the variations in conditions include lean and rich mixtures, premixed and non-premixed, various strain and pressure conditions, various levels of preheating of fuel and/or oxidizer. In a practical combustion system there exists a wide range of conditions at different locations in space of the same system. It is quite natural to question the applicability of the reduced mechanisms that are proposed for some simplified situations.

The discrepancy in the numerical simulation results and experimental results in turbulent reacting flows can be attributed to three factors: one is from the modeling of the unclosed terms, the second due to chemistry and transport models, and the third is the turbulence-chemistry interaction. The effects of initial/boundary conditions and numerical error can also be important. When comparing the results for practical combusting system, it is difficult to differentiate the discrepancy caused by each of the reasons individually. In this chapter the effect of chemistry and transport models of the different reduced reaction mechanisms of methane/air combustion will be studied in a simple geometry: laminar counter flow geometry. In

next chapter the effect of turbulence on methane flames and vice versa will be studied.

Counter-flow geometry has been widely used for the study of diffusion and partial premixed flames over the past three decades. It consists of an oxidizer jet (or stream) and a fuel jet (or stream) that are issued from two different nozzles opposing each other. A stagnation plane will be established in between the two nozzles at a place depending on the momentum of the two streams. This makes an interesting configuration to study the flame experimentally as a flat planar flame will be established between the two jets. Also the two-dimensional problem can be transformed into a one-dimensional problem which is easier to study analytically and numerically. Counterflow diffusion flame is ideal for studying chemistry models and molecular transport since the flame in this configuration often exhibits very similar scalar structure as "flamelets" in a turbulent flow field [35].

According to the laminar flamelet concept, the turbulent diffusion flame can be viewed as an ensemble of laminar diffusion flamelets. A steady laminar flamelet is a solution of steady one-dimensional diffusion reaction partial differential equations. The reaction zone is thin sheet near the stoichiometric value. A look-up library of laminar flamelet solutions can be generated and stored that can be used in simulations of turbulent combustion. Flamelet tables consists of the temperature, species profiles in mixture fraction space parameterized by mixture fraction dissipation rate at stoichiometric [35, 37].

The interest in flamelets is due to its importance in turbulent modeling of combustion. Liñán [29] studied the asymptotic structure of temperature for counterflow diffusion flames for one-step reaction with large activation energy and identified four regimes. In this classic study of high activation-energy asymptotics (AEA), it is predicted that the departure of the profiles from the equilibrium profiles is small for all the strains up to the extinction. AEA predicts significant fuel leakage through the reaction zone but negligible oxygen leakage as extinction is approached. This is

contrary to what has been observed in experiments and numerical results. According to AEA, in mixture fraction space the reactive-diffusive zone lies in between the two convective-diffusive zones. The one-step reaction that represents the combustion occurs in the reactive-diffusive zone.

It is always not possible that fuel and oxidizer are separated before burning in the turbulent field; sometimes fuel and oxidizer are mixed before they burn. Partial premixed flames are observed in non-premixed combustion at the base of lifted flame zone where the fuel and oxidizer are mixed before ignition. They are also observed when there is a local extinction and consequently mixing takes place without reaction. The partially premixed mode of burning produces less amount of pollutants, and hence it is a preferred mode of combustion. These situations can be modeled as an ensemble of laminar, partial premixed diffusion flamelets. Domingo et al. [17] have used partial premixed flamelets in simulation of non-premixed turbulent combustion using large eddy simulation.

Peters [36] analyzed the structure and extinction of partial premixed diffusion flamelets in initially unpremixed turbulent flows with a one-step irreversible reaction and large activation energy assumption. Situation where the local premixing occurs has been considered and the outer flame structure has been derived with a diffusion flame located around the stoichiometric mixture fraction and transition layers on rich and lean sides, which are characterized by premixed flame. When the Damkohler number is reduced the premixed regions merge with the diffusion flame and can lead to extinction because of increased sensitivity to flame stretch. And it was also shown that quenching couldn't occur in the diffusion flamelet as long as the transition layers are separated from it and thus, at extinction a merged flame structure develops.

Tanoff and Smooke [54] have also studied the structure of partially premixed flames in physical space for a wide range of fuel premixing and strain rates in methane-air vs. air counterflow flames. They observed that the structure of their

partially premixed flame changes rather significantly as the fuel stream premixing changes slightly around a critical equivalence ratio of $\phi = 1.5 - 1.4$. For $\phi > 1.5 - 1.4$, a single merged flame in the vicinity of stagnation plane was observed and for $\phi < 1.4$ a double flame consisting of a premixed flame and a diffusion flame is formed. The diffusion flame was formed primarily due to the oxidation of CO and the premixed flame mainly involves the oxidation of the fuel and the production of H_2 species. The exact value of the critical equivalence ratio was observed to be dependent on the strain rate - flames close enough to the extinction remained merged even at the lowest equivalence ratio.

Xue and Aggarwal [60] studied the effects of reaction mechanisms on the physical structure and the extinction characteristics of a partially-premixed methane-air flame over a range of strain rates and for different equivalence ratios. They considered the 12-step, GRI-Mechs 2.11 & 3.0, and C_1 and C_2 mechanisms of Peters and Rogg [39]. Premixed flame speed calculated using C_2 and GRI-2.11 were in good agreement with experimental results, whereas C_1 mechanism showed significant differences. Diffusion flame structure was found to be similar for all the mechanisms with some differences in the peak temperatures. Results for Partially premixed flames showed a quantitative disagreement for all the five mechanisms, though they were qualitatively similar, reproducing the double flame structure associated with these flames. Compared to C_1 mechanism C_2 was more sensitive to the equivalence ratio. Also for lower equivalence ratios the reaction zones merged more for C_2 mechanism than that for C_1 mechanism. Temperature gradients increased as the strain rates were increased. However, the extinction strain rates for partial premixed flames were higher for C_2 and GRI-Mech 2.11 mechanisms compared to those using C_1 mechanism. Xue et al. [61] compared the numerical results for temperature and species with the experimental data for moderate strain rates an found that the C₂ mechanism predictions are in better agreement with the experiment than those of GRI-Mech 3.0 mechanism.

Turbulent non-premixed or partial premixing combustion can be modeled using laminar flamelets. A flamelet library is compiled using the solutions of laminar counter-flow flames prior to the actual simulation of the complex flows. Full mechanisms can be utilized for these laminar flow calculations, since the computational requirement is not stringent. In turbulent simulations with finite rate chemistry reduced mechanisms are used due to the computational cost. A comparison of turbulent simulation results via these two methods will not differentiate the effects of chemistry and thus a simple configuration is chosen here, where there are no other modeling assumptions, to study the chemistry effects. In this present work a comprehensive study of various chemistry models for varying strain and partial premixing level of fuel stream with air will be done. The results of different reduced mechanisms will be compared to the prediction of "full" mechanism (GRI-Mech 3.0).

The organization of this chapter is as follows. First, the general governing equations for gaseous combustion are given, then the flamelet equations are derived. A brief description of counter-flow diffusion flames along with the governing equations and the numerical methods in solving the equations will be outlined next. In the results section, the temperature structure in mixture fraction as predicted by various mechanisms will be presented. Effects of strain and partial premixing on the temperature structure will also be discussed. The structure of flames obtained with various mechanisms is compared with that of the GRI-Mech 3.0 for different strain rates and different partial premixing. Finally, Major species and minor species structures are presented and discussed and will be followed by the conclusions.

1.2 Mathematical and Numerical Formulation

A continuous reacting flow system is described by the conservation equations of mass, momentum, energy and the species transport equations along with the boundary conditions, initial conditions, and the constitutive relations. In the following sections, the general three-dimensional equations for the gaseous combustion system are first presented along with the models for chemical processes and molecular transport, after that the flamelet equations and the equations for counterflow (opposed diffusion) flame, which represents the flamelet equations in physical space will be presented. A mapping will then be defined to transform the physical space counterflow flame solutions to mixture fraction space flamelet solutions.

1.2.1 Equations for Gaseous Combustion

The conservation of mass law applied to a fluid passing through an infinitesimal, fixed control volume yields the following equation of continuity

$$\frac{\partial \rho}{\partial t} + \frac{\partial (\rho u_i)}{\partial x_i} = 0 \tag{1.1}$$

where ρ is the fluid density and u_i is the fluid velocity in *i*th direction.

The momentum balance applied to the same infinitesimal, fixed control volume vields in the *i*th direction,

$$\frac{\partial(\rho u_i)}{\partial t} + \frac{\partial(\rho u_i u_j)}{\partial x_i} = \frac{\partial\sigma_{ij}}{\partial x_i} + \rho f_i \tag{1.2}$$

where $f_i = g_i$ is the gravitational body force per unit mass applied on the fluid element and σ_{ij} is the stress tensor. The total stress tensor σ_{ij} represents the surface forces per unit volume on the fluid element.

For a Newtonian fluid, the stress tensor (σ_{ij}) will be given, in tensorial notation, by:

$$\sigma_{ij} = -p\delta_{ij} + \mu \left(\frac{\partial u_i}{\partial x_j} + \frac{\partial u_j}{\partial x_i} \right) - \frac{2}{3} \mu \frac{\partial u_k}{\partial x_k} \delta_{ij}$$
(1.3)

where μ is the coefficient of viscosity, p is the pressure and δ_{ij} is the Kronecker delta function. In Eq. (1.3) the bulk viscosity is assumed to be negligible.

The application of energy conservation law to the control volume yields the total energy equation,

$$\frac{\partial E_t}{\partial t} + \frac{\partial (E_t u_i)}{\partial x_i} = \frac{\partial Q}{\partial t} - \frac{\partial q_i}{\partial x_i} + \rho \sum_k Y_k f_{k,i}(u_i + V_{k,i}) + \frac{\partial (\sigma_{ij} u_j)}{\partial x_i}$$
(1.4)

where E_t is the total energy per unit volume given by

$$E_t = \rho \left(e + \frac{u_i u_i}{2} + \text{potential energy} + \dots \right)$$

and e is the internal energy per unit mass, Y_k is species k mass fraction, $f_{k,i}$ is the body force in ith direction of species k, and $V_{k,i}$ is the diffusion velocity of species k in ith direction. Q is the heat produced per unit volume by the external sources and can be assumed to be zero and the first term gives the rate of heat produced per unit volume, second term gives the rate of heat flux exchanged and third and fourth term are respectively the work done per unit volume by body forces and surface forces. q_i of the second term is the heat flux in ith direction and it is given by

$$q_i = -k\frac{\partial T}{\partial x_i} + \sum_k \rho V_{k,i} Y_k h_k + q_{R,i} + \dots$$
 (1.5)

where k is the coefficient of thermal conductivity and T is the temperature. The first term in Eq. (1.5) is the heat transfer by heat conduction, the second term is heat flux due to mass diffusion and the third term represents the heat flux due to

radiation. Dufour effect is neglected.

The species mass fractions in a reacting mixture are determined by the species continuity equations which are given by

$$\frac{\partial \rho_k}{\partial t} + \frac{\partial \left[\rho_k(u_j + V_{k,j})\right]}{\partial x_j} = \dot{\omega}_k \qquad k = 1, 2, ..., K$$
(1.6)

where ρ_k (= ρY_k) is the partial density of species k, $\dot{\omega}_k$ is the production rate of species k due to chemical reactions and K is the total number of species. Y_k is the mass fraction of the species k. In the above equation (Eq. (1.6)), k does not obey the summation rule. This equation can also be written in terms of mass fractions as

$$\rho \left(\frac{\partial Y_k}{\partial t} + u_j \frac{\partial Y_k}{\partial x_j} \right) + \frac{\partial (\rho Y_k V_{k,j})}{\partial x_j} = \dot{\omega}_k \qquad k = 1, 2, ..., K$$
 (1.7)

where the mass flux of species k due to the diffusion can be approximated using the Fick's law:

$$V_{k,i} = -\frac{D_k}{Y_k} \frac{\partial Y_k}{\partial x_i}$$

 D_k being the diffusion coefficient of species k.

The rate of production of each species $\dot{\omega}_k$ is evaluated by an appropriate chemistry model. A chemistry model consisting N reactions and K reactant species can be symbolically represented as

$$\sum_{k=1}^{K} \nu'_{nk} A_k \rightleftharpoons \sum_{k=1}^{K} \nu''_{nk} A_k \qquad n = 1, 2, ..., N$$

where A_k is the chemical symbol of reactant species k and ν'_{nk} and ν''_{nk} are the stoichiometric coefficients of species k in reaction n. The chemical source term $\dot{\omega}_k$ is a consequence of the production and destruction of species k due to each of the

reaction step, i.e.

$$\dot{\omega}_k = \sum_{n=1}^N \dot{\omega}_{nk}$$

and $\dot{\omega}_{nk}$ is given by:

$$\dot{\omega}_{nk} = (\nu_{nk}'' - \nu_{nk}') \frac{W_k}{W_n} \left[k_{fn} \rho^{\mu'} \prod_{k=1}^K Y_k^{\nu'_{nk}} - k_{bn} \rho^{\mu''} \prod_{k=1}^K Y_k^{\nu''_{nk}} \right]$$
(1.8)

where $\mu' = \sum_{k=1}^K \nu'_{nk}$, $\mu'' = \sum_{k=1}^K \nu''_{nk}$ and k_{fn} and k_{bn} are respectively forward and backward reaction rates for reaction n. W_k is the molecular weight of species k and W_n is

$$W_n = \sum_{k=1}^K \nu'_{nk} W_k$$

The rate constants in Eq. (1.8) can be calculated by the following equations:

$$k_{fn} = A_n T^{\beta_n} \exp\left(\frac{-E_n}{\bar{R}T}\right)$$

$$\frac{k_{bn}}{k_{fn}} = K_n(T)$$
(1.9)

where A_n is the pre-exponential factor, β_n is the temperature exponent, \bar{R} is the universal gas constant, E_n is the activation energy characterizing the reaction n and K_n is the equilibrium constant for reaction n.

The final equation that closes the above described equations by relating the thermodynamic variables (p, ρ, T, e, h) is the state equation which is given for a perfect gas by:

$$p = \rho \frac{R}{\bar{W}} T \tag{1.10}$$

where \bar{W} is the mixture-averaged molar mass given by

$$\bar{W} = \left(\sum_{k=1}^{K} \frac{Y_k}{W_k}\right)^{-1}$$

1.2.2 Flamelet Formulation

When the chemistry is fast as compared to transport processes (convection and diffusion), combustion can be shown [35, 37] to occur in laminar like thin layers within the turbulent flow field. These thin layers are called 'flamelets' and the regime of turbulent combustion where such an assumption is valid is known as flamelet regime. There has been a great amount of study on this concept, and extensive literature is available since most of the practical applications fall in to this regime. For non-premixed flame, the one-dimensional 'flamelet equations' will be derived in this section from Eqs. (1.1)-(1.7) via a coordinate transformation.

In the non-premixed flamelet, all the scalars (temperature, concentration of species and density) are uniquely related to a single chemistry independent tracking scalar variable called "mixture fraction" (Z) as,

$$Y_k = Y_k(Z)$$
 $T = T(Z)$ $\rho = \rho(Z)$

The mixture fraction describes the level of mixedness of the fuel and oxidizer and can be interpreted (in a two-feed system) as the amount of mass originating from the fuel stream in the total mass at a particular location in space. It was first introduced by Burke and Schumann [12] for a one-step global chemical reaction

$$\nu_F F + \nu_O O \rightarrow \nu_p P$$

where F, O and P refer to fuel, oxidizer and product respectively. If \mathcal{L} be set to an

operator defined as

$$\mathcal{L} = \rho \frac{\partial}{\partial t} + \rho u_j \frac{\partial}{\partial x_j} - \frac{\partial}{\partial x_j} \Big(\rho D \frac{\partial}{\partial x_j} \Big),$$

where D is the diffusivity of fuel and oxidizer assumed to be equal. Then the transport equations for the species mass fractions becomes

$$\mathscr{L}(Y_F) = -\nu_F W_F \dot{\omega}'$$

$$\mathscr{L}(Y_O) = -\nu_O W_F \dot{\omega}'.$$

Manipulation of the above equations to eliminate (reaction rate) $\dot{\omega}'$ leads to

$$\mathcal{L}(\beta) \equiv \mathcal{L}\left(\frac{Y_F}{\nu_F W_F} - \frac{Y_O}{\nu_O W_O}\right) = 0$$

The above function β can be normalized to yield the definition of mixture fraction with a value of unity in fuel stream (feed 1) and a value of zero in the oxidizer stream (feed 2) as

$$Z = \frac{\beta - \beta_2}{\beta_1 - \beta_2} = \frac{\nu Y_F - Y_O + Y_{O,2}}{\nu Y_{F,1} + Y_{O,2}}$$

where ν is given by,

$$\nu = \frac{\nu_O W_O}{\nu_F W_F}$$

This definition of mixture fraction based on the fuel and oxidizer mass fractions is not valid for more general chemistry models. Since the intermediates are formed from the reactants over a broad region in space, it is possible that the mass fractions of fuel and oxidizer may be small in this region and therefore will have a constant value of mixture fraction according to the above definition. This situation can be remedied by using the definition given by Bilger [7] based on the element mass fractions

$$Z = \frac{\frac{2(Z_C - Z_{C,O})}{W_C} + \frac{0.5(Z_H - Z_{H,O})}{W_H} - \frac{(Z_O - Z_{O,O})}{W_O}}{\frac{2(Z_{C,F} - Z_{C,O})}{W_C} + \frac{0.5(Z_{H,F} - Z_{H,O})}{W_H} - \frac{(Z_{O,F} - Z_{O,O})}{W_O}}$$
(1.11)

where Z_i is the element mass fraction of element i and W_i is the atomic weight of the element i.

Mixture fraction transport is governed by the equation given by

$$\rho \frac{\partial Z}{\partial t} + \rho u_j \frac{\partial Z}{\partial x_j} = \frac{\partial}{\partial x_j} \left(\rho D_Z \frac{\partial Z}{\partial x_j} \right)$$
 (1.12)

where Z is the mixture fraction and D_Z is the diffusion coefficient of mixture fraction. This is exactly same equation as the species equation (Eq. (1.7)) with Fick's law for species diffusion and no chemical source/sink terms.

The balance equations for species and temperature can be written from Eq. (1.7) and Eq. (1.4) respectively. In Eq. (1.7), Fick's law is assumed to be valid for diffusion velocities. In Eq. (1.4), the heat production term by external forces is neglected. Viscous terms and pressure gradient terms are also neglected based on the low mach number approximations and q_i can be substituted by Eq. (1.5). Consequently, the species and energy equation reduces to, after some manipulations

$$\rho \left(\frac{\partial Y_k}{\partial t} + u_j \frac{\partial Y_k}{\partial x_j} \right) - \frac{\partial}{\partial x_j} \left(\rho D \frac{\partial Y_k}{\partial x_j} \right) = \dot{\omega}_k \qquad k = 1, 2, ..., K$$
 (1.13)

$$\rho \left(\frac{\partial T}{\partial t} + u_j \frac{\partial T}{\partial x_j} \right) - \frac{\partial}{\partial x_j} \left(\rho D \frac{\partial T}{\partial x_j} \right) = -\frac{1}{c_p} \sum_{k=1}^K h_k \dot{\omega}_k - \frac{1}{c_p} \frac{\partial q_{R,j}}{\partial x_j}$$
(1.14)

where D is assumed to be same for all the species and is equal to the thermal diffusivity of the mixture at that point (equal diffusivity assumption) implying a Lewis number of one (Le = 1) for all the species and $c_{p,k}$ is assumed constant and equal to c_p for all species.

In flamelet models, the above equations are written in a coordinate system that is attached to the surface of stoichiometric mixture fraction in which the x_1 coordinate is replaced by mixture fraction Z. With a Crocco-type transformation

Eqs. (1.13) and (1.14) are written as

$$\rho \frac{\partial Y_l}{\partial \tau} = \rho D \left(\frac{\partial Z}{\partial x_i} \right)^2 \frac{\partial^2 Y_l}{\partial Z^2} + \dot{\omega}_l \qquad l = 1, 2, ...K$$
 (1.15)

$$\rho \frac{\partial T}{\partial \tau} = \rho D \left(\frac{\partial Z}{\partial x_i} \right)^2 \frac{\partial^2 T}{\partial Z^2} - \sum_{l=1}^K \frac{h_l}{c_p} \dot{\omega_l} - \frac{1}{c_p} \frac{\partial q_{R_i}}{\partial x_i}$$
 (1.16)

where $\tau = t$ and $x_2 \& x_3$ are directions perpendicular to Z. All the higher order terms in the (thin) flamelet reaction zone have been neglected (see [35] for details). This formulation leads to a one-dimensional flame structure normal to the surface of stoichiometric mixture. The influence of the flow field in the flamelet equations, Eqs. (1.15) and (1.16), is introduced through the instantaneous scalar dissipation rate

$$\chi = 2D \Big(\frac{\partial Z}{\partial x_i}\Big)^2$$

An essential objective of the flamelet formulation is to decouple the chemical kinetics from the turbulence. One of the simple laminar flow configuration that can be representative for flamelets and may be used for building a flamelet library is the counter-flow flame. A flamelet library consists of the profiles of the temperature and mass fractions of the reactive species as a function of the mixture fraction $Z \& \chi$ and is used in turbulent flame calculations.

1.2.3 Counterflow Flames

In counterflow flames, a stagnation plane flame is established in the middle of the two opposing nozzles at a place, which is dependent on the momentum of two streams. One of the streams, which is called fuel stream, contains the partially premixed fuel and the other, called oxidizer stream, contains the air. The mass conservation equation for this counter-flow geometry is given by

$$\frac{\partial(\rho u)}{\partial x} + \frac{1}{r} \frac{\partial(\rho vr)}{\partial r} = 0$$

where u and v are the axial and radial velocity components and ρ is the mass density. With a karman similarity transform, the dependent variables depends only on the axial coordinates. Assuming velocity is a function of r only, the above equation can be transformed to

$$G(x) = \frac{dF(x)}{dx} \tag{1.17}$$

where

$$G(x) = -\frac{\rho v}{r}$$
 and $F(x) = \frac{\rho u}{2}$

The radial pressure gradient is constant,

$$\frac{1}{r}\frac{\partial p}{\partial r} = H = \text{constant},\tag{1.18}$$

and the radial momentum equation is governed by

$$H - 2\frac{d}{dx}\left(\frac{FG}{\rho}\right) + \frac{3G^2}{\rho} + \frac{d}{dx}\left[\mu\frac{d}{dx}\left(\frac{G}{\rho}\right)\right] = 0 \tag{1.19}$$

The transport equations for energy and species are

$$\rho u \frac{dT}{dx} - \frac{1}{c_p} \frac{d}{dx} \left(\lambda \frac{dT}{dx} \right) + \frac{\rho}{c_p} \sum_k c_{pk} Y_k V_k \frac{dT}{dx} + \frac{1}{c_p} \sum_k h_k \dot{\omega}_k = 0$$
 (1.20)

$$\rho u \frac{dY_k}{dx} + \frac{d}{dx} \left(\rho Y_k V_k \right) - \dot{\omega}_k W_k = 0 \qquad k = 1, K$$
 (1.21)

where the diffusion velocity is either given by the multi-component formulation

$$V_{k} = \frac{1}{X_{k}\bar{W}} \sum_{j=1}^{K} W_{j} D_{kj} \frac{dX_{j}}{dx} - \frac{D_{k}^{T}}{\rho Y_{k}} \frac{1}{T} \frac{dT}{dx}$$
(1.22)

or the mixture-averaged formulation

$$V_{k} = -\frac{1}{X_{k}} D_{km} \frac{dX_{k}}{dx} - \frac{D_{k}^{T}}{\rho Y_{k}} \frac{1}{T} \frac{dT}{dx}, \qquad D_{km} = \frac{1 - Y_{k}}{\sum_{j \neq k}^{K} X_{j} / \mathcal{D}_{jk}}$$
(1.23)

where D_{kj} , D_{km} , \mathcal{D}_{jk} and D_k^T are the multi-component, mixture averaged, binary, and thermal diffusion coefficients, respectively.

The boundary conditions for the fuel (subscript F) and oxidizer (subscript O) streams at the nozzles are

At
$$x = 0$$
: $F = \frac{\rho_F u_F}{2}$, $G = 0$, $T = T_F$, $\rho u Y_k + \rho Y_k V_k = (\rho u Y_k)_F$ (1.24)

$$At \ x = L: \qquad F = \frac{\rho_O u_O}{2}, G = 0, T = T_O, \qquad \rho u Y_k + \rho Y_k V_k = (\rho u Y_k)_O \qquad (1.25)$$

In this chapter, when diffusivities are equal, we use the mixture-averaged formula for diffusion velocity. Further, we assume that the thermal diffusion coefficient D_k^T is zero, and the mixture-averaged diffusion coefficient is replaced by thermal diffusivity $(\lambda/\rho c_{p,mix})$. In effect it will be reduced to the Fick's law with unit Lewis number. If Eq. (1.23) with the above mentioned modifications is used in Eq. (1.21), will give the flamelet equation in physical space. By using the definition given in Eq. (1.12) the mixture fraction can be calculated at each point in the physical space then the solution of Eq. (1.21) can be mapped to be the solution of the flamelet equation (Eq. (1.15)). Similarly the equation (1.20) can be transformed to the flamelet equation (1.16) and the strain rate, which is uniquely related to the scalar mixture fraction dissipation [35], can be approximately computed as [26, 49]

$$a_s = \frac{2|v_o|}{L} \left(1 + \frac{|v_f|\sqrt{\rho_f}}{|v_o|\sqrt{\rho_o}} \right) \tag{1.26}$$

Here, L is the distance between the two co-axial nozzles, v is the velocity and ρ is the density at the nozzle exit. Subscripts o and f denote the oxidizer and fuel.

1.2.4 Numerical Method

The above set of equations for counterflow flame Eqs. 1.17-1.25 will be solved to determine the temperature and species fields. Then each grid point in the physical space is mapped into a point in mixture fraction space using the Eq. (1.11).

The counter-flow diffusion and partial premixed flame is simulated using the Oppdif [30] application of Chemkin II [24]. The differential equations, Eqs. (1.17)–(1.23) along with the boundary conditions (Eqs. (1.24)–(1.25)) given above will form a two-point boundary value problem for the dependent variables (F, G, H, T, Y_k) . These equations are discretized with conventional finite differencing techniques for non-uniform mesh spacing. Diffusive terms use central differences, with truncation error that is second order in the mesh spacing. Convective terms use the upwind differencing, which uses the sign of the velocity to choose which direction the spatial difference will go. The truncation error of this approximation is first-order in the mesh spacing, leading to "artificial diffusion", which will avoid unwanted oscillations during the solution on the coarse mesh. Alternatively, the convective terms can be central differenced with second order accuracy in mesh spacing.

Oppdif, incorporates all the features described above and solves for the temperature, species mass fractions, axial and radial velocity components and radial pressure gradient. Chemical, thermodynamic and transport properties are evaluated in the model with the use of Chemkin and transport packages [23]. All the simulations conducted in this work uses mixture averaged transport properties.

Some selected test cases are run using the multi-component and mixture-averaged approximations for the transport properties. The difference in temperature predicted obtained by these two methods is insignificant.

The code is modified to include the equal diffusivity assumption in some of the simulations. This was achieved by setting the diffusion coefficient for all species equal to thermal diffusivity of the mixture at that location. Mixture fraction is calculated using the elements C, H and O and the formulation suggested by Bilger for the fuel containing C, H and O (see Eq. (1.11)). Since the governing equations given above does not contain the strain rate explicitly, the characteristic strain rate of the flow may be approximated by a formula based on the velocities and densities of the oxidizer and fuel streams and is given by Eq. (1.26). Velocities of both the fuel and the oxidizer jet streams are always taken to be equal and varied for different strain rates along with the distance between the nozzles. Initial temperature for the fuel and oxidizer stream is 300K in all simulations, unless stated otherwise.

1.3 Results and Discussion

All the mechanisms considered for this study, along with the number of species, reaction steps, and the corresponding reference are tabulated in Table 1.1. Results obtained by simulating the laminar counterflow flame for various cases are discussed in this section. The effects of strain and partial premixing are studied by analyzing the structure of temperature and species in physical and compositional (mixture fraction) space. The performance of reduced chemistry models are assessed by comparing the results generated with these mechanisms with those via GRI-Mech 3.0. The sensitivity of the ignition temperature to strain rate, premixing and chemistry model will also be discussed.

Table 1.1. Reaction Mechanisms Assessed.

Mechanism	Species	Reactions	Reference
4-step	8	4	Peters N. [38]
5-step	9	5	Hemanth P. Mallampalli et al [33]
6-step	10	6	WC. Chang and CY. Chen [14]
10-step	14	10	WC. Chang and CY. Chen [14]
12-step	16	12	C. J. Sung et al [53]
Skeletal	18	35	M. D. Smooke and V. Giovangigli [51]
Gri-Mech 1.2	32	177	M. Frenklach et al [19]
Gri-Mech 2.11	49	279	C. T. Bowman et al [11]
Gri-Mech 3.0	53	325	Gregory P Smith et al [50]

When the diffusivities of all the species in the system are taken to be equal and the Lewis number is taken to be unity, the structure produced by counterflow diffusion/partially-premixed flame is dependent only on mixture fraction and the stoichiometric scalar dissipation rate [6, 35, 37]. However, the results could be dependent on the computational domain size (the distance between the two stream nozzles) when the domain size is not sufficiently large. In this case, a zero gradient inlet conditions are not guaranteed and there will be a heat loss from the reaction zone to the

nozzle due to conduction [60]. This may cause a decrease in predicted peak temperature. To ensure the accuracy of results, various testings were performed. For example, in Figure 1.1(a), 1.1(b) and 1.1(c) show the flame (temperature structure) for three different domain sizes, 0.4, 1 and 2 centimeters respectively, a strain rate of 100(1/s), and 75% partial premixing of the fuel. For the cases with 1 and 2 cm domain size (cases b and c) the flame is sufficiently far from both the fuel and oxidizer nozzles, and for the case with 0.4 centimeters domain size the flame hits the nozzles creating a nonzero temperature gradient at the boundary, which causes the heat to flow out of the domain [60]. Figure 1.1(d) compares the temperature structure, produced for the three different cases discussed above, in mixture fraction space. Whereas in case (b) and (c) temperature profiles are almost identical with negligible difference [6], case (a) temperature profile is significantly different from the other two. In case (a) there is a heat loss to the nozzles due to non-zero gradients at the boundary. In this study care has been taken to contain the temperature profile in between the nozzles and cases such as (a) which display a disparity with others have been avoided.

1.3.1 Temperature Field

In this section the temperature structure is studied in both physical and compositional space as predicted by different reduced mechanisms. Figure 1.2 shows the typical effects of strain rate and partial premixing of the fuel on the temperature structure. Temperature is plotted in compositional space as predicted by GRI-Mech 2.11 mechanism for constant premixing and varying strain rates (Figure 1.2(a)), and constant strain rate and varying levels of partial premixing (Figure 1.2(b)).

Figure 1.2(a), which is plotted for constant fuel premixing of 75% and a strain that is varying from 10-400 (1/s), is in agreement with the earlier analytical, experimental, and numerical studies. The peak temperature is seen to be decreasing with increasing strain rate (or scalar dissipation rate, which is directly related to the strain rate). At the lowest strain rate of 10 1/s, a slight hump is seen on the

rich side of the flame, which is a precursor to the famous double flame structure. As the strain rate (or scalar dissipation rate) is increased, the premixed flame on the rich side will be pushed into the diffusion flame leading to a merged flame as noted by asymptotic analysis of Peters [36] and numerical studies of Tanoff and Smooke [54].

Figure 1.2(b) shows the temperature plot in mixture fraction space for a constant strain rate of 25 1/s and five different premixing levels of the fuel stream with air (%A =0, 25, 50, 75, 85). Premixing level has been given in terms of volume or mole percentage of air in the fuel stream. As the premixing level is increased from 0 (pure diffusion flame) to 85 percentage of air in fuel stream, the peak temperature shifts to the higher mixture fraction value (so does the stoichiometric mixture fraction value). The vertical lines in the plot show the stoichiometric mixture fraction values, from left to right, for each of the increased premixing level. A premixed flame is formed in the fuel stream as the premixing level is increased, which is due to the availability of enough oxidizer to the fuel in the fuel stream. A diffusion flame is formed from the products of premixed flame and oxidizer stream [10, 54]. The separation of the premixed flame and diffusion flame will lead to a double flame structure [28, 36, 47, 52, 62]. Plots similar to the above, with variable diffusivity effects included (not shown here) indicate trends similar to those of equal diffusivity case, even though there are some quantitative disagreements. Interestingly, the peak adiabatic flame temperature does not significantly change with partial premixing of the fuel with air, but it decreases slightly with strain rate as expected.

The temperature profiles in mixture fraction space as predicted by different mechanisms at various strain rates and various partial premixing levels are shown in Figures 1.3 and 1.4. Figure 1.3 shows the plots for strain rates of 10, 50, 150 and 300 1/s for a fuel stream premixed with 75% air. Here the 5-step and 6-step mechanisms over-predict the temperature in the fuel-rich region, but the 4-step one under-predicts the temperature in the same region. However, the difference in the temperatures predicted by various mechanisms is less for the lower strain rates (compare 1.3(a))

and 1.3(b)). However, for all the values of strain rates 5-step over-predicts the peak temperature whereas 4-step under-predicts it and the 10-step and 12-step mechanisms predictions are in good agreement with the GRI mechanisms. Even though the difference between the GRI-Mechanism and the reduced mechanisms decrease with the strain rate, 4-step, 5-step and 6-step mechanisms, which contains only the C_1 chain species, are not able to fully reproduce the results of GRI-mechanisms [60].

The temperature over-prediction of 5-step, 6-step mechanisms (as compared to GRI-Mechs and 10, 12 steps mechanisms) can be partially explained by considering the profiles of reactant production rates in mixture fraction space. Figure 1.5 shows the production rates of CH_4 , O_2 , and CO_2 species for 5-step and 10-step mechanisms. For 5-step mechanism the consumption of CH_4 and O_2 has one of the peaks in the fuel stream (near Z=1). The early peak in the fuel stream for consumption of CH_4 for 5-step maybe due to the representation of combustion in reactions. Oxidation of CH_4 involves O_2 and H_2O which are readily available in partially premixed fuel stream. In 10-step mechanism, radicals like H and CH_2O are involved in the oxidation of methane.

Figure 1.4 is plotted for various levels of partial premixing and at fixed strain rate of 25 1/s for different mechanisms. The temperature is over-predicted on the rich side at lower premixing levels for 4-step mechanism, but is under-predicted for higher partial premixing. And, for 5-step and 6-step mechanisms their prediction deteriorates as the level of premixing is increased from 0% air to 75% as the air available in the fuel stream is sufficient to cause the reactions to occur in the fuel stream. Again, the 10-step and 12-step mechanisms perform well and predict the temperature structure as the full mechanisms with high accuracy due to better representation of fuel consumption reactions by radicals near the diffusion flame zone.

To better quantify the differences in the predictions of temperature by different mechanisms, a parameter called mean relative percentage difference is defined

here, which represents the difference between GRI-Mech 3.0 (which is assumed to be the best mechanism tested here) and the mechanism in question. It is given as

$$\langle PD \rangle = \overline{\left[\frac{(T_{Ref} - T_{RM}) \times 100}{T_{Ref}} \right]}$$

where the T_{Ref} is the temperature obtained by the reference mechanism (here, GRI-Mech 3.0) and T_{RM} is the temperature obtained by the reduced mechanism. Averaging is performed over all the values in mixture fraction space on the rich side of stoichiometric value which is represented by the bar. This parameter has been plotted in Figure 1.6 for all of our simulations. Figure 1.6(a) shows the mean percentage difference versus strain rate for different reduced mechanisms for 75% premixing. This figure shows that the percent difference is reducing with strain rate for all the mechanisms. 4-step, 5-step, 5-step (Modified version), 6-step reduced reaction mechanisms perform badly for all cases and specially for low strains (refer to the explanation of Figure 1.3). 10-step, 12-step results lie within $\pm 2\%$ for all the strain rates. While the 4-step, 10-step and 12-step results show positive values indicating that the temperature predicted by these mechanisms are lesser than that of the reference mechanism GRI-Mech 3.0, 5-step, modified 5-step and 6-step values are all negative and thus over-predicting temperature on rich side. It can also be observed that $\langle PD \rangle$ is nearly constant for higher strain rates.

Figure 1.6(b) shows the variation of $\langle PD \rangle$ with respect to percentage of air in fuel stream for all the mechanisms. The relative mean difference for 4-step, 5-step and 6-step increases as the percentage of air in fuel stream is increased. 10-step and 12-step are predicting the temperature with good accuracy. One important point to be noted is that for 4-step mechanism the error seems to decrease first and then increase as more air is added to the fuel stream. However, the mean error plotted in this figure is absolute and since 4-step moves from over-predicting at lower premixing levels to under-predicting at higher premixing levels, it appears that the

error decreases first and then increases. It can also be seen that the mean difference decreases when percentage of air increases from 75% to 85%. The reasons for this behavior are explained below. Figure 1.7 show the maximum temperature difference between reduced and full (GRI-Mech 3.0) mechanisms in mixture fraction space versus the partial premixing. It can be seen that the maximum temperature increases with increasing premixing of fuel stream indicating that indeed the increasing levels of premixing worsens the temperature prediction for all the reduced mechanisms.

Figure 1.8(a) and Figure 1.8(b) shows the plot of temperature difference in mixture fraction space for 75% premixing and 85% premixing, respectively. It can be seen in Figure 1.8(a) that the width of region in mixture fraction space where there is significant temperature difference is much more than that for the 85% premixing even though the difference itself is small indicating that the premixed reaction zone is well separated from the diffusion flame in the 85% case. Since the prediction is bad in the premixed region than the non-premixed, and the average values are taken over the richer side of stoichiometric mixture fraction region, we see in Figure 1.6(b) that this average is lower for 85%.

1.3.2 Species Field

In addition to temperature, the other variables calculated and modeled in the flamelet methods include the species mass fractions, which are functions of mixture fraction alone under equal diffusivity and fast chemistry assumptions. So, it becomes important that the reduced reaction mechanisms should predict the species profiles accurately. The results for some important species are discussed in this section. First, the results for the major species CH_4 , O_2 and CO_2 will be considered, and comparison will be made between the structures of these species as obtained by different mechanisms in compositional space. Then the minor species such as H, H_2, CO and NO will be discussed. Similar to that of temperature analysis, a parameter will be defined for each species, which will represent the deviation of

predicted results via various mechanisms from GRI-Mech 3.0 results. The variation of this parameter with strain and partial premixing will be plotted.

The effect of partial premixing and strain rate on methane and oxygen are considered in figures 1.10 and 1.10, respectively. Figures 1.9(a) and 1.10(a) shows the mass fractions of CH_4 and O_2 in mixture fraction space as produced by different Each plot contains four subplots at different premixing levels (0, 25, 50, 75 percent) of fuel stream. Evidently, the compositional structure of both Y_{CH_4} and Y_{O_2} as computed by 4-step, 5-step and 6-step deviate more from the GRI-Mech 3.0 as the level of partial premixing is increased for a constant strain rate. 4-step over-predicts the mass fractions (or under-predicts the consumption) on the rich flame side, where as the 5-step and 6-step under-predicts the mass fractions. 10-step and 12-step follow closely the trends of full mechanisms. These trends are consistent with the trends in temperature structure (see figure 1.4). Higher temperatures are predicted at the regions where the consumption rates for reactants are predicted higher. A slight deviation is seen in the predictions of 4-step mechanism. At lower premixing levels even though the consumption rates of methane and oxygen for 4-step mechanism on the rich side of the flame are higher compared to other mechanisms, there is also a slightly higher prediction of temperature. This may be due to the fact that the 4-step mechanism does not involve a lot of other endothermic reactions as compared to the fuller mechanisms.

The effect of strain rate on Y_{CH_4} and Y_{O_2} for various mechanisms is shown in Figures 1.9(b) and 1.10(b). The four subplots in these figures are for different strain rates at a constant premixing of 75%. Again, similar to the temperature structure (see Figure 1.3), the reduced reaction model predict results closer to those of GRI-Mech 3.0 when the strain rate is increased. In both the fixed strain rate and fixed partial premixing plots, the profiles predicted by 4-step mechanism are piece-wise linear with a discontinuity in the gradient near the stoichiometric mixture fraction, where the reaction zone is located. This can be explained by the

non-existent of premixed flame zone in 4-step flames (double flame structure) for any of the cases considered (Figure 1.11). For the 5-step and 6-step mechanisms, at the lower strain rates and higher partial premixing levels one can find a pronounced double flame structure as the reaction mechanisms predict a longer separation in the diffusion and premixed reaction zones as shown in Figure 1.5 and Figure 1.11.

The compositional structures of CO_2 , H_2 and CO, as predicted by different mechanisms, and the effect of strain rate and partial premixing on them, are studied through figures 1.12, 1.13, and 1.14. Subplots (a) and (b) show the effects of varying partial premixing and strain rates, respectively. Interestingly in Figure 1.12(a) for CO_2 , unlike for the other species, it is seen that the disagreement is more pronounced in lower premixing levels than the higher premixing especially for 4-step and 6-step. This is explained in Figure 1.15, where the molar production rate of CO_2 along with its structure as predicted by 4-step and 5-step mechanisms are shown. The sharp peak in the mass fraction profile is not predicted very well by 4-step mechanism because of the sharp gradient in the production rate profile. In 4-step mechanism the only reaction that involves CO_2 is the reaction

$$CO + OH \rightleftharpoons CO_2 + H_2$$

whereas, in 5-Step mechanism it is combination of three reactions

$$3H_2 + O_2 + CO_2 = 3H_2O + CO$$

 $H_2 + CO_2 = H_2O + CO$

$$3H_2 + CO_2 + 2NO = 2H_2O + CO + N_2$$

where only the first two reactions are prominent in deciding the production of CO_2 . Prediction via 5-step at lower premixing levels compare well with GRI-Mechs, but it deviates at higher partial premixing levels, which is due to the incorrect representation of the premixed flame in fuel stream. The effect of strain rate in

Figure 1.12 (b), shows similar trends of betterment with increased strain rate.

Figures 1.13 and 1.14 show the structures of H_2 and CO respectively. to other species, the deviations between GRI-Mech 3.0 and other mechanisms increases as the strain rate is decreased, but the differences are much more pronounced for H_2 and CO than for the CO_2 and O_2 . An interesting observation is the similarities in the reduced reaction mechanisms behavior. For example, while 5-step and 6-step mechanisms have same behavior and predict higher mass fraction, 4-step predicts lower, and 10-step and 12-step predict much closer to the profile predicted by GRI-Mechs. This is due to the way these mechanisms are developed; 5-step and 6-step are derived from GRI-Mech 1.2, and contains only the C_1 species; 10-step and 12-step are also derived from GRI-Mech 1.2, but in addition to C_1 species they also incorporate the effects of C_2 species reactions. 4-step mechanism is derived from a skeletal reaction mechanism of 25 reactions and contain only C_1 species. As also observed earlier (Refer to [60]), mechanisms that took only C_1 reactions into consideration tend to be generally less accurately. The effect of partial premixing, on all the mechanisms, has been the reduction in peak mass fraction, and movement of the position of its occurrence towards higher mixture fraction values.

The results for H_2 and CO in Figures 1.13(b) and 1.14(b) indicates that the maximum mass fraction predicted by 4-step increases as the strain rate increases whereas, for the other mechanisms the opposite is true. This gives an erroneous view of the effect of strain on CO and H_2 structures if 4-step mechanism is used [15]. 10-step and 12-step compares well with the GRI-Mechs, especially the GRI-Mech 2.11, even though there are some deviations from GRI-Mech 3.0 at lower strain rates. In figure 1.14(a), it is shown that the peak of CO increases as the partial premixing is increased. This may seem surprising as we expect a reduction in CO emissions as more complete combustion occurs due to increased amount of oxidizer. The reason for this behavior is that in partially premixed flames, production of CO will start in fuel stream due to the oxidation of methane [10], which has to be transported to

the CO/H_2 oxidation diffusion flame. Therefore, the increase in CO production is due to increase in partial premixing and increase in the distance between methane oxidation zone and CO/H_2 oxidation zone.

Figures 1.16(a) and 1.16(b) shows the variation of mass fraction of H in mixture fraction space. The plots needed to be zoomed to show the details and consequently, the scales on individual plots are different. As the premixing is increased the H structure is broadened in mixture fraction space, a behavior that is different for different mechanisms. The peak mass fraction is decreasing for all the mechanisms with an increase in premixed air except for 4-step mechanism for which it remains nearly same. 5-step mechanism does not contain H, and the deviation from the full mechanisms for the 6-step mechanism is seen to increase initially then reduces. However, as the strain rate is increased the peak of H mass fraction structure is increased slowly for all the kinetic models except for the 4-step one. 4-step structure tends to deviate more from the full mechanisms as the strain rate is increased. Overall, predictions of H radical by 4-step is inaccurate for the cases (see Figure 1. of [8]).

Figures 1.17(a) and 1.17(b) show of structure of NO in compositional space for different partial premixing and different strain rates. There has been a great detailed study about the formation of NO_x in counterflow flames [10]. The mechanisms considered here that contain NO species are the 5-step, GRI-Mech 2.11 and GRI-Mech 3.0. The prediction by GRI-Mech 3.0 is very different from the other two as was noted earlier and 5-step prediction is close to GRI-Mech 2.11. Nevertheless, in all cases the peak production of NO occurs near the stoichiometric value of mixture except in the flame with 75% premixing and low strain. In this flame it seems to shift slightly to the right of the stoichiometric value. This is because of the production of NO by two different mechanisms - Finimore (Prompt) and thermal NO_x mechanisms [54]. Increasing premixing decreases the peak NO production as can be seen from Figure 1.17(a) [10, 54] and also increasing strain rates sees the

decrement in production of NO.

A parameter, similar to that which was defined for temperature will be defined below for species mass fractions to study the deviations of results obtained by various mechanisms from those of reference "full" mechanism. The reference mechanism is again taken to be GRI-Mech 3.0. Instead of relative mean difference, we define the mean difference (mean is represented by overbar or $\langle \rangle \rangle$, $\langle DF \rangle$, to be

$$\langle DF \rangle = \overline{(Y_{Ref} - Y_M)}$$

where Y denotes the mass fraction of species and the subscripts Ref and M stands for reference (which is GRI-Mech-3.0) and mechanism in question respectively.

Figures 1.18(a) and 1.18(b) show the temperature difference between GRI-Mech 3.0 and other mechanisms, averaged over the mixture fraction values greater than the stoichiometric value, with respect to the strain rate for CH_4 and CO, respectively. It can be observed in both the figures that as the strain is increased, $\langle DF \rangle$ decreases for almost all the mechanisms. The results for 4-step mechanism are somewhat different; for this mechanism first, $\langle DF \rangle$ decreases, passes through zero line, and then increases on other side (Values above 0 implies species mass fraction is under-predicted). There is a point in both figures for which the 4-step mechanism crosses the zero line which is where the 4-step values matches to that of GRI-Mech 3.0 in an average sense. But, it has to be noted that the value of the strain for different species is different, and thus one can not conclude that 4-step accurately predict all the variables (temperature and species mass fraction).

Figures 1.19(a) and 1.19(b) show the plot of $\langle DF \rangle$ versus percentage of air in fuel stream for CH_4 and CO. The trend for 5-step and 6-step mechanisms is similar to that observed for temperature; it first increases with increasing the premixing then drops at 85% premixing. 4-step mechanism shows relatively large deviations

as compared to other mechanisms for CH_4 . The drop in $\langle DF \rangle$ in Figure 1.19(b) when premixing air is increased from 75% to 85% can be attributed to lesser width of difference zone in mixture fraction domain. This is shown in Figure 1.20, where the maximum difference in Y_{CO} predictions by 5-step and 6-step mechanisms from those of GRI-Mech 3.0 increases with premixing.

4-step, 5-step and 6-step mechanisms, which contain only the C_1 species, does not perform satisfactorily for any of the strain rates and for different partial premixing though they predict within tolerance limits in some situations. 10-step and 12-step which contain both C_1 and C_2 species are able to reproduce the temperature structure within 2 percent difference from the reference GRI-Mech 3.0 for all the strain rates and premixing levels that are considered in this study. The temperature structure of 10 and 12 step mechanisms are more close to GRI-Mech 1.2 and 2.11 than GRI-Mech 3.0, which can be explained by the fact that they both are reduced from GRI-Mech 1.2. Considering that 10-step mechanism contains two species and two reactions steps less than that of 12-step mechanism, it can be said that it will be computationally less expensive to use 10-step mechanism.

1.3.3 Autoignition

In the past several decades the phenomena of flame extinction has been widely studied using analytical, experimental, and numerical approaches. Equally important ignition phenomena has also been the subject of extensive study in the recent years. Non-premixed mode of ignition takes place usually in diesel engines and supersonic combustors where the fuel is injected into heated air, which acts as a source of ignition. This type of ignition can be studied through the counterflow (opposed jet) flame model, where the cold fuel is ignited by an opposed hot air jet. Another flame ignition process which can be modeled by opposed jets is the flamelet ignition in turbulent jet flames. Ignition by this procedure has been studied extensively for methane/air mixtures of various dilutions with nitrogen [18]. The method that

was employed to determine the ignition temperature was to increase the oxidizer temperature incrementally until ignition occurs and a converged steady state solution is obtained.

An equally important situation that occurs in turbulent flames is the re-ignition of the strain extinguished flamelets, which can not be studied using cold fuel/hot air configuration. It is more likely, in these situations, that the fuel and air will both be at the same high temperature. For example quenched flamelet may contain both fuel and oxidizer at same temperature rather than the fuel being at 300K and oxidizer being at "ignition temperature" [18]. Ignition temperature obtained by this procedure may not be accurate for modeling the re-ignition of flamelets as they may over-predict the actual values.

In this work we determined the ignition temperature with the same fuel and oxidizer jet temperatures, and the initial temperature variation is taken to be a straight line in the domain. The magnitude of initial temperature is gradually increased in equal increments and a steady state solution is sought. If, a steady state solution is obtained at some temperature then the incremental step is halved and solution is sought in other direction (i.e., temperature is reduced with a halved step from the point where it was found to ignite). This procedure is repeated until the ignition temperature is determined with in a prescribed range. This whole procedure is automated and the ignition temperature can be determined with an accuracy of 10 degrees Kelvin within 10-15 iterations.

Figure 1.21 is plotted for the ignition temperature with respect to the strain rate for various partial premixing levels of fuel stream with air. It can be seen that the ignition temperature increases with strain rate for all premixing levels then it reaches a constant value for strain rate values higher than 300 1/s. The constant value it reaches at higher strain rate is dependent on the the level of premixing, and it decreases with increasing partial premixing. At strain rates below 100, the

added premixed oxidizer to fuel stream does not seem to have significant effect on the ignition temperature.

These results indicate that in a turbulent flow, where significant variations in strain rate and partial premixing of the fuel/oxidizer/products, the ignition, extinction and re-ignition of the flame is a very complex phenomena and may not be accurately modeled by simple laminar steady opposed jet data in the form of flamelet tables. The flamelet tables need to incorporate the level of partial premixing and mixture temperature as well as variable strain rate effects into account.

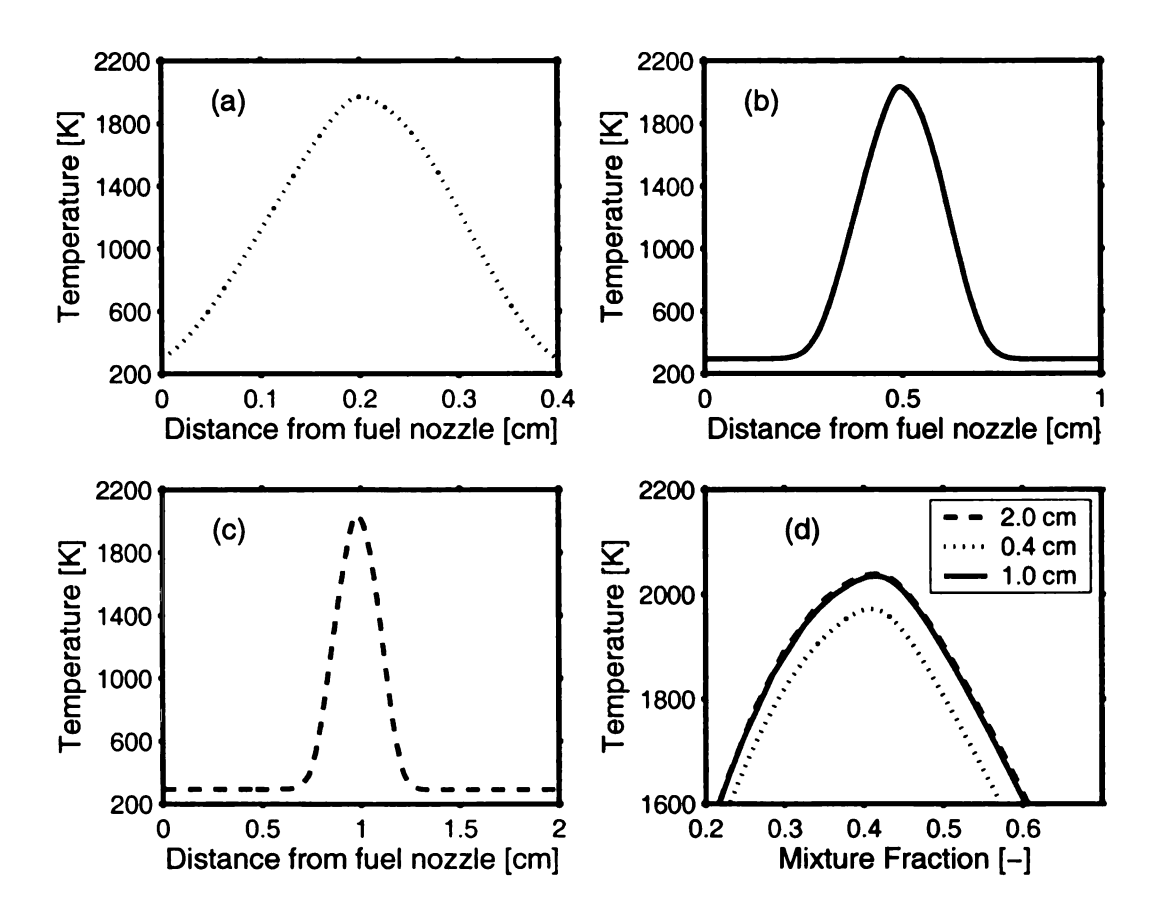


Figure 1.1. Temperature structures in physical and compositional space for various domain sizes, (a) 0.4 cm, (b) 1.0 cm, (c) 2.0 cm.

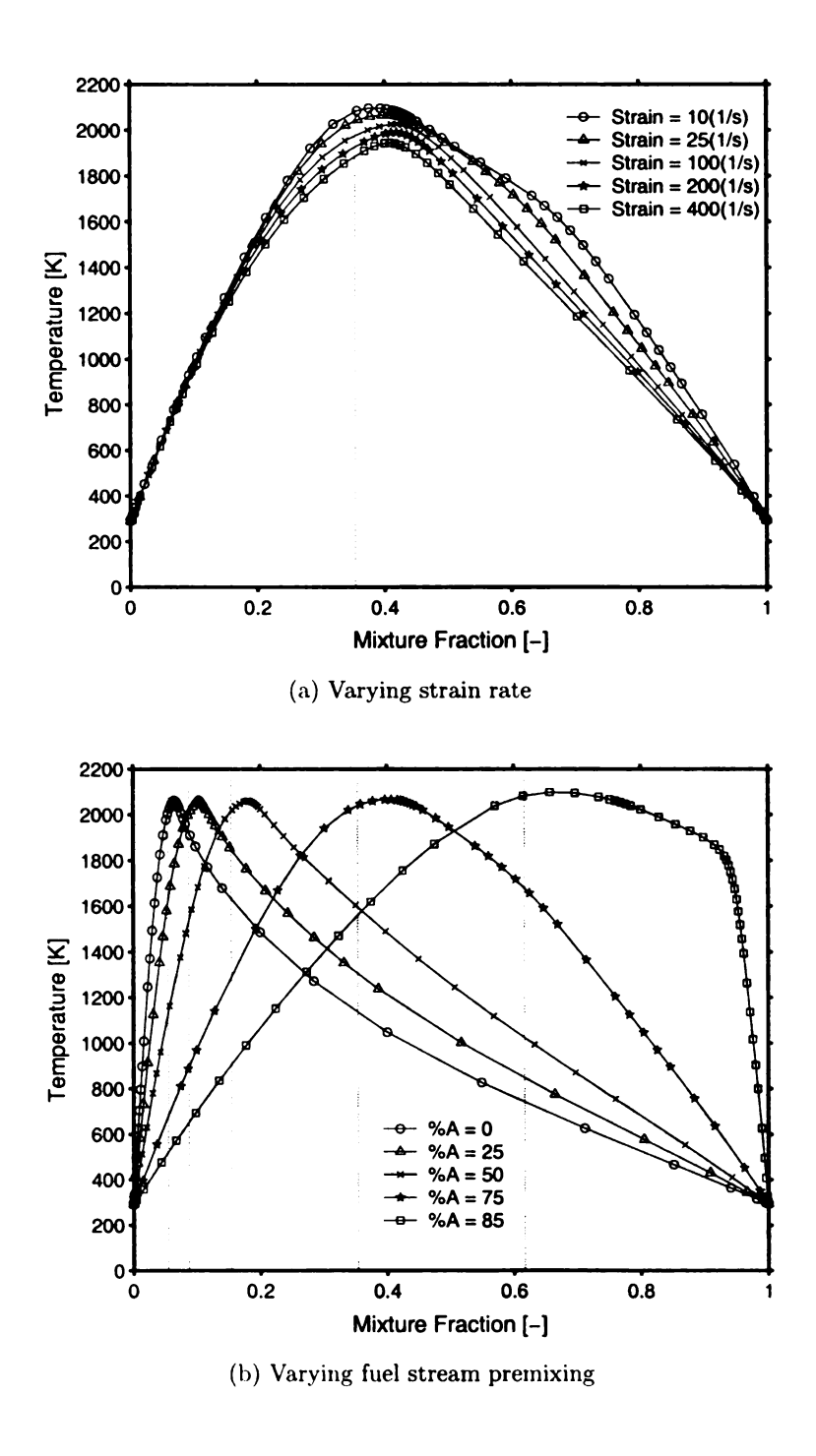


Figure 1.2. Temperature structure in mixture fraction space with GRI-Mech 2.11 (a) for different strain rates and premixing of 75% air in the fuel stream, (b) for different premixing levels of the fuel stream and strain of 25(1/s). Vertical lines indicate stoichiometric mixture fraction.

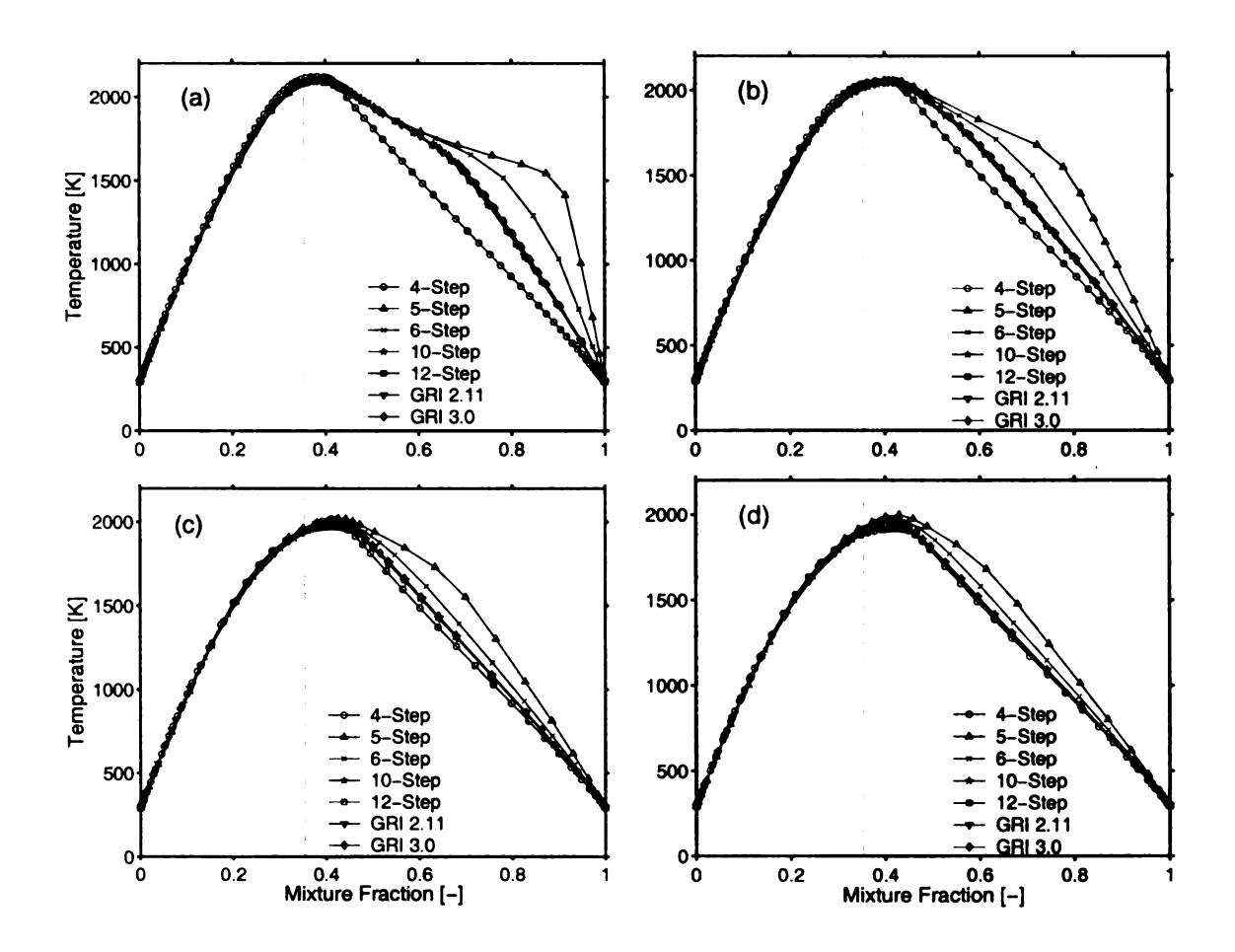


Figure 1.3. Compositional temperature structure obtained with various mechanisms for 75% premixing of fuel stream and different strain rates, (a) 10 (1/s) (b) 50 (1/s) (c) 150 (1/s) (d) 300 (1/s). Vertical lines indicate the stoichiometric mixture fraction.

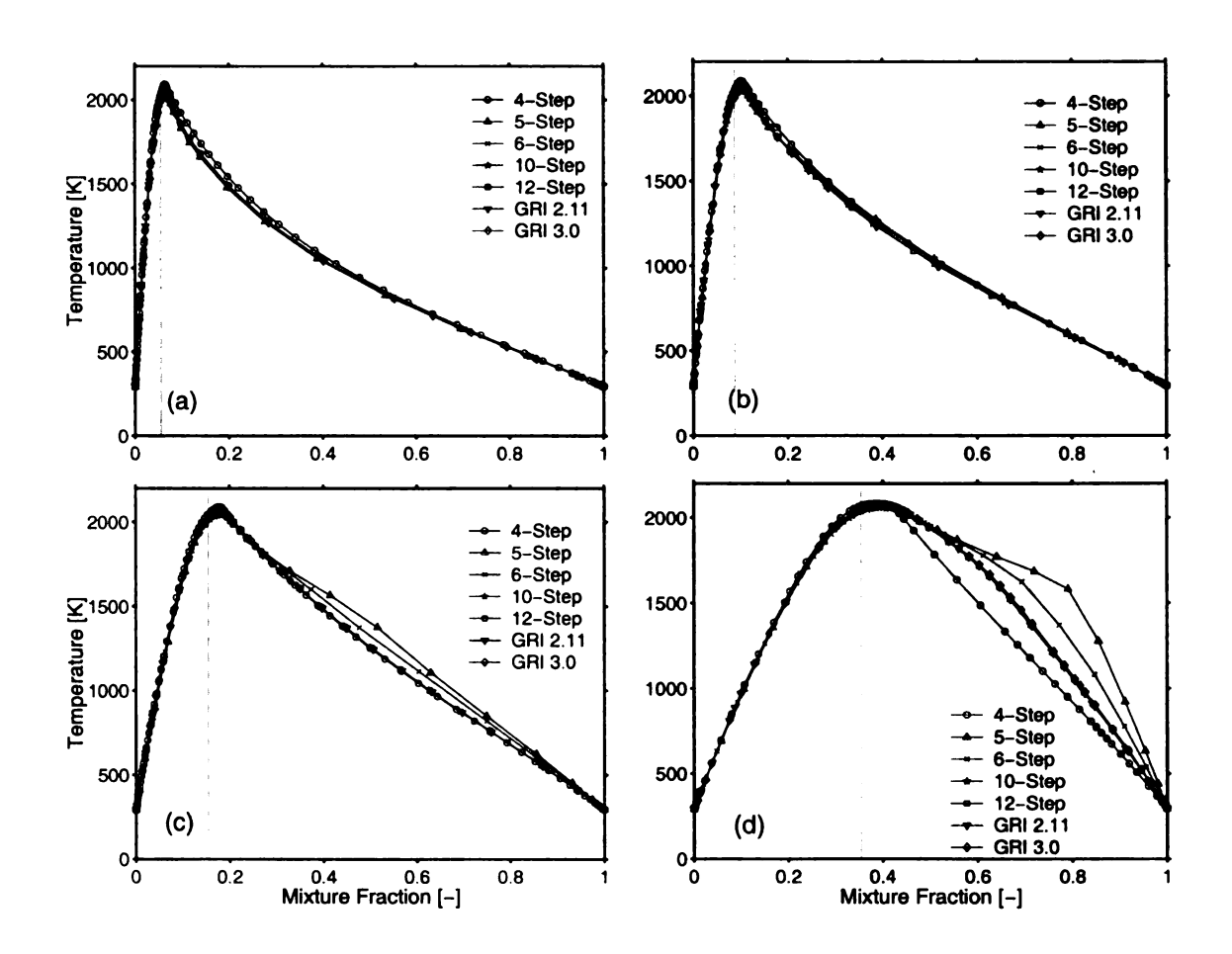


Figure 1.4. Compositional temperature structure obtained with different mechanisms for different premixing of fuel stream and a strain rate of 25 (1/s), (a) 0% (b) 25% (c) 50% (d) 75%. Vertical lines indicate the stoichiometric mixture fraction.

36

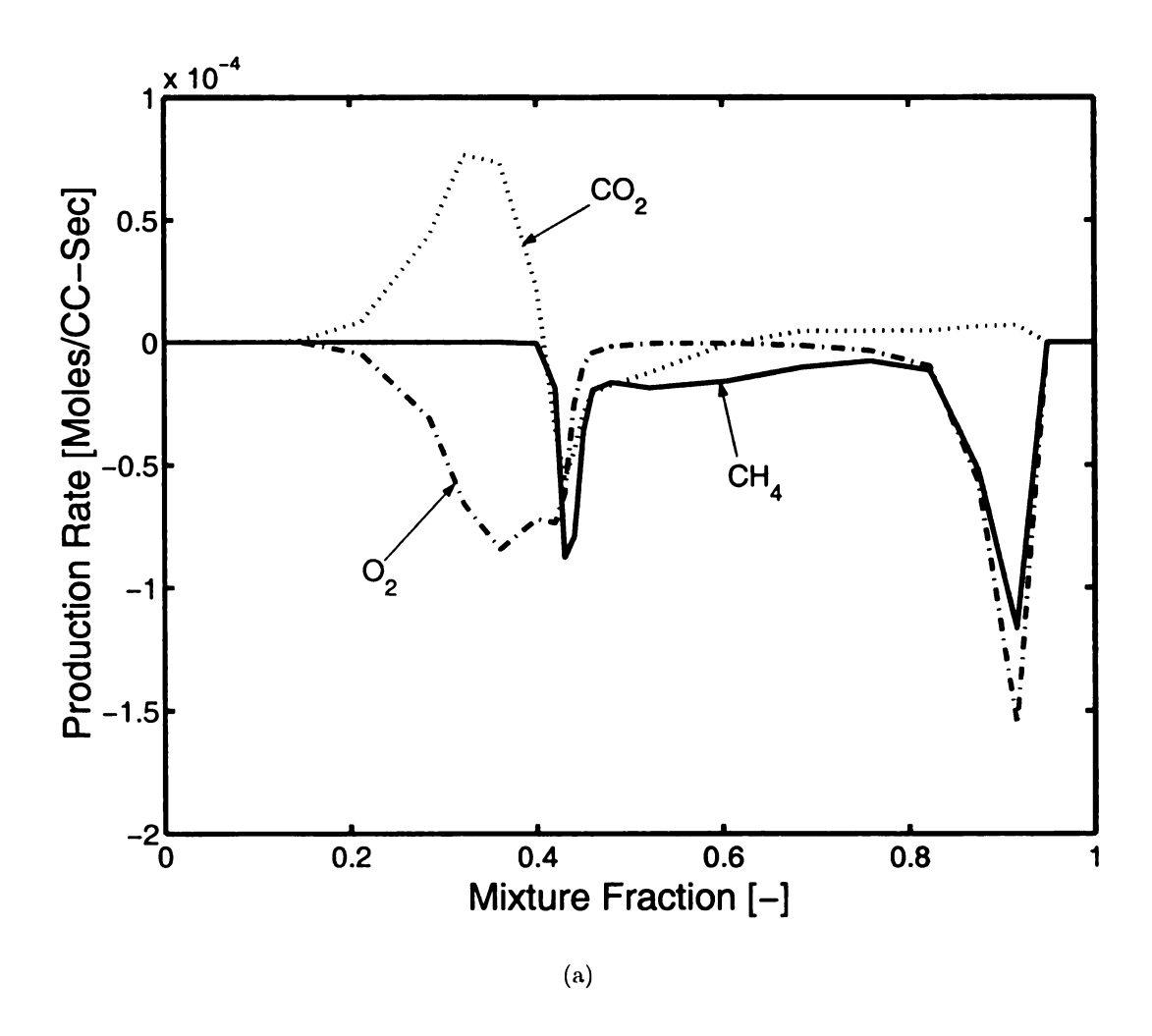


Figure 1.5. Production rates of CH_4, O_2 , and CO_2 . (a) 5-step mechanism

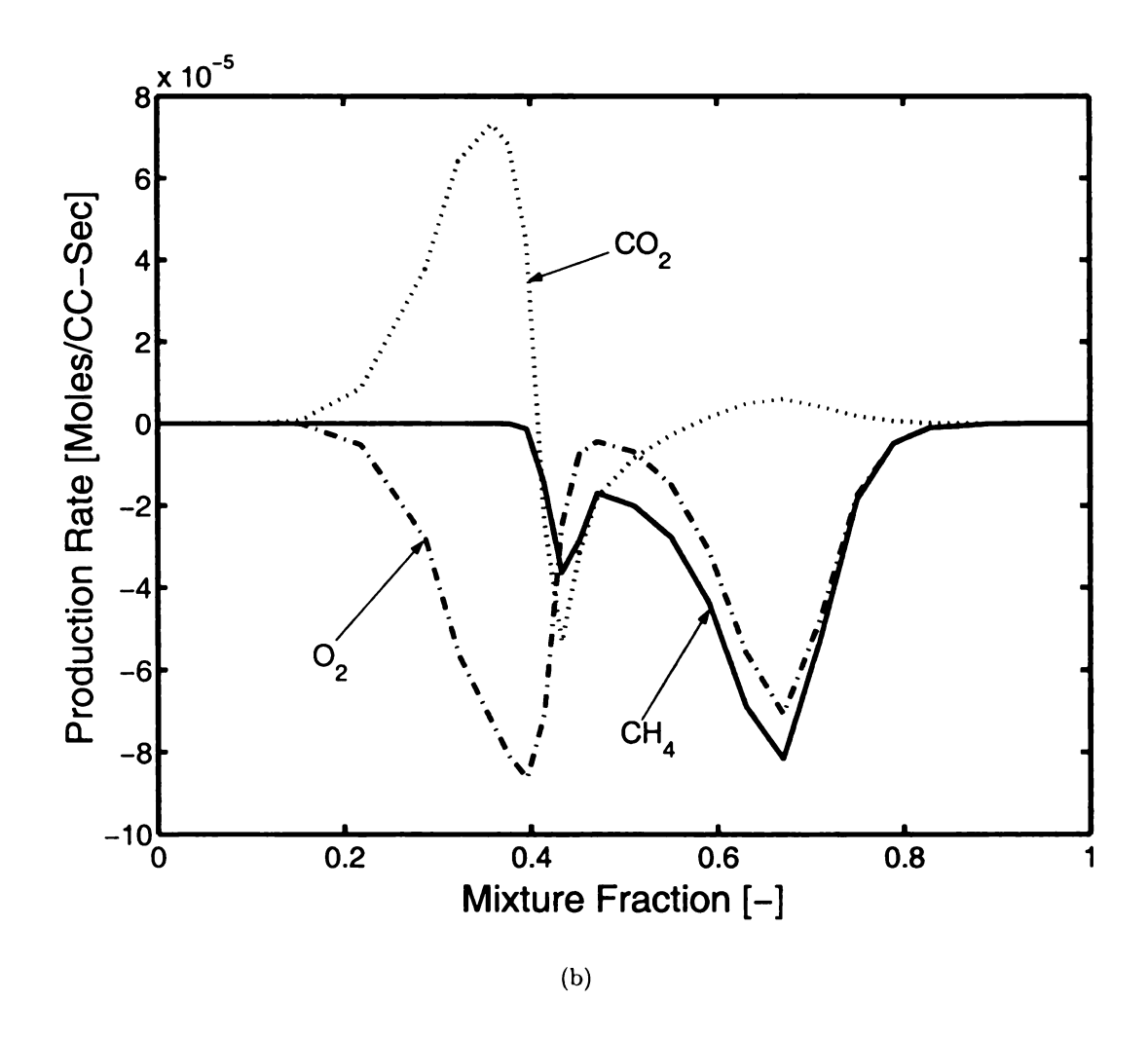
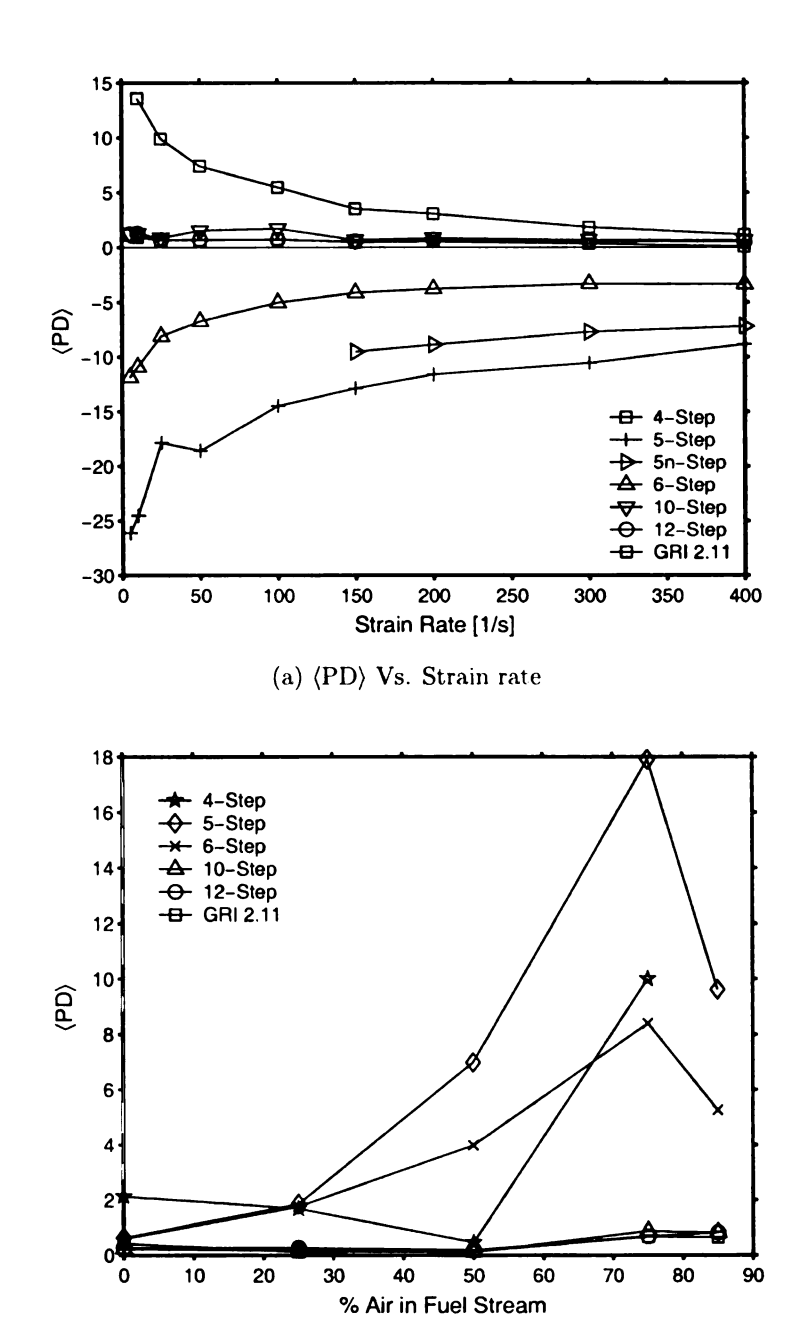


Figure 1.5. [contd...] Production rates of $CH_4, O_2,$ and CO_2 . (b) 10-step mechanism.



(b) $\langle PD \rangle$ Vs. Fuel stream premixing

Figure 1.6. Percentage mean of temperature difference from GRI 3.0 for different mechanisms vs. (a) strain rate for premixing of 75% air in fuel stream, (b) premixing level of fuel stream with air for strain rate of 25(1/s).

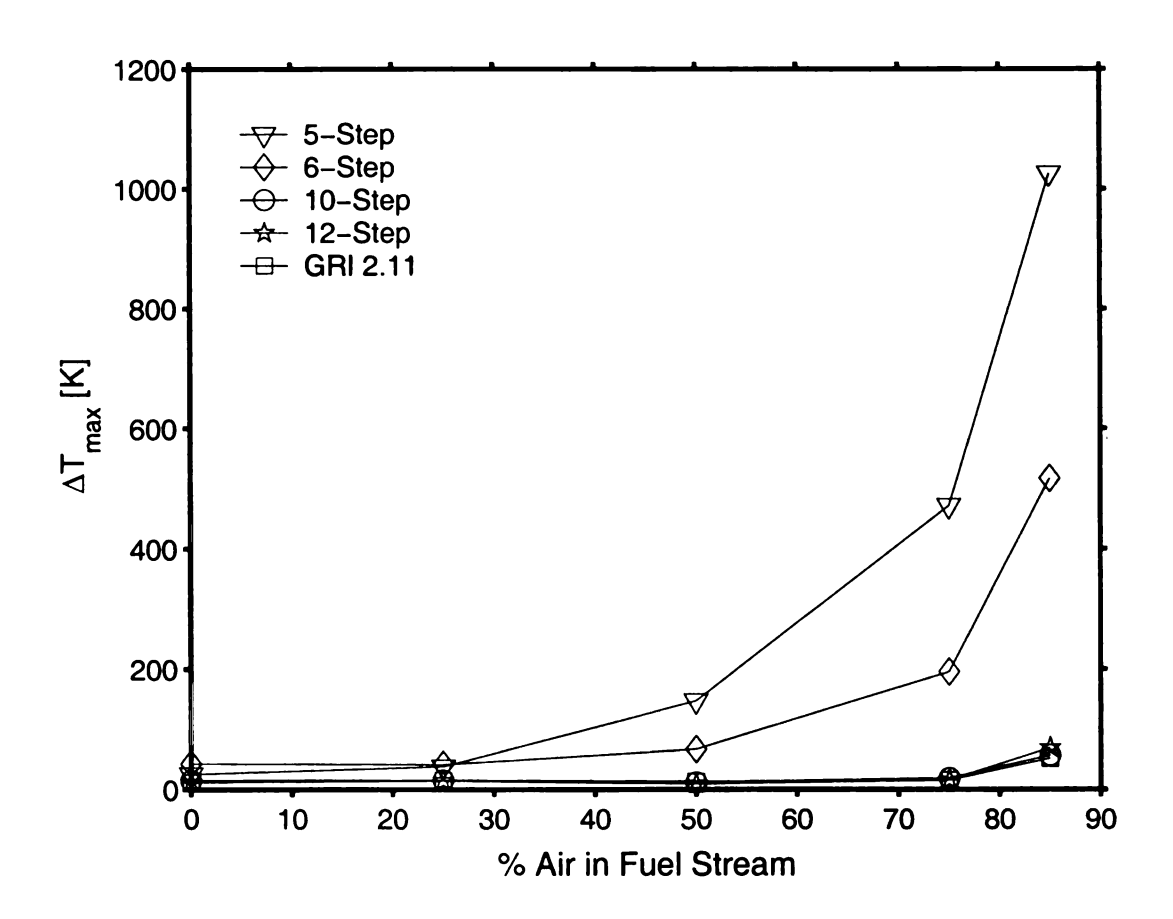


Figure 1.7. Maximum temperature deviation from GRI 3.0 predictions for different mechanisms and a strain of 25 (1/s).

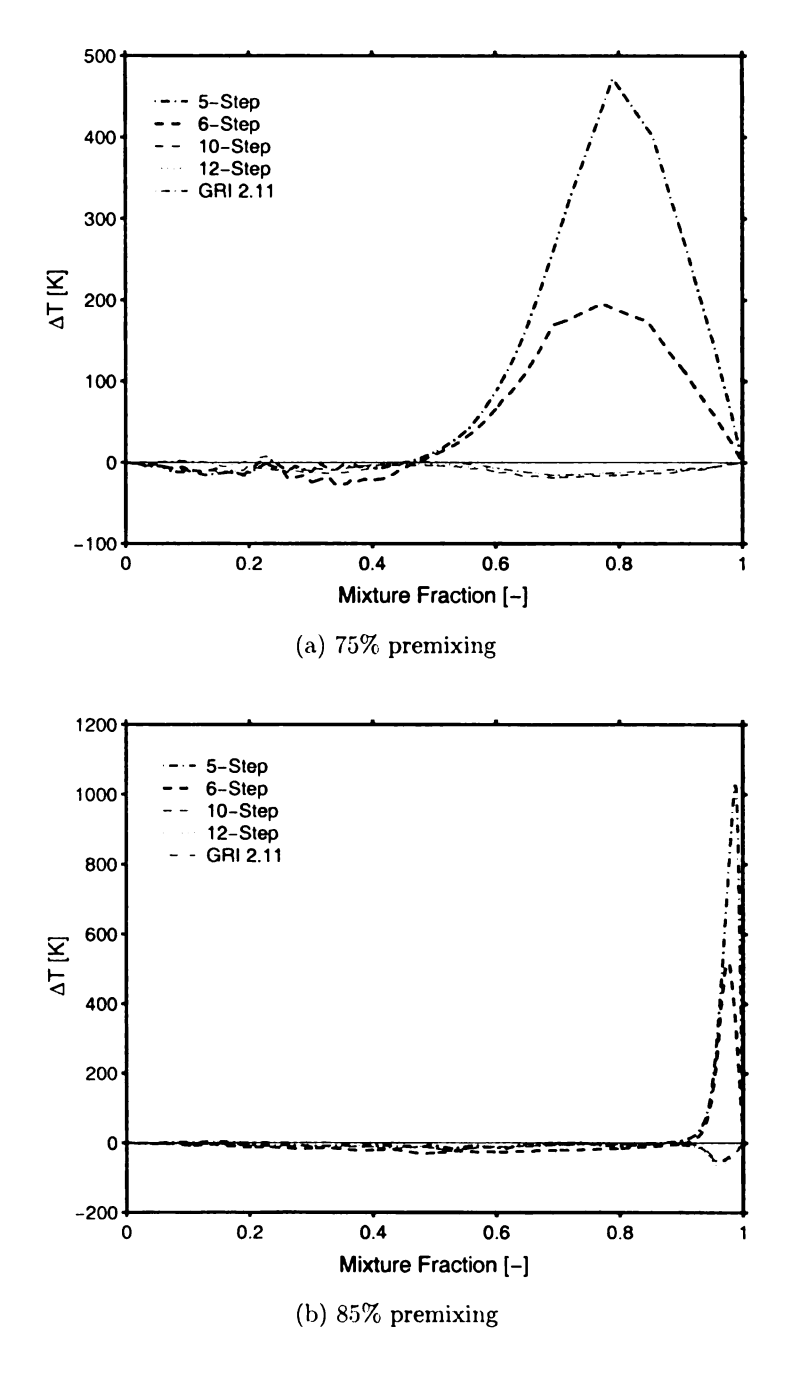


Figure 1.8. Temperature difference from GRI 3.0 for different mechanisms vs. mixture fraction for strain rate of 25(1/s) and (a) 75% air in the fuel stream, (b) 85% air in the fuel stream.

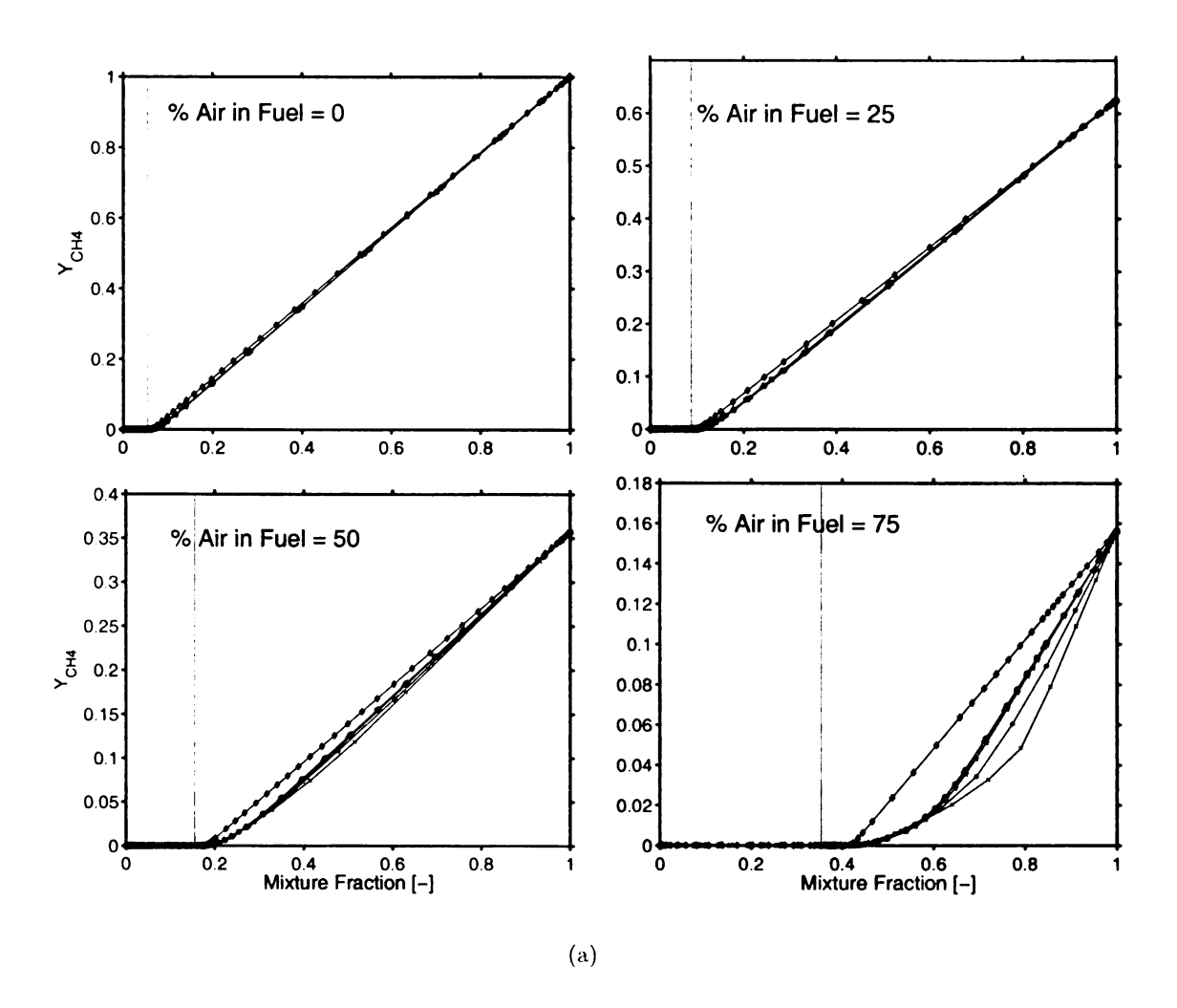


Figure 1.9. Effect of partial premixing on Y_{CH_4} structure. $-\diamondsuit-$, 4-Step; $-\times-$, 5-Step; -*-, 6-Step; $-\triangle-$, 10-Step; $-\Box-$, 12-Step; $-\bigcirc-$, GRI 2.11; $-\bigstar-$, GRI 3.0.

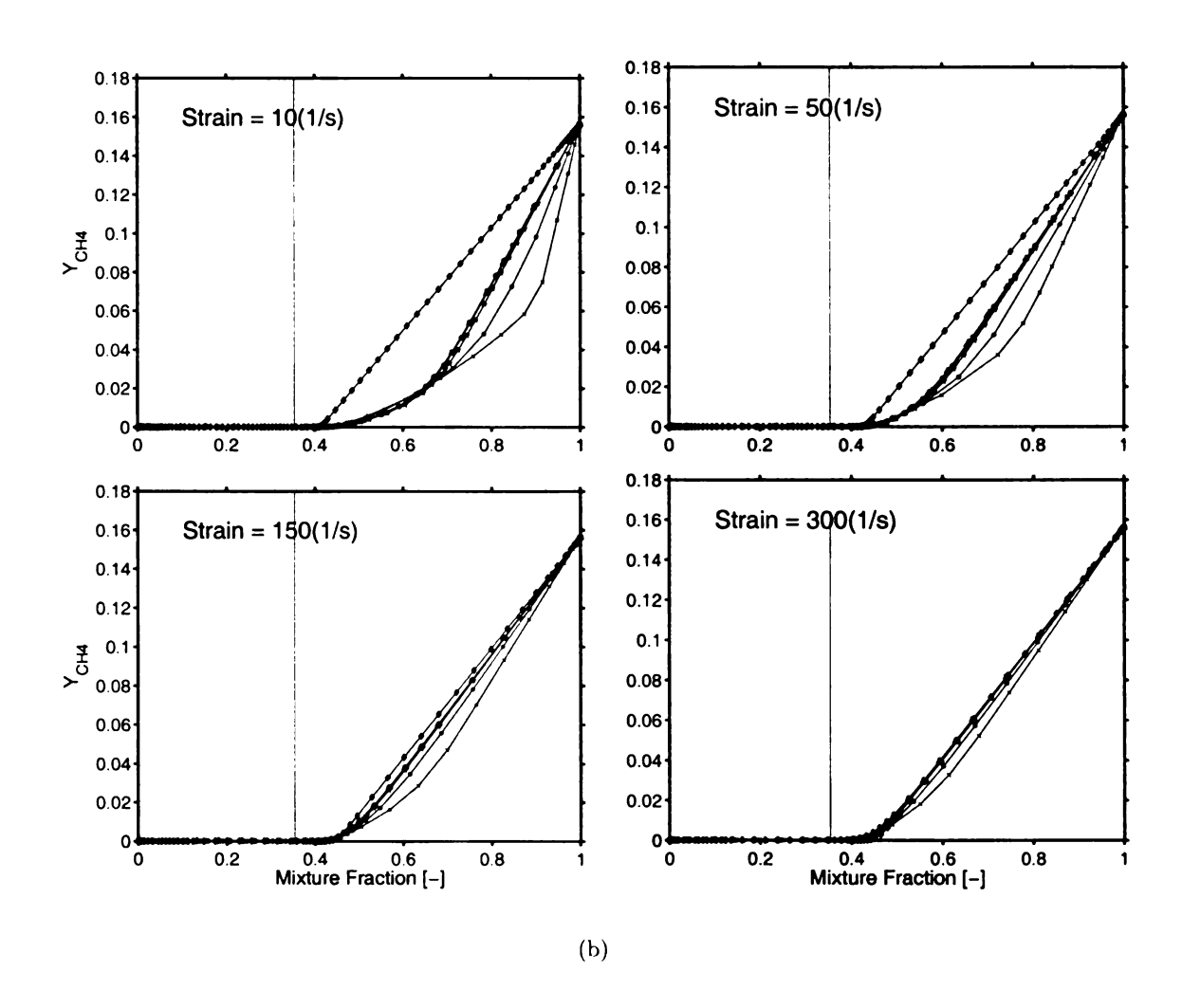


Figure 1.9. [contd...] Effect of strain rate on Y_{CH_4} structure. See Figure 1.9(a) for labeling

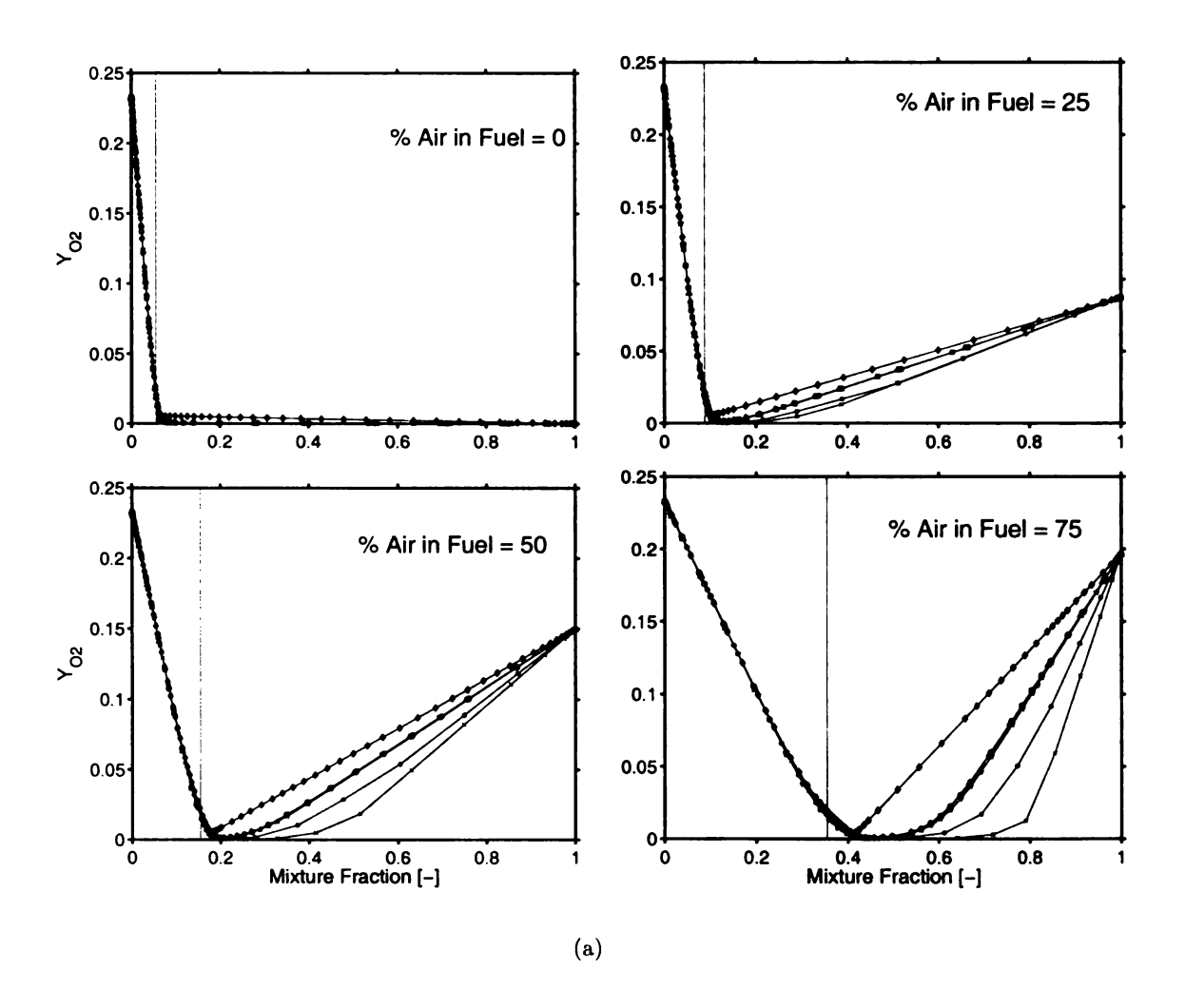


Figure 1.10. Effect of partial premixing on Y_{O_2} structure. See Figure 1.9(a) for labeling. Vertical lines indicate the stoichiometric mixture fraction.

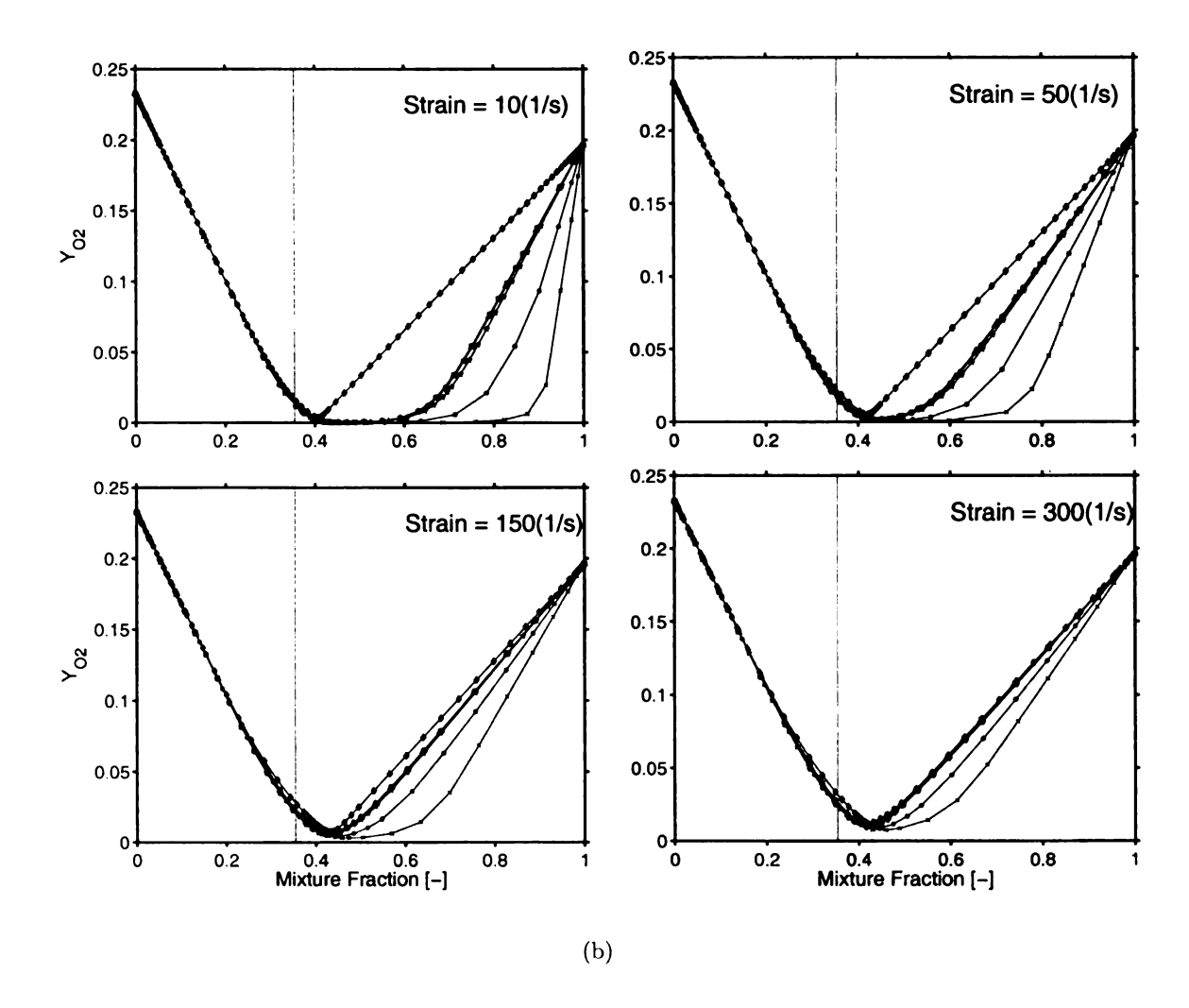


Figure 1.10. [contd...] Effect of strain rate on Y_{O_2} structure. See Figure 1.9(a) for labeling. Vertical lines indicate the stoichiometric mixture fraction.

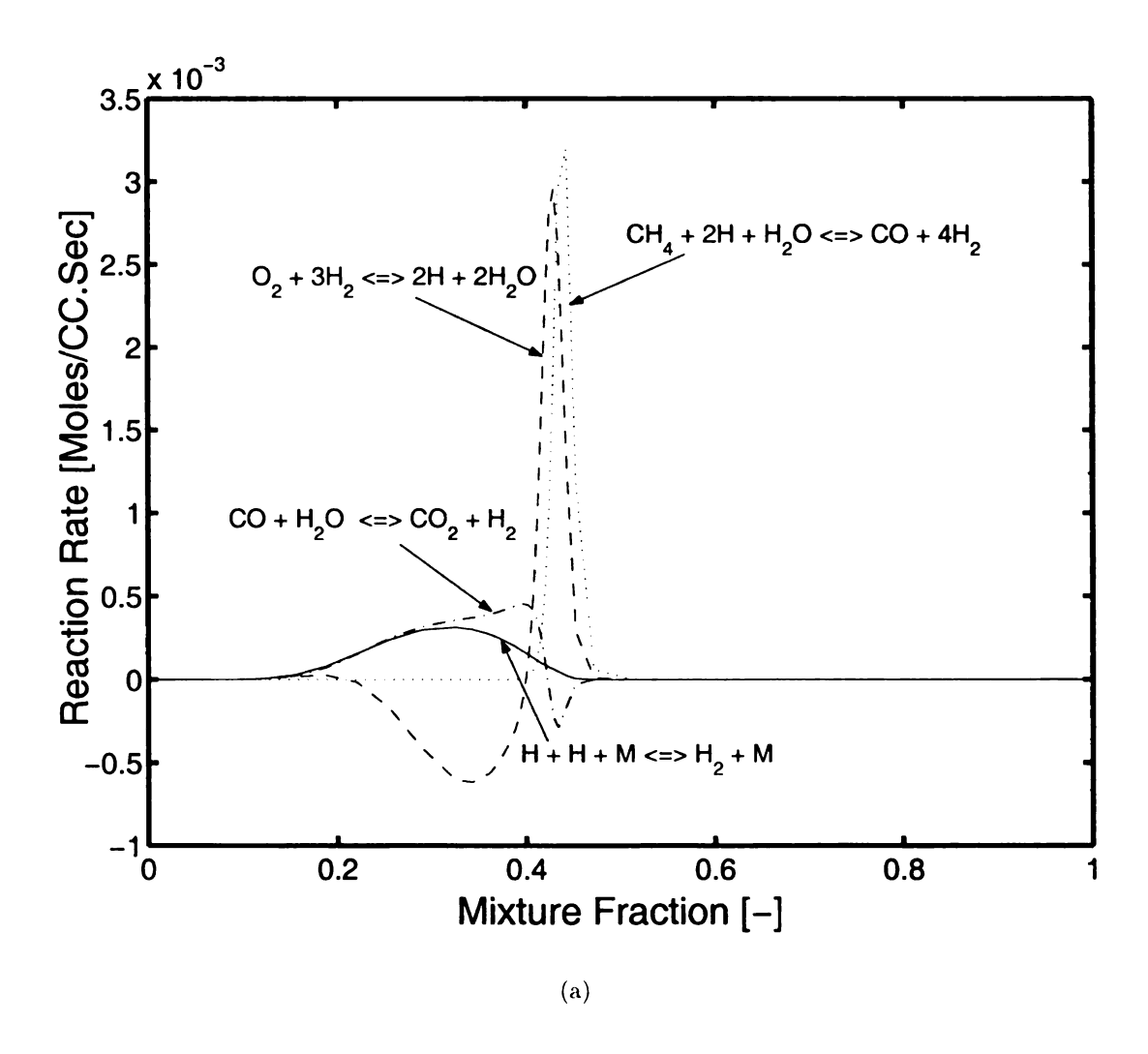


Figure 1.11. Reaction rate of the global reactions in (a) 4-step mechanism.

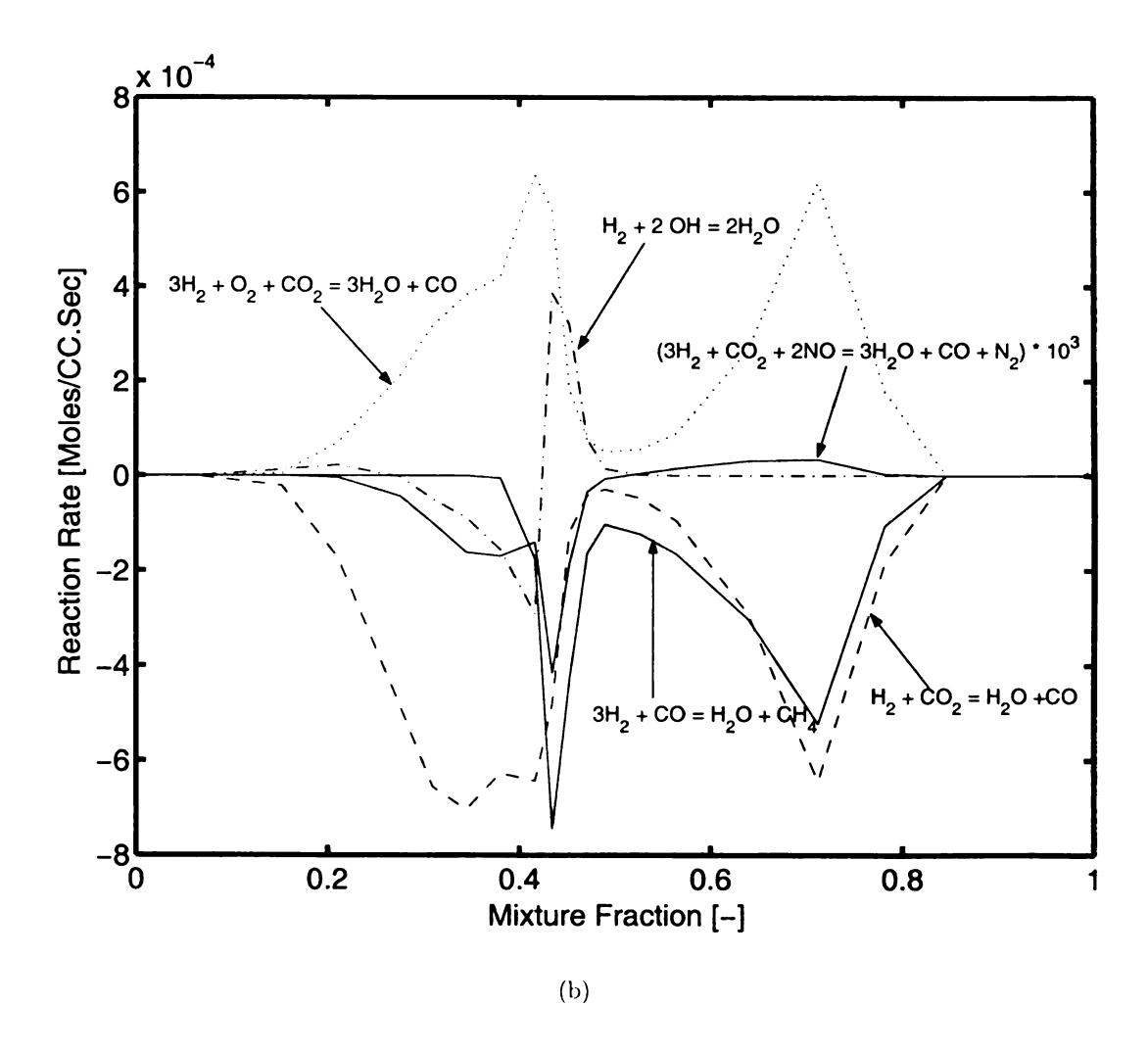


Figure 1.11. [contd...] Reaction rate of the global reactions in (b) 5-step mechanism.

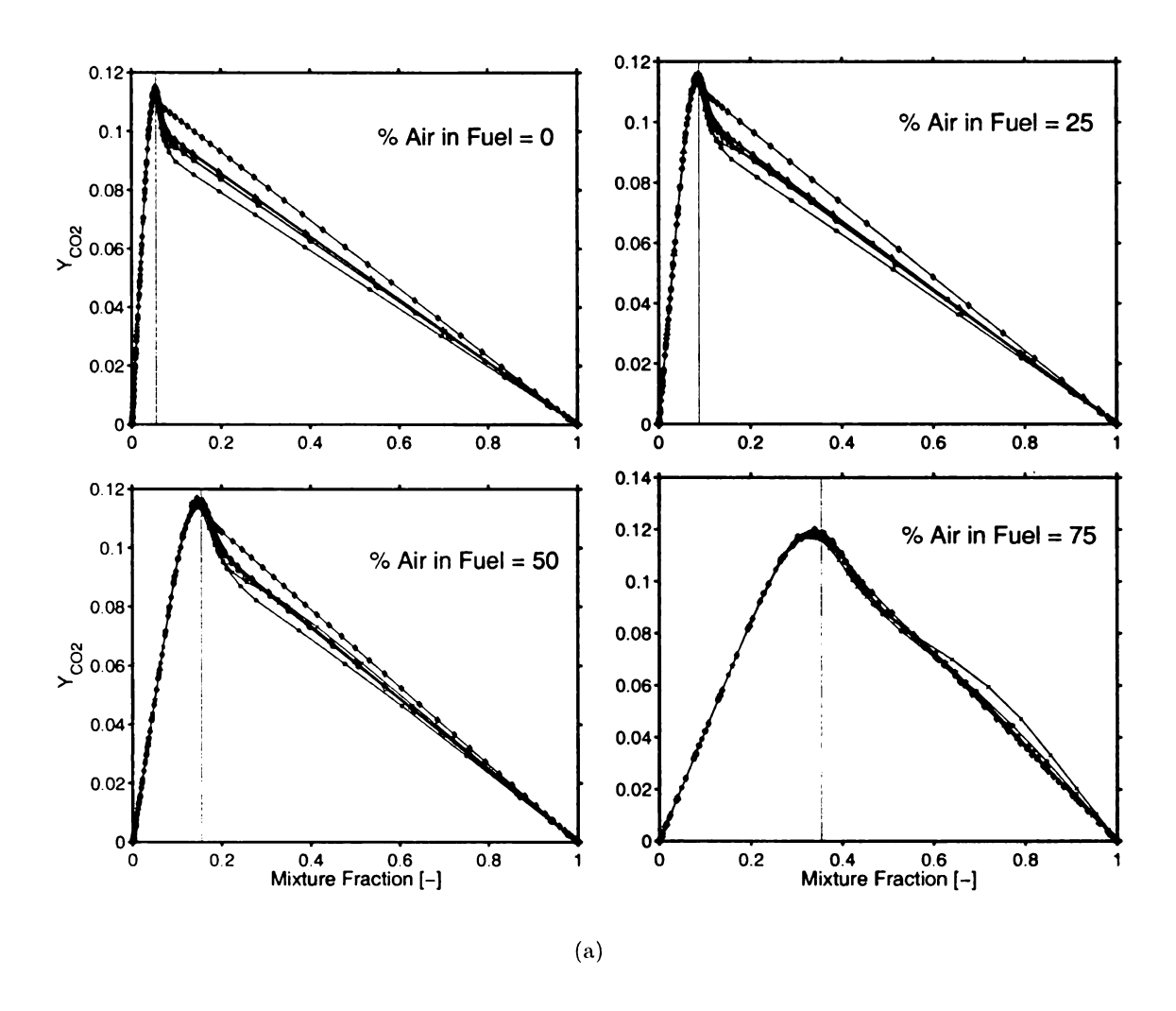


Figure 1.12. Effect of partial premixing on Y_{CO_2} structure. See Figure 1.9(a) for labeling. Vertical lines indicate the stoichiometric mixture fraction.

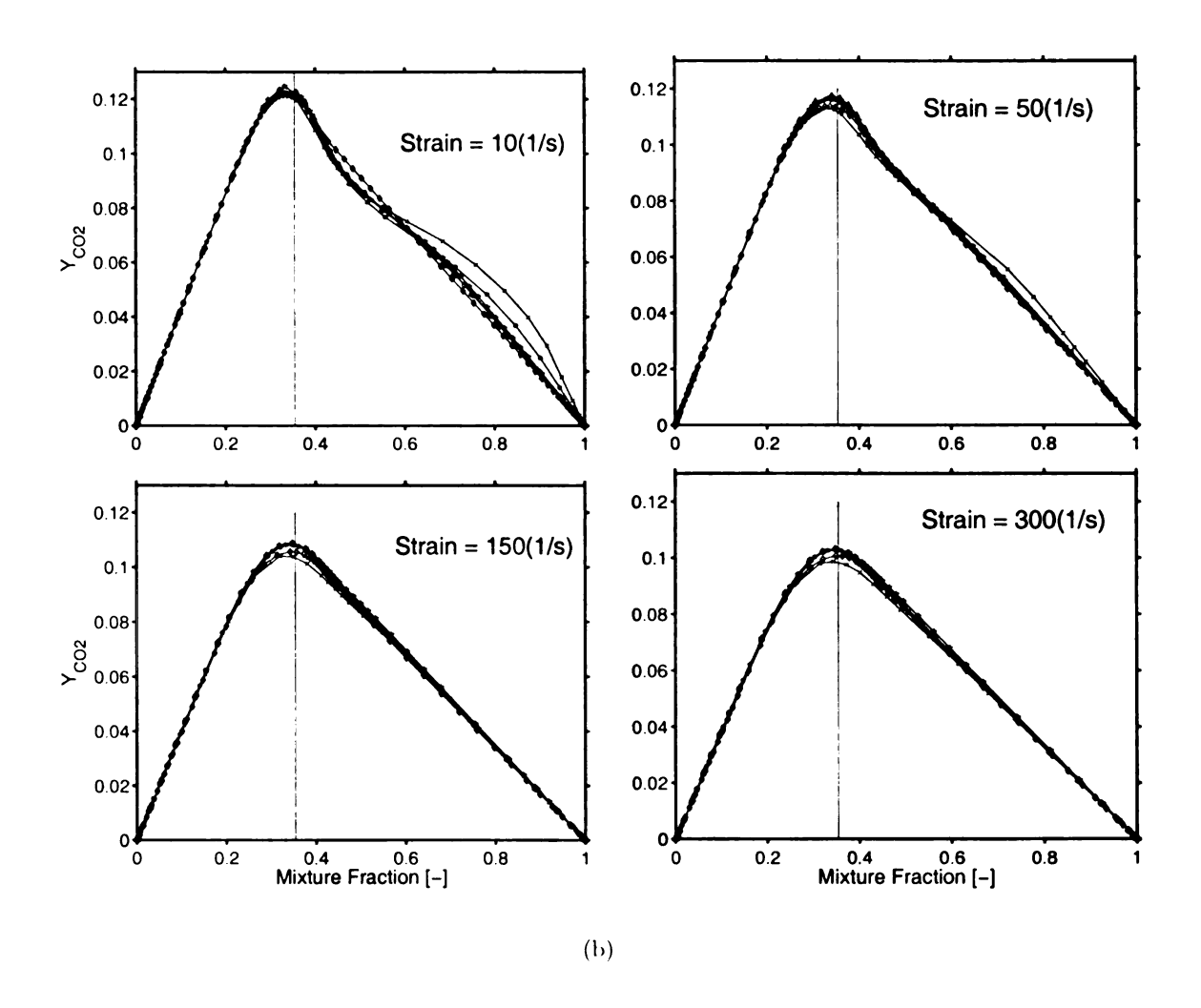


Figure 1.12. [contd...] Effect of strain rate on Y_{CO_2} structure. See Figure 1.9(a) for labeling. Vertical lines indicate the stoichiometric mixture fraction.

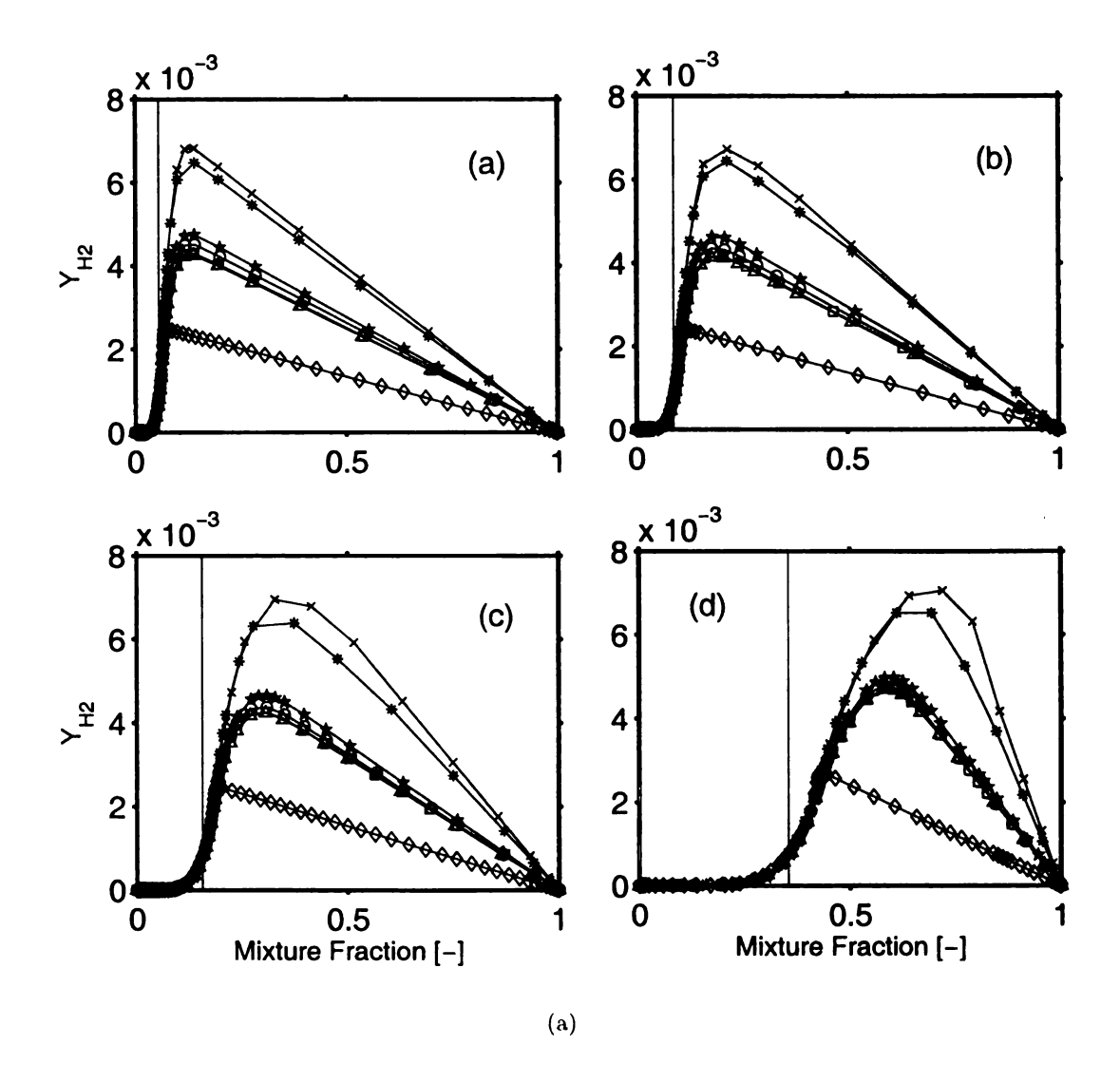


Figure 1.13. Effect of partial premixing on Y_{H_2} structure. (a) A% = 0, (b) A% = 25, (c) A% = 50, and (d) A% = 75. See Figure 1.9(a) for labeling. Vertical lines indicate the stoichiometric mixture fraction.

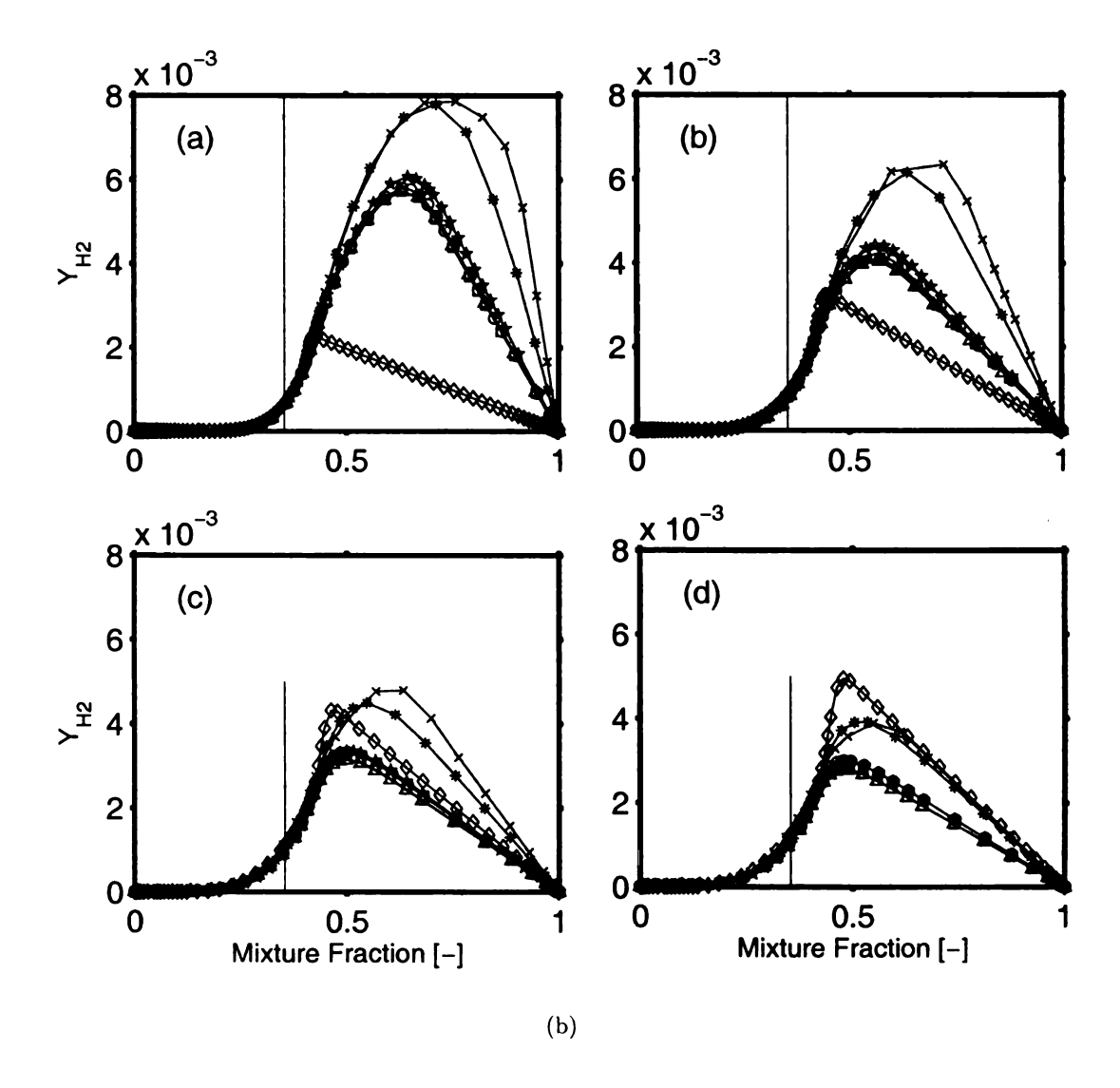


Figure 1.13. [contd...] Effect of strain rate on Y_{H_2} structure. (a) strain = 10 1/s, (b) strain = 50 1/s, (c) strain = 150 1/s, and (d) strain = 300 1/s. See Figure 1.9(a) for labeling. Vertical lines indicate the stoichiometric mixture fraction.

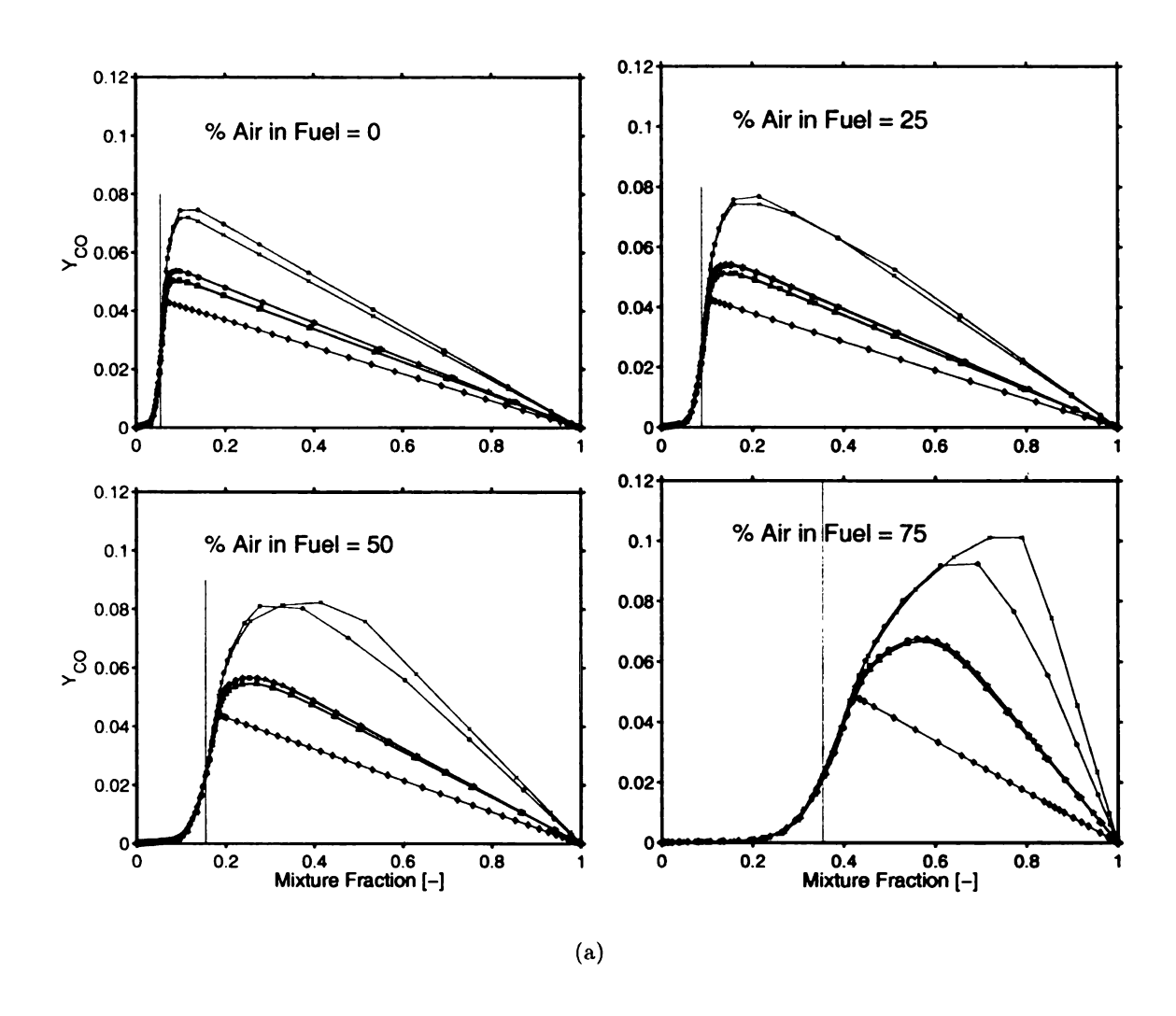


Figure 1.14. Effect of partial premixing on Y_{CO} structure. See Figure 1.9(a) for labeling. Vertical lines indicate the stoichiometric mixture fraction.

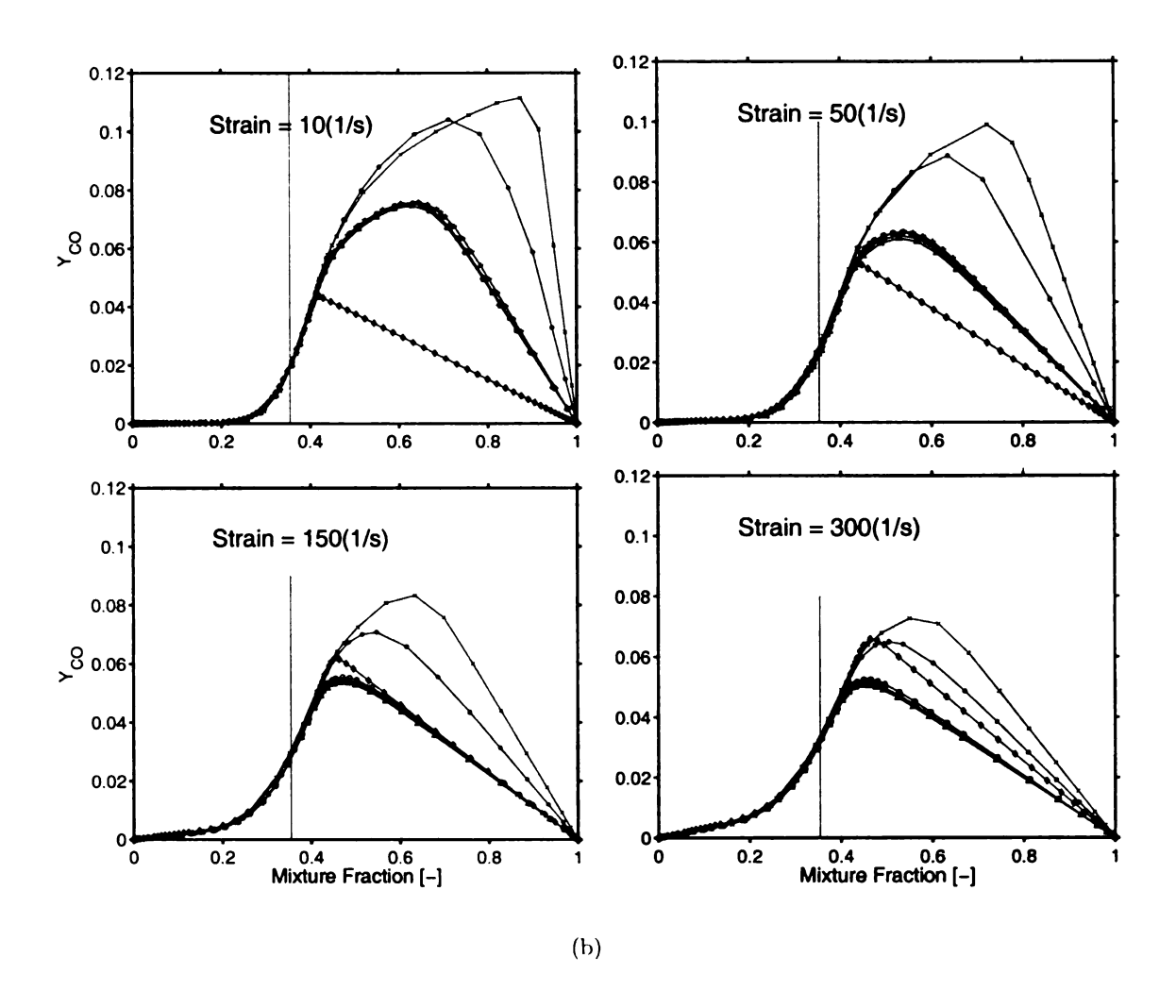


Figure 1.14. [contd...] Effect of strain rate on Y_{CO} structure. See Figure 1.9(a) for labeling. Vertical lines indicate the stoichiometric mixture fraction.

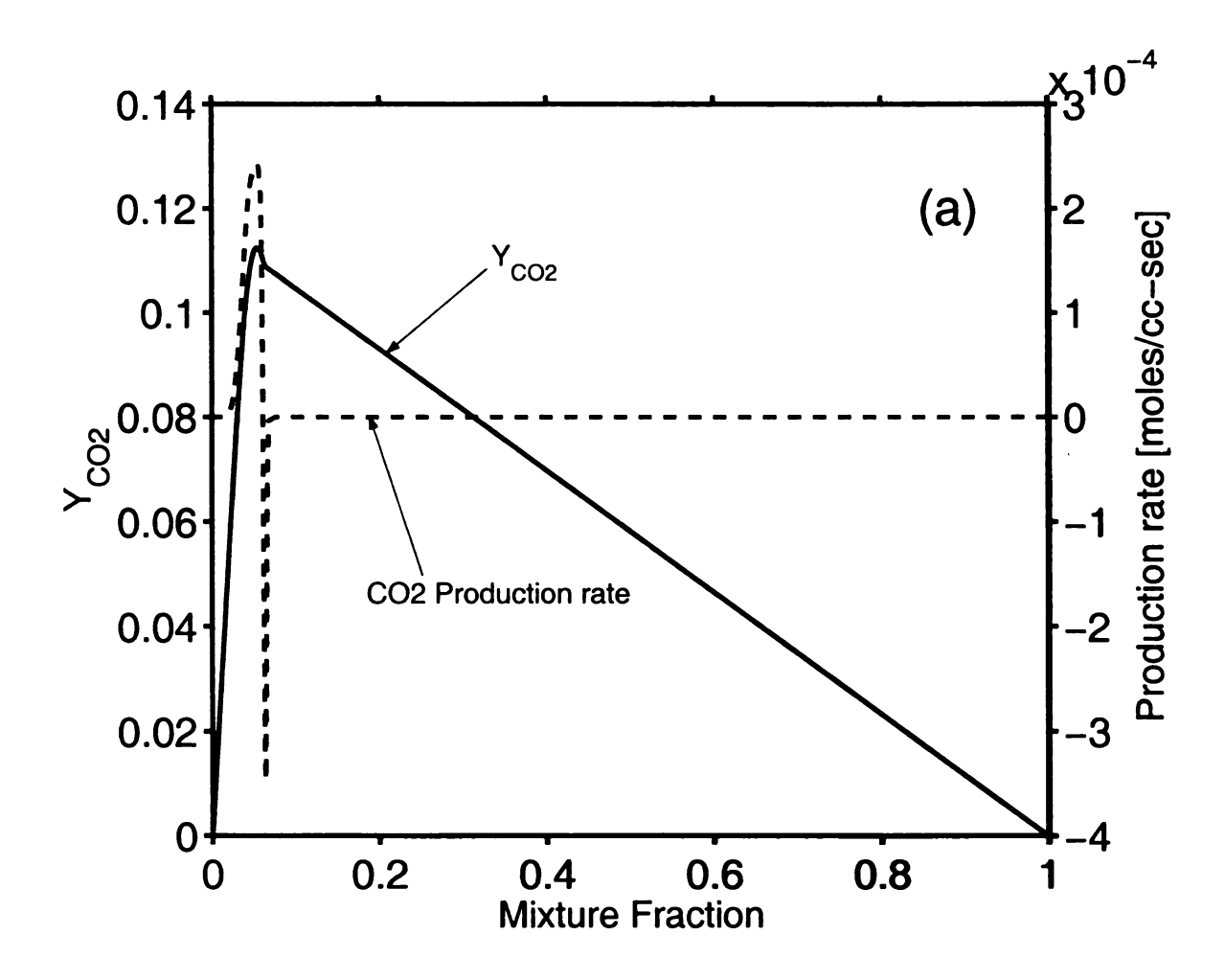


Figure 1.15. CO_2 production rate and mass fraction compared for 0% partial premixing and a strain rate of 25 1/s 4-step mechanism.

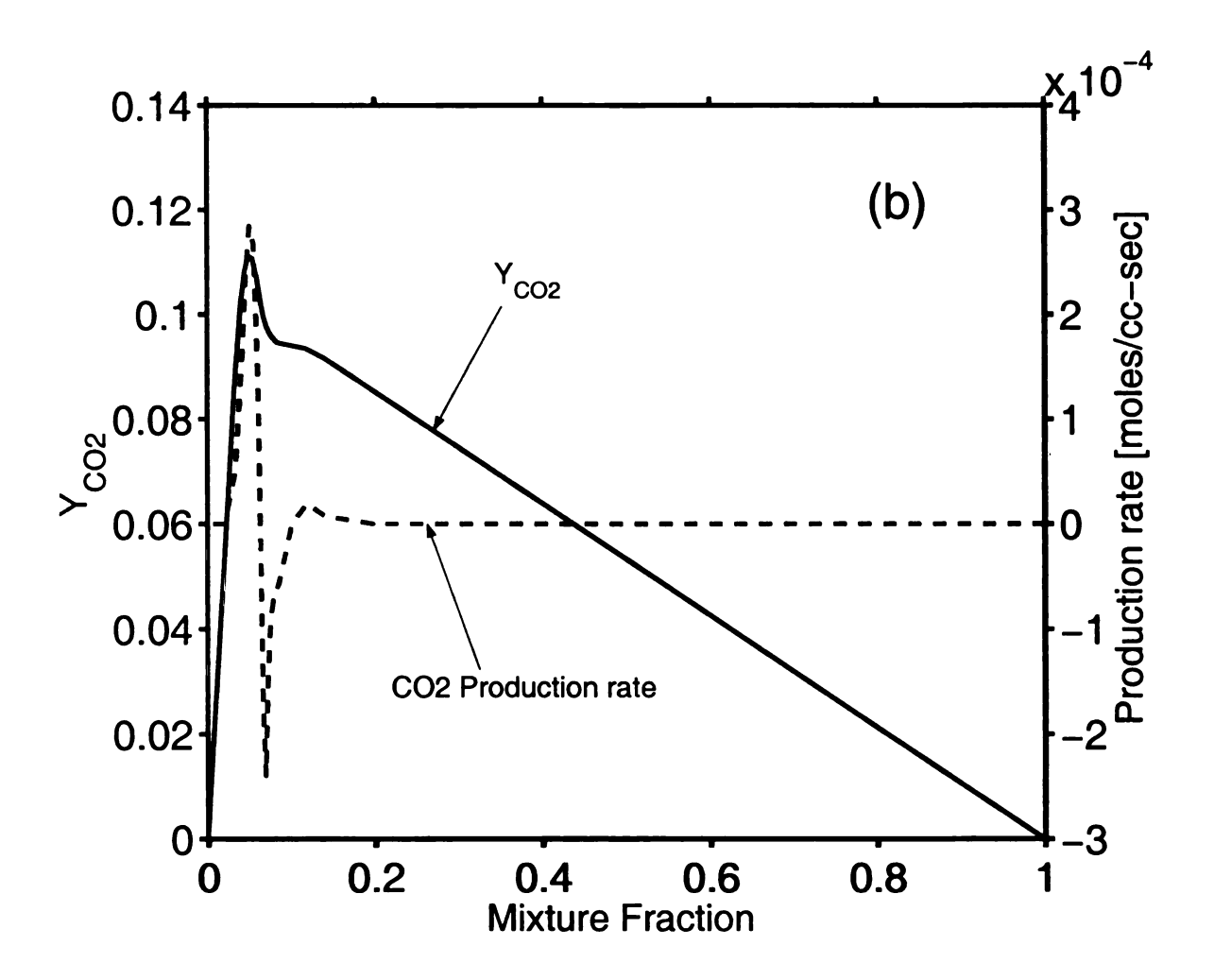


Figure 1.15. [contd...] CO_2 production rate and mass fraction compared for 0% partial premixing and a strain rate of 25 1/s 5-step mechanism.

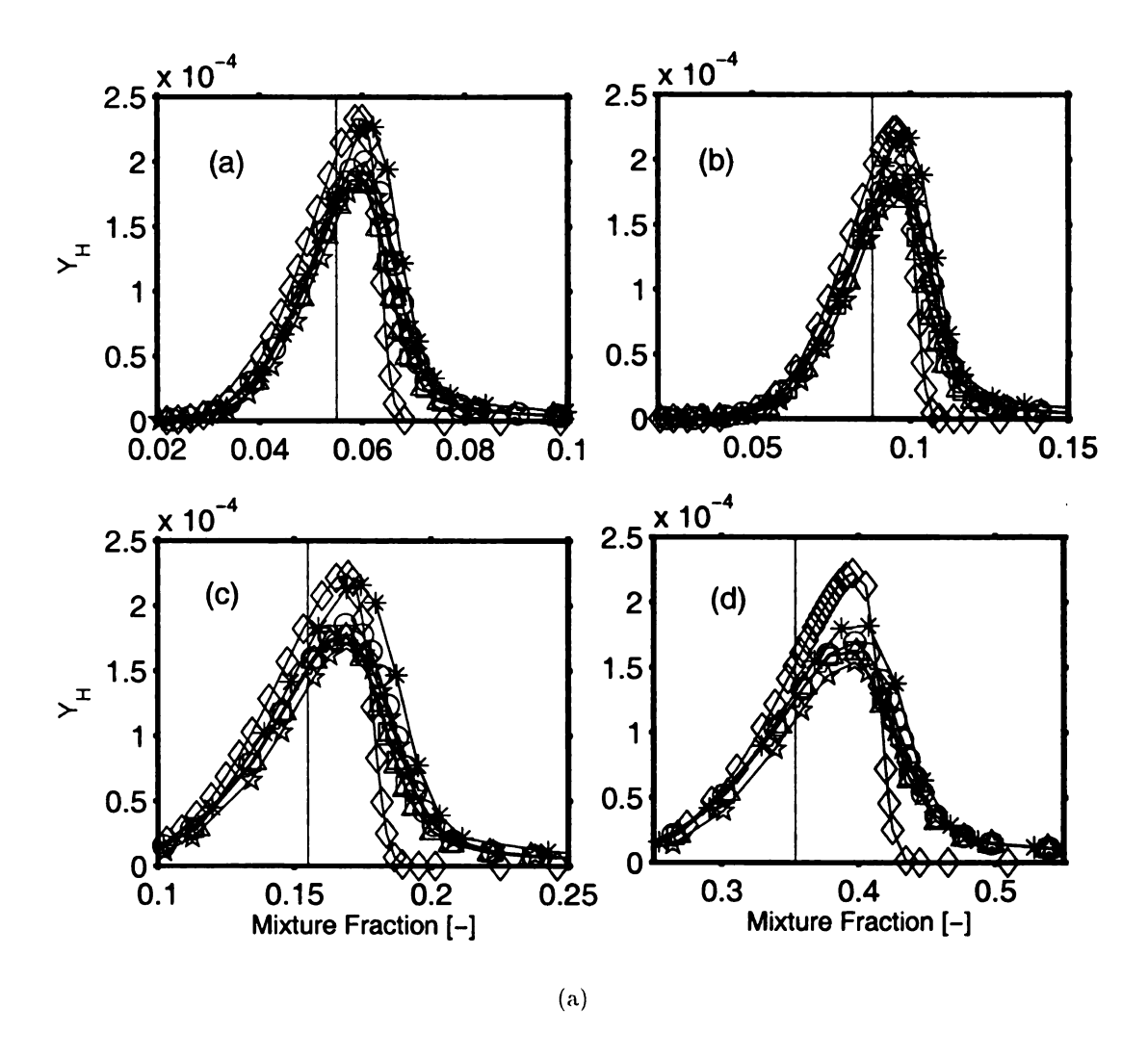


Figure 1.16. Effect of partial premixing on Y_H structure. (a) A% = 0, (b) A% = 25, (c) A% = 50, and (d) A% = 75. See Figure 1.9(a) for labeling. Vertical lines indicate stoichiometric mixture fraction.

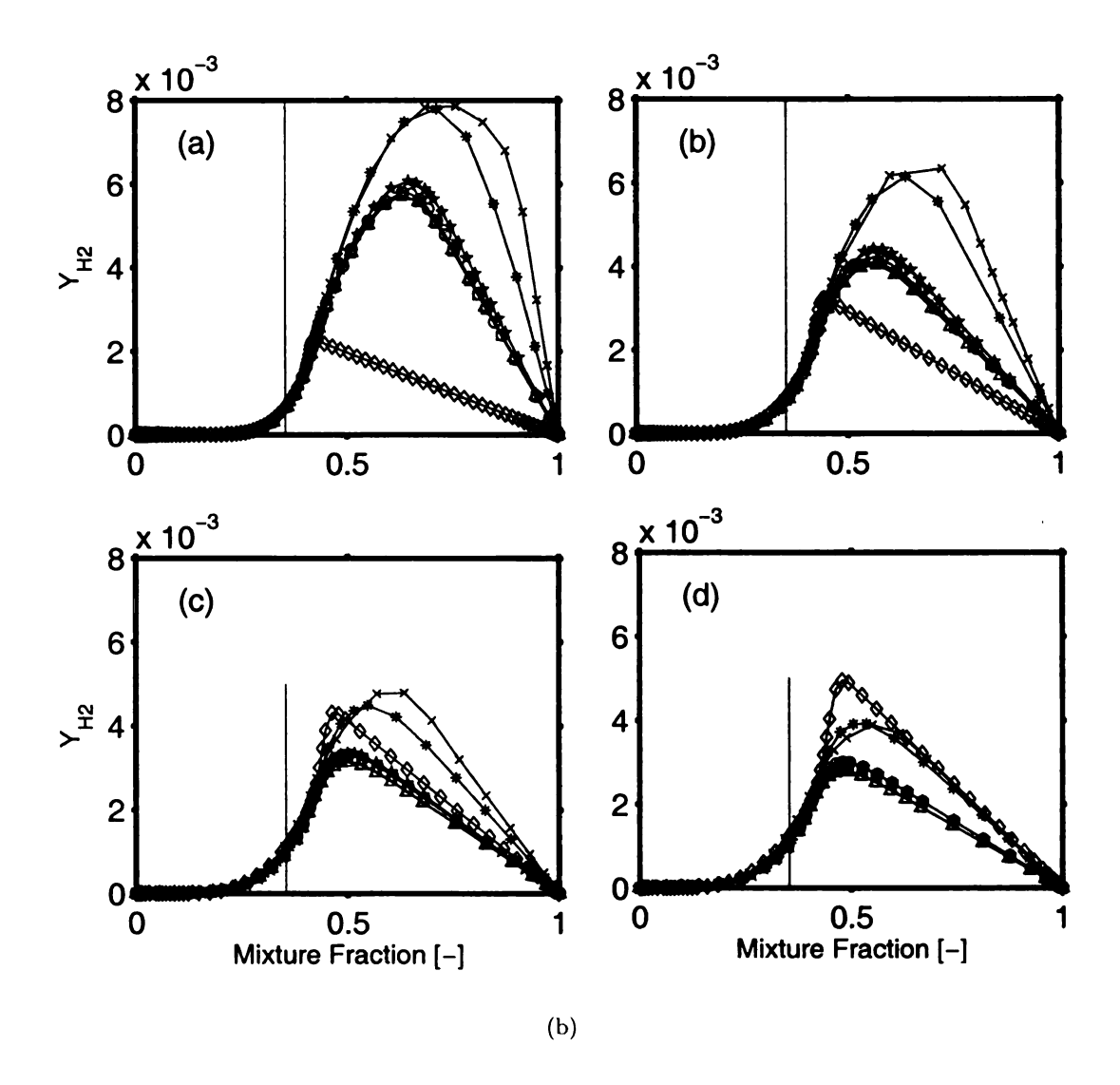


Figure 1.16. [contd...] Effect of strain rate on Y_H structure. (a) strain = 10 1/s, (b) strain = 50 1/s, (c) strain = 150 1/s, and (d) strain = 300 1/s. See Figure 1.9(a) for labeling. Vertical lines indicate stoichiometric mixture fraction.

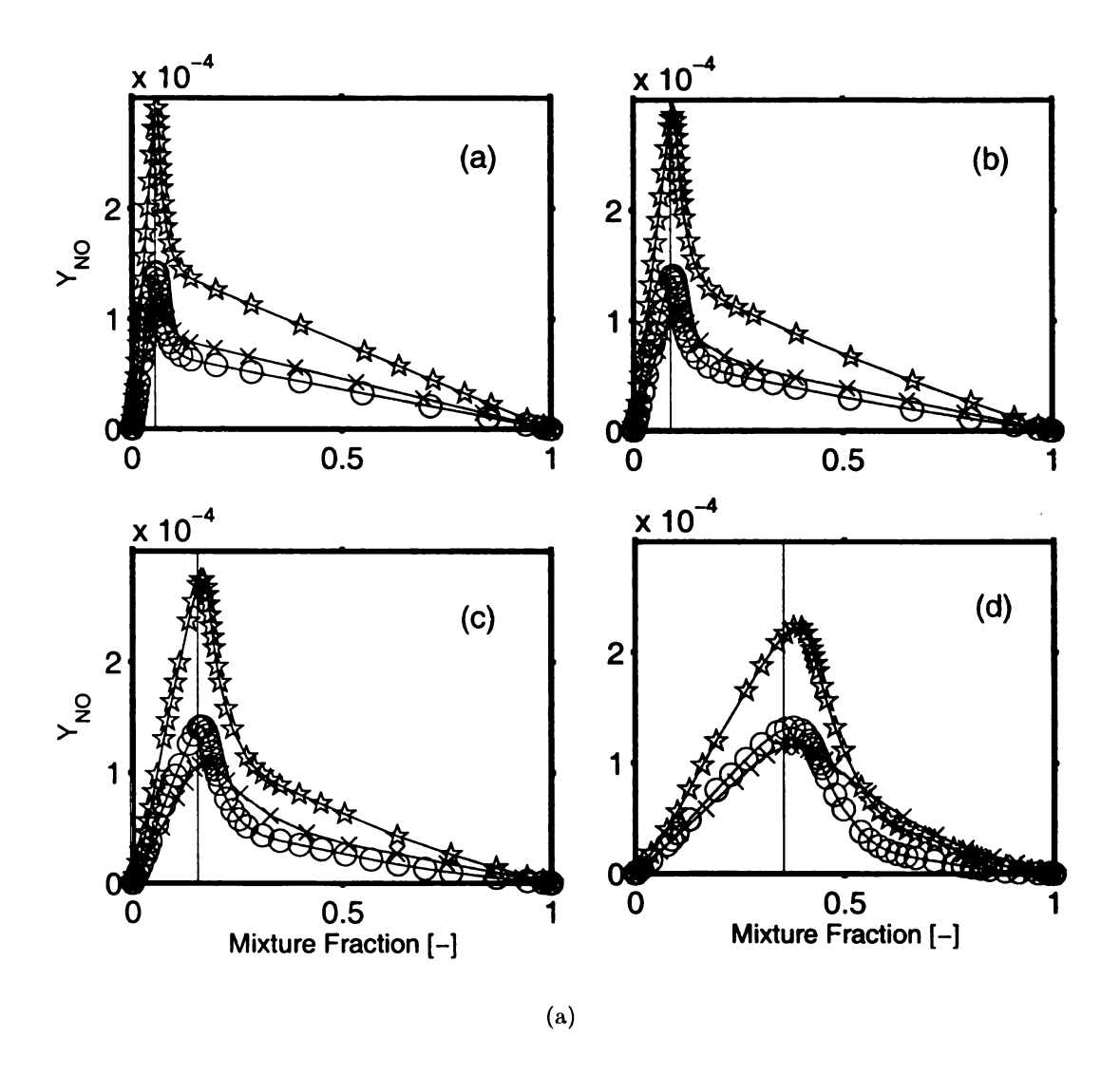


Figure 1.17. Effect of partial premixing on Y_{NO} structure. $-\times$ -, 5-Step; $-\bigcirc$ -, GRI 2.11; $-\bigstar$ -, GRI 3.0. (a) A%=0, (b) A%=25, (c) A%=50, and (d) A%=75. Vertical lines indicate stoichiometric mixture fraction.

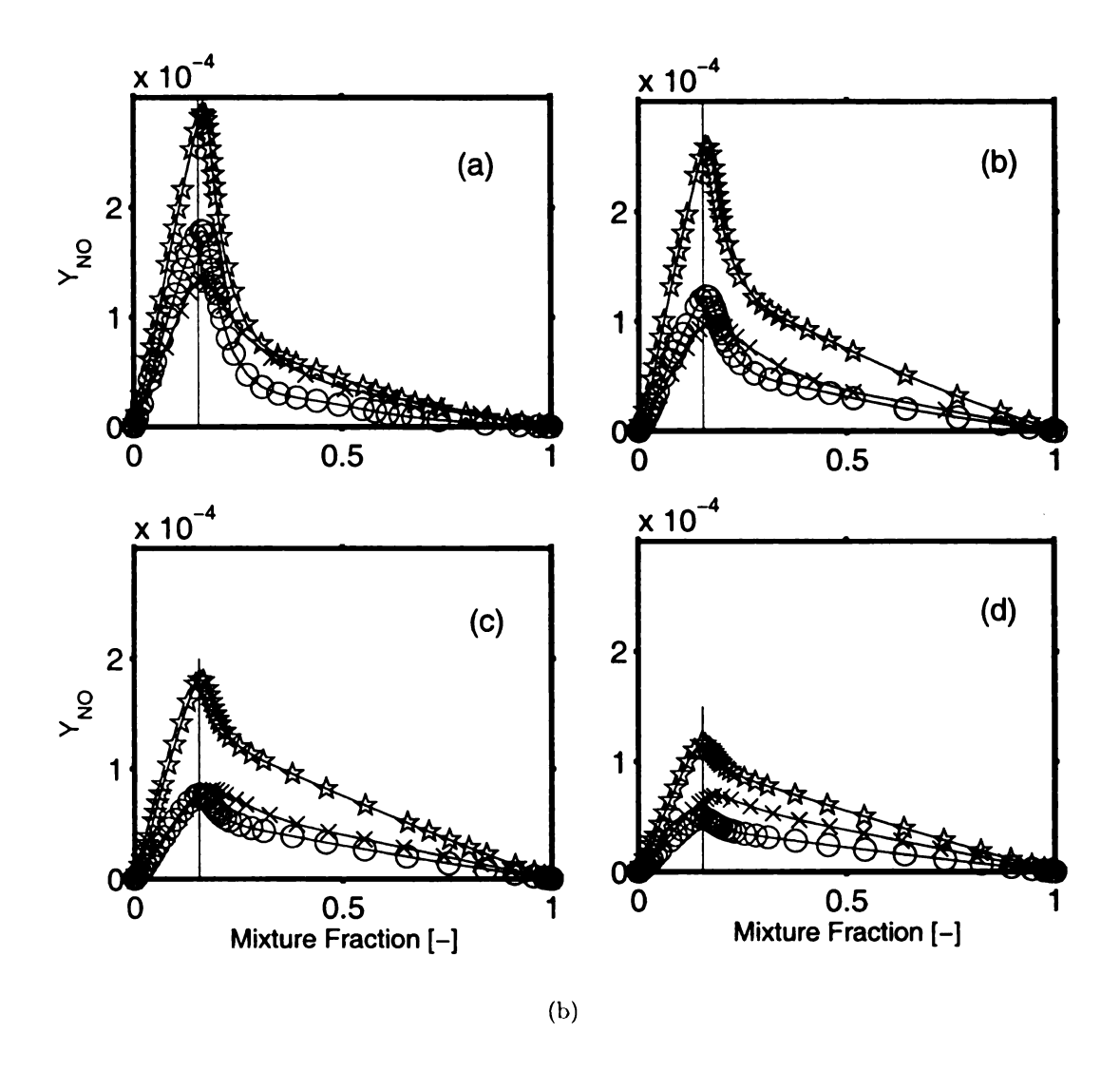


Figure 1.17. [contd...] Effect of strain rate on Y_{NO} structure. $-\times$ -, 5-Step; $-\bigcirc$ -, GRI 2.11; $-\bigstar$ -, GRI 3.0. (a) strain = 10 1/s, (b) strain = 50 1/s, (c) strain = 150 1/s, and (d) strain = 300 1/s. Vertical lines indicate stoichiometric mixture fraction.

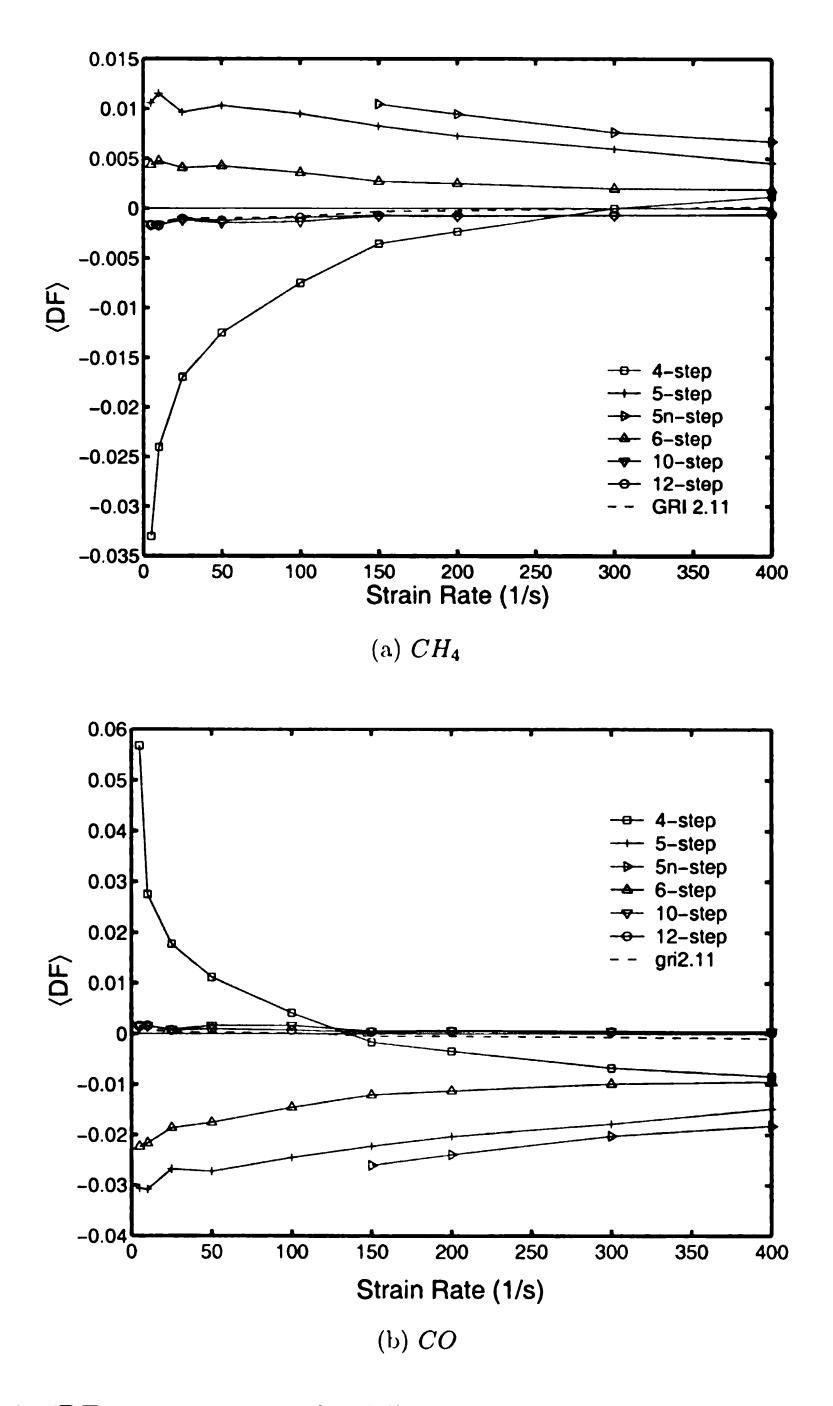


Figure 1.18. $\langle DF \rangle$ vs. strain rate for different mechanisms and premixing of 75% air in fuel stream. (a) CH_4 , (b)CO.

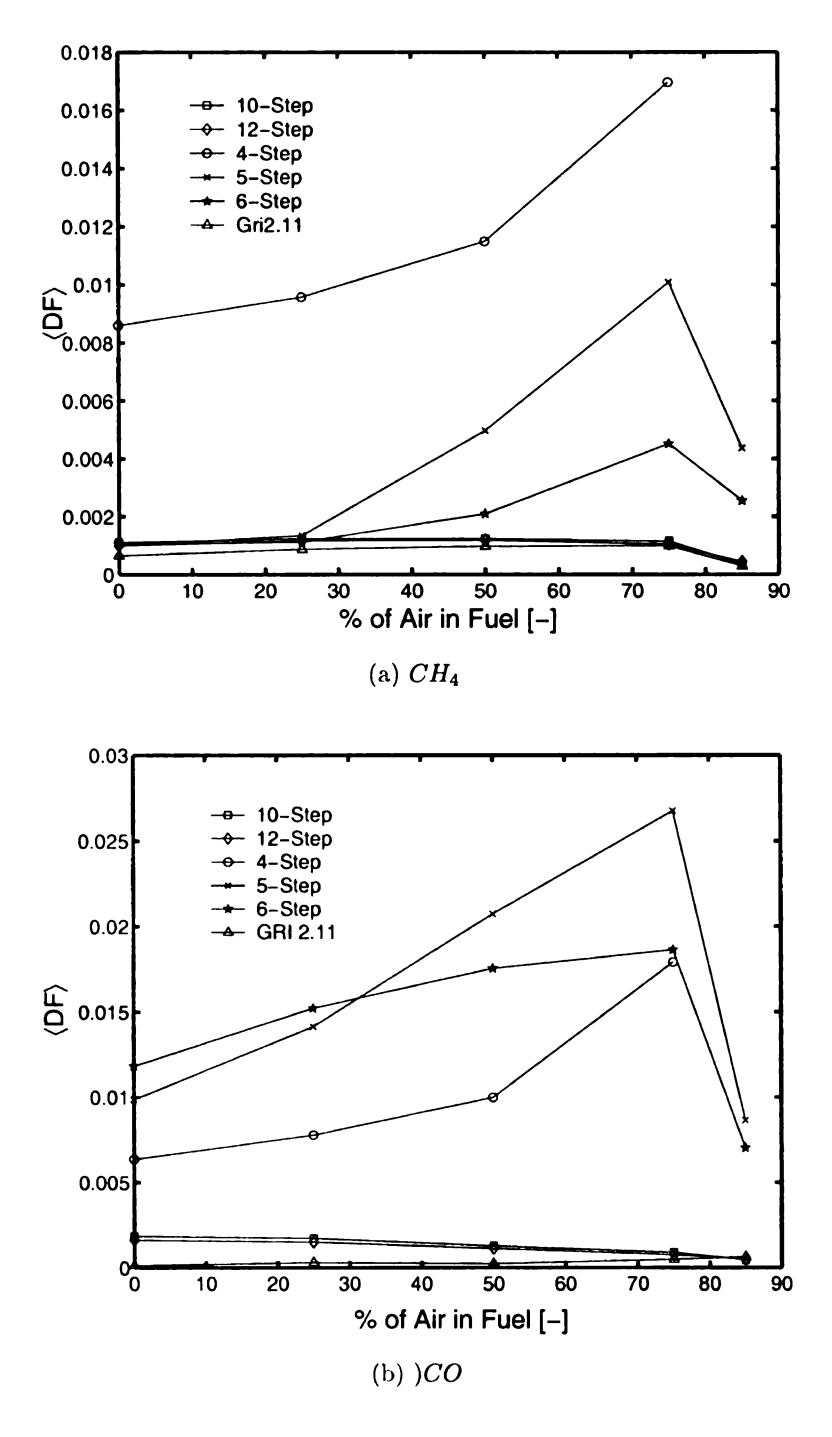


Figure 1.19. $\langle DF \rangle$ vs. partial premixing level of fuel with air for different mechanisms and strain rate of 25(1/s). (a) CH_4 , (b) CO.

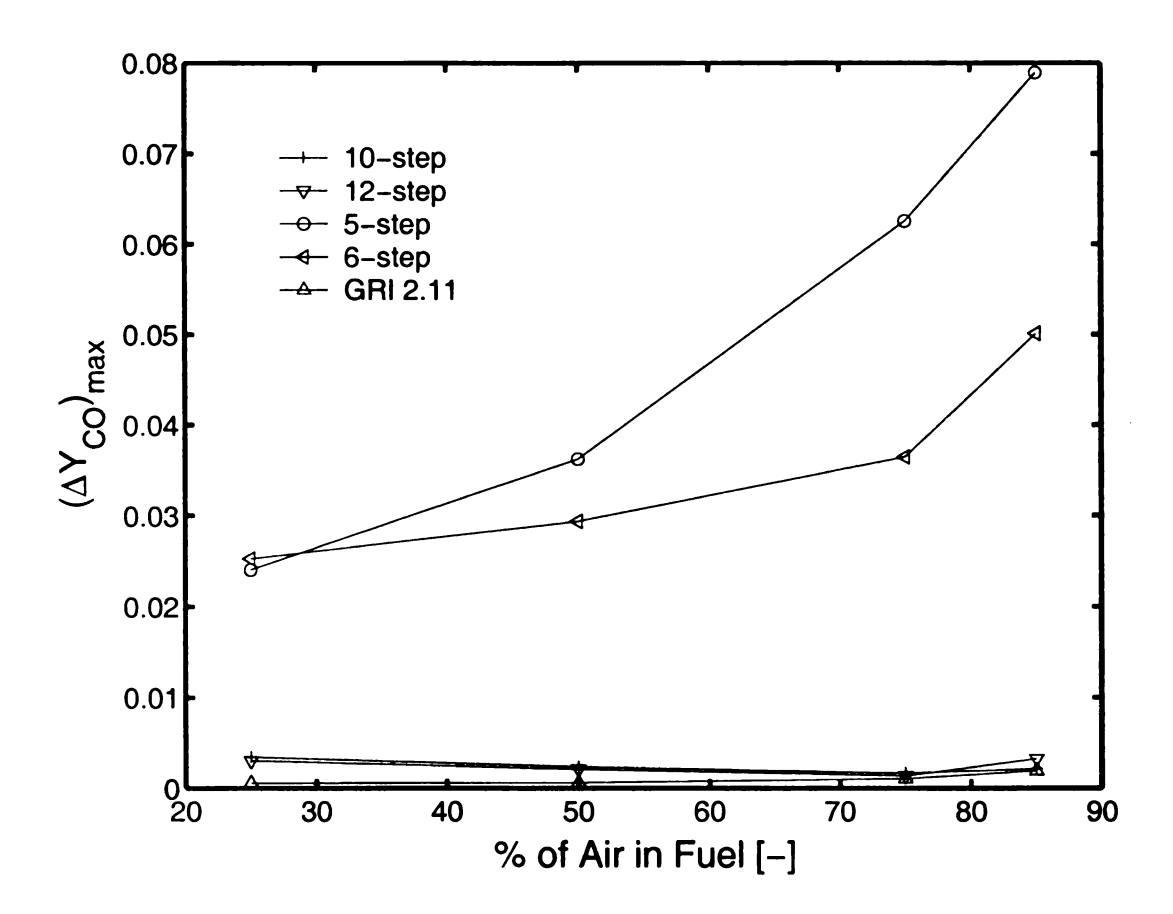


Figure 1.20. Maximum Y_{CO} difference between the GRI 3.0 results with those obtained with other mechanisms.

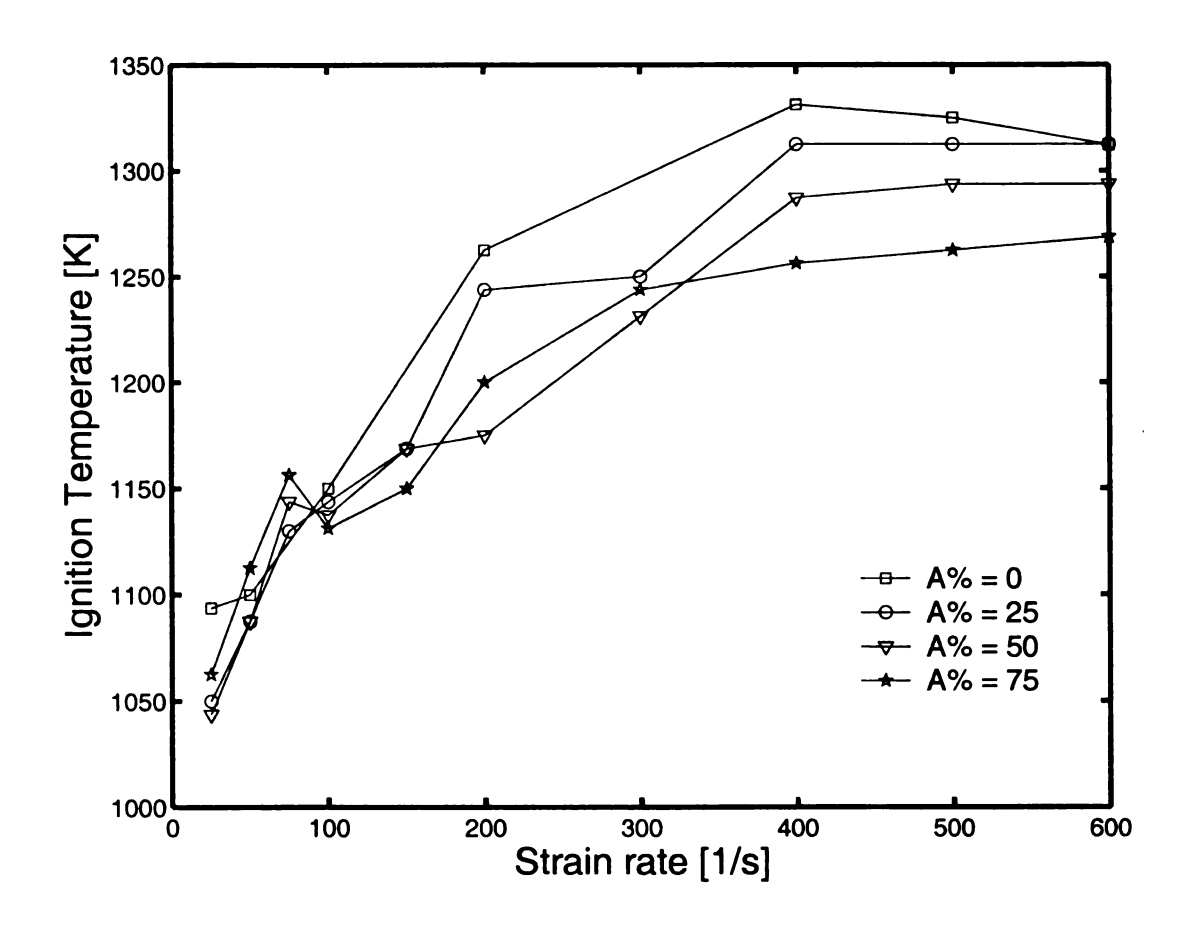


Figure 1.21. Ignition temperature vs. strain rate for various premixing levels of the fuel with air using GRI 3.0.

CHAPTER 2

Turbulent Flames

2.1 Introduction

Turbulent flows are characterized by a large number of length scales and time scales depending on the Reynolds number of the flow. For each dimension that exists in the flow, scale separation grows proportional to $Re^{3/4}$. Combustion occurring in turbulent flows further adds chemical scales to the flow scales. Depending on the interactions between flow and chemical scales, a diagram of combustion regimes can be constructed, and the combustion can be modeled using various methodologies [43, 27, 35, 44]. A diagram illustrating the different regimes of non-premixed combustion in " $Re_t - Da$ " space is shown in Figure 2.1 [56]. Da is Damköhler number which represents the ratio of turbulent to chemical time scales, and Re_t is the turbulence Reynolds number, which compares turbulent transport to molecular transport.

Non-premixed turbulent combustion occurs in many of the practical applications where the fuel and oxidizer enter the combusting region separately. Combustion rate is enhanced by strong turbulent mixing, where more efficient mixing of reactants is possible [45]. Many of the industrial applications use non-premixed combustion since unmixed fuel and oxidizer are safer to handle. Consequently, there has been considerable interest in the study of non-premixed turbulent combustion. A vast

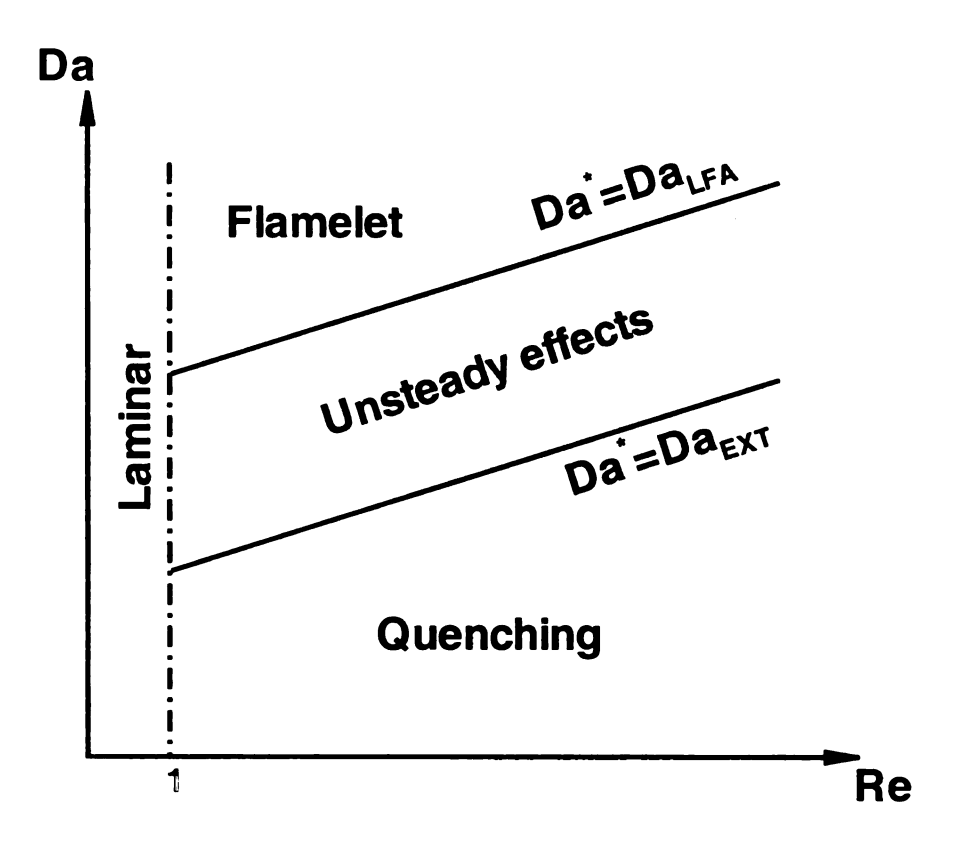


Figure 2.1. Combustion regimes for non-premixed flame

amount of literature has accumulated on this subject which includes analytical, numerical and experimental studies.

A complete description of regimes in non-premixed combustion is difficult since it does not exhibit any intrinsic characteristic scales [43]. A description based on the work of Cuenot and Poinsot [16] will be given here. Two limiting Damköhler numbers, Da_{LFA} and Da_{ext} , can be identified from their flame/vortex interaction

studies, which will be used to describe the combustion regimes. When Da^* is greater than Da_{LFA} , the flame front is assumed to be a steady laminar flame which is not affected by the vortices. Here, Da^* represents the Damköhler number for laminar diffusion flame $(Da^* \approx \frac{1}{\chi_{st}\tau_c})$, where χ_{st} is the dissipation rate at stoichiometry and τ_c is the chemical time scale. The flame front will be quenched when $Da^* \leq Da_{ext}$. Unsteadiness is observed in the intermediate range.

These regimes can also be explained based on different scales that exist in the reactive flows. Reaction zones are embedded inside the mixing layer of fuel and oxidizer, and the mixing region length is roughly the order of turbulent integral length scale $(l_t \approx l_z \approx |\nabla \tilde{z}|)$. Diffusive thickness, controlled by Kolmogorov scales, can approximated to depend on diffusion coefficient (D_{st}) and conditional mean of scalar dissipation rate, conditioned upon $Z = Z_{st}$: $l_d \approx \left(\frac{D_{st}}{\tilde{\chi}_{st}}\right)^{1/2} \approx \eta_k$. Flow time scale can be defined using the conditioned scalar dissipation rate as: $\tau_f \approx \frac{1}{\tilde{\chi}_{st}} \approx \tau_k$. A summary of different scales of reactive layer along with the diffusive layer (which is controlled by the Kolmogorov scales) is given in Table 2.1.

Table 2.1. Characteristic scales in turbulent non-premixed flames

	Length scale	Time scale	Velocity scale
Diffusive layer	$l_d pprox \left(rac{D_{st}}{ar{\chi}_{st}} ight)^{1/2}$	$ au_f pprox rac{1}{ ilde{\lambda} s t}$	l_d/ au_f
Reactive layer	$l_r = l_d (Da)^{-1/a} [29]$	$ au_c = 1/(Da\tilde{\chi}_{st})$	l_r/ au_c

At lower Reynolds numbers, we will have laminar flames. If the Reynolds number is high and when the chemistry is fast, the chemical time scale (τ_c) is small and Damköhler number large, which implies $l_r \ll l_d \approx \eta_k$. In this case the flame is thin and laminar ('flamelet'), and it will not be effected by turbulence. For larger values of τ_c , the length scale of reactive layer will be comparable to the Kolmogorov length scale, which makes the turbulence affect the reaction zone. For further larger values of τ_c or lower Damköhler numbers, the chemistry can not withstand the turbulent

fluctuations and extinctions occur.

Numerical simulations of flows that can resolve all the scales in complex geometries with complex chemistry seem to be impractical in the near future [45]. Combustion modeling approaches that utilize the simplifying characteristics of different regimes have been devised to simulate such flows. But, it is not always the case that all the points in the physical space of interest obey the same combustion regime characteristics. Direct numerical simulations (DNS) has recently emerged as a important tool in validating existing models and improving them, and understanding fundamentals of turbulent combustion [55]. In DNS of turbulent reacting flows, equations of hydrodynamic field and scalar field are solved on a fine grid, which resolves all flow and chemical scales.

Due to formidable requirements of computational power, direct numerical simulations are performed for various simplifying situations depending on the interest of study. In the choice for solving hydrodynamics equations, depending on applicability, incompressible, low Mach number or full compressible equations can be chosen. Along with the simplifications mentioned for flow field, different degrees of simplification in describing chemistry, from one-step global description to full mechanisms, and computing the transport properties can be utilized [20]. Another valuable simplification that seems to be valid in reacting flows is performing simulations in two-dimensions. Confirmation is obtained from three-dimensional direct simulations that flame structures exist in two-dimensions with a higher probability even though the flow itself is three-dimensional [4, 41, 31].

The advantage in performing simulations in two-dimensions is significant as the computational costs associated with them are much less compared to three-dimensional simulations. Jaberi and James [22] have studied the interactions between chemical reaction and turbulence in compressible two-dimensional homogeneous flows. Both isothermal and exothermic non-premixed combustion reactions are considered for

their study. Significant increase in the fluctuations of density, pressure, temperature and dilatational term is seen due to non-uniform heat release. Angoshtari [1] studied two-dimensional premixed methane flames using three different reduced reaction mechanisms, 1-step, 5-step and 12-step, for strain and curvature effects on the flame. She concluded the 12-step reduced reaction mechanism to perform better in predicting the tear-offs and pocket formations. Maas and Thévenin [31] extracted data from two-dimensional DNS of turbulent non-premixed hydrogen-air flame for determining local Intrinsic Low Dimensional Manifolds (ILDMs).

In this work we perform direct simulations of two-dimensional turbulence interacting with initially laminar methane flame. Effects of turbulence on chemical reactions and vice versa are studied for different flame thickness, premixing levels of fuel, and turbulent intensities. Laminar solution is obtained using the counterflow diffusion flame code for a very low strain rate. Chemistry is modeled using the 10-step reduced reaction mechanism of methane combustion which has been reduced from GRI-Mech 2.11. It represents methane combustion with ten reaction steps involving 14 species. Laminar studies have been used to determine that this mechanism represents the combustion accurately at various strain rates and various levels of premixing with minimum number of species (see chapter 1). This will greatly reduce the computational costs as the number of species transport equations to be solved have reduced without sacrificing much in accuracy.

Following this introduction, section 2 describes the governing equations that are required to solve in turbulent reacting flows along with the thermodynamic, transport, and chemistry models to close them. Section 3 briefly describes the numerical methodology used in this study. Section 4 describes the laminar flames that are required for the initialization of the direct numerical simulations and followed by a description of turbulent flames and DNS results.

2.2 Governing Equations for Reacting Flows

In this section the governing differential equations for turbulent reacting flows will be briefly described. For complete description of these equations the reader is referred to the textbooks on the subject [43, 59]. Description of thermodynamic, transport and chemistry models will be provided that are needed to close the system of "hydrodynamic" and scalar equations. The equations will be solved for ρ , two components of velocity, u_i , total energy, species mass fractions, Y_k , and pressure. Continuity equation gives ρ , momentum equations in two directions give the two velocity components, total energy and species equations give total energy and species mass fraction, and pressure can be obtained from equation of state. All equations are coupled.

2.2.1 Conservation Equations

The equation representing the conservation of mass is:

$$\frac{\partial \rho}{\partial t} + \frac{\partial (\rho u_i)}{\partial x_i} = 0 \tag{2.1}$$

where ρ is the density of mixture and u_i is the component of velocity.

The equation of momentum is similar to Navier-Stokes equation for non-reacting case:

$$\frac{\partial(\rho u_i)}{\partial t} + \frac{\partial(\rho u_i u_j)}{\partial x_i} = -\frac{\partial p}{\partial x_i} + \frac{\partial \tau_{ij}}{\partial x_j} + \rho f_i \qquad (i = 1, 2)$$
(2.2)

where p is the pressure, τ_{ij} is the viscous stress tensor components, and f_i is the external force in *i*th direction. Even though explicit reaction terms does not appear in these equations, combustion will modify the hydrodynamic field by changing the temperature dependent viscosity μ , which will appear in the closure model for τ_{ij}

and by changing the density. The typical variation of these quantities will be in a ratio of 1:8. As a consequence the local Reynolds number varies more compared to the non-reacting case.

There are many variations for energy equation depending upon the variable chosen for solving (enthalpy, internal energy, total energy, etc.). A complete list of variables that are solved for and their derivation is given in reference [43]. Here in this study we use the total energy as our variable and the equation is:

$$\frac{D(\rho e_t)}{Dt} = \frac{\partial(\rho e_t)}{\partial t} + \frac{\partial(\rho u_j e_t)}{\partial x_j} = -\frac{\partial q_j}{\partial x_j} + \frac{\partial \sigma_{ij} u_i}{\partial x_j} + Q_e + \rho \sum_{k=1}^K [Y_k f_{k,j} (u_j + V_{k,j})] \quad (2.3)$$

where q_j is the component of heat flux vector in jth direction, Q_e is the external source of energy (like spark ignition source), σ_{ij} is the stress tensor, and $f_{k,j}$ is the body force on species k in jth direction. The last term represents the power generated due to the volume force f_k on species k.

Different simplifications for this equation is possible depending on the assumptions like constant pressure (low Mach number), equal heat capacities for all species. In this study we solve the full equation without any simplifications.

For each species present in the system we need to solve a species balance equation given by:

$$\frac{\partial(\rho Y_k)}{\partial t} + \frac{\partial(\rho u_j Y_k)}{\partial x_j} = -\frac{\partial(\rho Y_k V_{k,j})}{\partial x_j} + \dot{\omega}_k \qquad (k = 1, ..., K)$$
 (2.4)

where K is the total number of species present, $V_{k,j}$ is the jth component of diffusion velocity for species k, and $\dot{\omega}_k$ is the rate of mass poduction/destruction per unit volume for species k.

The above system of partial differential equations given in Eqs. 2.1 - 2.4 solve

for density ρ , the velocity components u_j , the K species mass fractions Y_k , and the total energy e_t . This system of equations are not closed in this form and relations are needed to express species enthalpies and the relation between pressure and mixture composition. Expressions for viscous stress tensor, the heat flux vector, and diffusion velocities are also needed. And most importantly, we need a closure model for the rate of mass production, $\dot{\omega}_k$. In this section we give the expressions that are required for closing the above set of equations.

In this study we assume that the gas obey the perfect gas law. This assumption is valid in most of the combustion applications which assume low pressure and high temperatures. The gas law gives a relation between pressure, temperature, and local mixture composition as:

$$p = \rho \frac{\bar{R}}{\bar{W}} T \tag{2.5}$$

where \bar{R} is the universal gas constant whose value if $R=8.314 Jmol^{-1}K^{-1}$ and \bar{W} is the mixture averaged molar mass given by

$$\bar{W} = \left(\sum_{k=1}^{K} \frac{Y_k}{W_k}\right)^{-1} \tag{2.6}$$

The variant of energy variable that is solved in this study can be expressed as:

$$e_t = h - p/\rho + \frac{1}{2}u_i u_i \tag{2.7}$$

where h is the enthalpy of the mixture and the last term is the kinetic energy. The mixture enthalpy h can be evaluated from the species enthalpies by:

$$h = \sum_{k=1}^{K} h_k Y_k \tag{2.8}$$

The specific enthalpy of species k is given by two parts: sensible and chemical. The

chemical part is the enthalpy that is required for the formation of the species at some reference temperature (usually taken to be 298.15 K). The sensible part will be computed from the specific heat of the species. The complete relation for species enthalpy is:

$$h_k(T) = \int_{T_0}^T C_{pk}(T)dT + \Delta h_{f,k}^o$$
(2.9)

where C_{pk} is the specific heat capacity of species k and the second term is the chemical part of the enthalpy. The values of specific enthalpy of formation are available in tables and the dependence of specific heat capacities on temperature are available in the form of polynomial functions. In this study we used the CHEMKIN thermodynamic database [24] for their values. C_{pk} is given in the NASA chemical equilibrium format:

$$\frac{C_{pk}}{\bar{R}} = a_{1k} + a_{2k}T_k + a_{3k}T_k^2 + a_{4k}T_k^3 + a_{5k}T_k^4$$
 (2.10)

where $a_{1k} - a_{5k}$ are the coefficients and T_k is the temperature of the species k.

2.2.2 Transport Models

The fluids encountered in most of the practical combustion applications are Newtonian. In this study we assume the fluid to be Newtonian also and thus the viscous stress tensor used in Eq. 2.2 can be approximated as:

$$\tau_{ij} = \mu \left[\frac{\partial u_i}{\partial x_j} + \frac{\partial u_j}{\partial x_i} \right] + \left(\kappa - \frac{2}{3} \mu \right) \frac{\partial u_k}{\partial x_k} \delta_{ij}$$
 (2.11)

where μ is the coefficient of viscosity, κ is the bulk viscosity and δ_{ij} is the Kroenecker delta. Bulk viscosity can be neglected on the basis of low-Mach number approximation. Usually the stress tensor as it appears in Eq. 2.3 can be written as the sum of pressure term and the viscous stress term:

$$\sigma_{ij} = -p\delta_{ij} + \tau_{ij} \tag{2.12}$$

The coefficient of strain term μ that appears in Eq. 2.11 is the mixture viscosity and it is calculated from the pure species viscosity by Wilke's formula [57] combined with the modification of Bird [9] as:

$$\mu = \sum_{k=1}^{K} \frac{X_k \mu_k}{\sum_{j=1}^{K} X_j \Phi_{kj}}$$
 (2.13)

where μ_k is the pure species viscosity, X_k is the mole fraction of species k and Φ_{kj} will be given by:

$$\Phi_{kj} = \frac{1}{\sqrt{8}} \left(1 + \frac{W_k}{W_j} \right)^{-1/2} \left(1 + \left(\frac{\mu_k}{\mu_j} \right)^{1/2} \left(\frac{W_j}{W_k} \right)^{1/4} \right)^2 \tag{2.14}$$

Pure species viscosity μ_k is obtained from [23]:

$$\mu_k = \frac{5}{16} \frac{\sqrt{\pi m_k k_B T}}{\pi \sigma_k^2 \Omega^{(2,2)^*}} \tag{2.15}$$

where σ_k is the Lennard-Jones collision diameter, m_k is the molecular mass, K_B is the Boltzman constant, and T is the temperature. The collision integral $\Omega^{(2,2)^*}$ is determined by a quadratic interpolation of the tables based on Stockmayer potentials given in Monchick and Mason [34]. A fourth degree polynomial is obtained as a function of temperature and the coefficients are tabulated for the pure species viscosity based on the description given above.

The heat flux in *i*th direction is given by:

$$q_i = -\lambda \frac{\partial T}{\partial x_i} + \sum_{k=1}^K [\rho h_k Y_k V_{k,i}]$$
 (2.16)

here λ is the thermal conductivity of the mixture. The first term is the Fourier

heat conduction term and the second term is the heat transport due to differential diffusion of species. In the above equation heat flux due to radiation and Dufour effect has been neglected.

The mixture-averaged thermal conductivity is calculated using the formula:

$$\lambda = \frac{1}{2} \left[\sum_{k=1}^{K} X_k \lambda_k + \left(\sum_{k=1}^{K} \frac{X_k}{\lambda_k} \right)^{-1} \right]$$
 (2.17)

here λ_k is the pure species thermal conductivity of species k which are calculated and the temperature dependent polynomial fit coefficients are tabulated similar to that of viscosity.

The complete general form of expression for diffusion velocity of the species i can be given as:

$$\mathbf{V}_{i} = -\sum_{k=1}^{K} D_{ik} \left[\nabla X_{k} + (X_{k} - Y_{k}) \frac{\nabla p}{p} + \frac{\rho}{p} \sum_{j=1}^{K} Y_{k} Y_{j} (\mathbf{f}_{j} - \mathbf{f}_{k}) \right] - D_{i}^{T} \frac{\nabla T}{T}$$
(2.18)

where D_{ik} is the multi-component diffusion coefficient, which is dependent on all the state variables. The term involving the thermal diffusion coefficient of species i (D_i^T) is known as Soret effect (thermodiffusion). This term gives the diffusion of species due to thermal gradients. This expression for the diffusion velocity is computationally very intensive and will not be used here. A computationally less intensive yet enough accurate formula will be used in this study. Diffusion velocity is then obtained from:

$$V_{k,i} = -D_{km} \frac{\partial X_k}{\partial x_i} \tag{2.19}$$

where the diffusion coefficient is for species k in to the mixture, and it will be calculated from the mixture-averaged formula (Zeroth order approximation) [21]:

$$D_{km} = \frac{1 - Y_k}{\sum_{j=1, j \neq k}^{K} X_j / D_{kj}}$$
 (2.20)

where D_{kj} is the diffusion coefficient for species k in species j. The diffusion velocity calculated by this formula does not obey the global mass conservation equation,

$$\sum_{k=1}^{K} Y_k V_{k,i} \neq 0 \tag{2.21}$$

To overcome this problem, a correction term will be added for all the species, which is given by:

$$V_{c,k} = -Y_k \sum_{k=1}^{K} V_{k,i}$$
 (2.22)

In order to calculate the binary coefficients a fourth degree polynomial was fitted to the data obtained from CHEMKIN for all the species involved in the simulation in the temperature range from 250K - 5000K.

2.2.3 Chemistry Models

Let the K species in the system react amongst themselves through R reactions. Then, the the reactions can be represented in a compact form as:

$$\sum_{k=1}^{K} \nu'_{rk} A_k = \sum_{k=1}^{K} \nu''_{rk} A_k \qquad r = 1, 2, ..., R$$
 (2.23)

where A_k is the chemical symbol for the species k, ν'_{rk} and ν''_{rk} are the molar stoichiometric coefficients of species k in reaction r. The conservation of mass for each reaction implies that the stoichiometric coefficients satisfies the following relation

$$\sum_{k=1}^{K} \nu'_{rk} W_k = \sum_{k=1}^{K} \nu''_{rk} W_k \tag{2.24}$$

The progress rate for the rth reaction will be given as:

$$w_r = k_{fr} \prod_{k=1}^{K} \left[\frac{\rho Y_k}{W_k} \right]^{\nu'_{rk}} - k_{br} \prod_{k=1}^{K} \left[\frac{\rho Y_k}{W_k} \right]^{\nu''_{rk}}$$
(2.25)

where k_{fr} and k_{br} are the forward and backward reaction rates for reaction r, and are expressed by Arrhenius law:

$$k_{fr} = A_{fr} T^{\beta fr} \exp\left(-\frac{E_{a,fr}}{\bar{R}T}\right)$$
 (2.26)

here A_{fr} is the pre-exponential coefficient, β_{fr} is the temperature exponent, $E_{a,fr}$ is the activation energy for the forward reaction r, and \bar{R} is the universal gas constant. Forward and backward reaction rates are related through the equilibrium constant of that reaction

$$K_{e,r} = \frac{k_{fr}}{k_{br}} \tag{2.27}$$

and

$$K_{e,r} = \left(\frac{p_a}{\bar{R}T}\right)^{\sum_{k=1}^{K} \nu_{kr}} \exp\left[\frac{\Delta S_r^o}{\bar{R}} - \frac{\Delta H_r^o}{\bar{R}T}\right]$$
(2.28)

where p_a is the atmospheric pressure, ΔS_r^o and ΔH_r^o are the changes in the entropy and enthalpy respectively during the transformation of reactants to products for reaction r, and $\nu_{kr} = \nu'_{kr} - \nu''_{kr}$. The mass reaction rate of species k is then

$$\dot{\omega}_k = W_k \sum_{r=1}^R \nu_{kr} w_r \tag{2.29}$$

and the conservation of mass forces the equation:

$$\sum_{k=1}^{K} \dot{\omega}_k = 0 \tag{2.30}$$

For evaluating the sources term in Eq. 2.4 for each species we need all the reactions that describe the mechanism of conversion of reactants to products, and also need all the constants that are mentioned here for each of such reaction. The most commonly used format to describe the reaction mechanism is the CHEMKIN format.

2.3 Numerical Solution

The numerical implementation of the governing equations explained in section 2 will be given here along with the tests performed to improve the performance of some of the computationally intensive subroutines. A representation of computational domain along with the flame and the boundary conditions used is given in Figure 2.2.

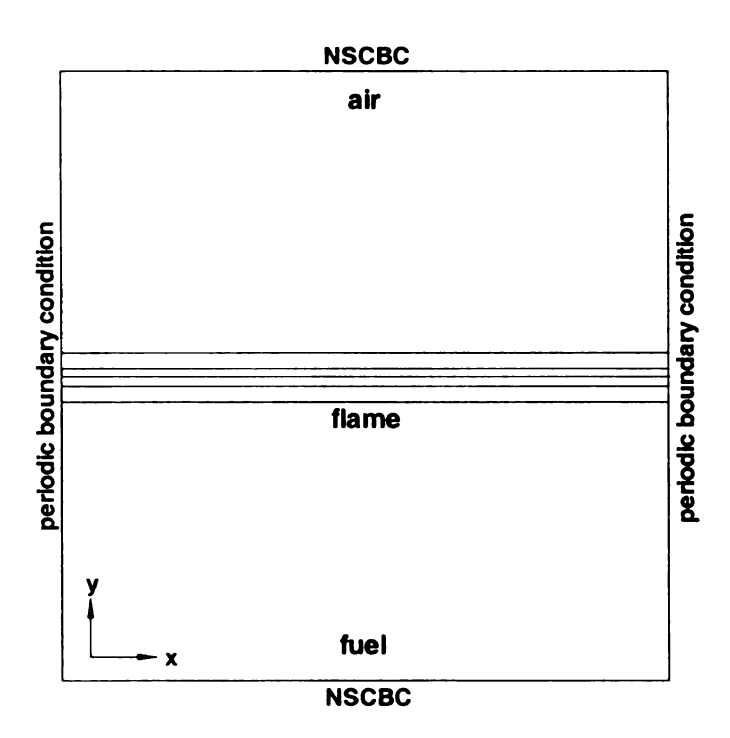


Figure 2.2. Computational Domain

2.3.1 Methodology

Equations 2.1 - 2.4 are integrated using the extended Maccormack method [25] with periodic boundary conditions on the boundary perpendicular to the flame and non-reflecting outflow boundary conditions [42, 48] on boundaries parallel to the flame. If the general equation, which represents any of the four governing equations is:

$$\frac{\partial \mathbf{U}}{\partial t} = \frac{\partial \mathbf{F}}{\partial x} + \frac{\partial \mathbf{G}}{\partial y} + \mathbf{S} \tag{2.31}$$

then symbolically the Maccormack scheme can be represented as:

Predictor pass:

$$\mathbf{U}_{i}^{*} = \mathbf{U}_{i}^{n} - \frac{\Delta t}{\Delta x} \Delta^{(1)} \mathbf{F}^{n} - \frac{\Delta t}{\Delta y} \Delta^{(2)} \mathbf{G}^{n} - \Delta t \mathbf{S}^{n}$$
(2.32)

and the corrector pass:

$$\mathbf{U}_{i}^{n+1} = \frac{1}{2} \left[\mathbf{U}_{i}^{n} + \mathbf{U}_{i}^{*} - \frac{\Delta t}{\Delta x} \Delta^{(1)} \mathbf{F}^{*} - \frac{\Delta t}{\Delta y} \Delta^{(2)} \mathbf{G}^{*} - \Delta t \mathbf{S}^{*} \right]$$
(2.33)

where $\Delta x, \Delta y$, and Δt represents the grid size in space x, y, and time t-directions, $\Delta^{(1)}$ and $\Delta^{(2)}$ are the forward or backward fourth order compact difference (Carpenter [13]) operators which are repeated in the solution procedure as given in Table 2.2. Time step Δt will be given by minimum of the chemical time step and time step calculated through CFL criteria.

Table 2.2. Differencing sequence foe wxtended Maccormack scheme

Step	Predictor		Corrector	
	$\Delta^{(1)}$	$\Delta^{(2)}$	$\Delta^{(1)}$	$\Delta^{(2)}$
1	Forward	Forward	Backward	Backward
2	Backward	Backward	Forward	Forward
3	Forward	Backward	Backward	Forward
4	Backward	Forward	Forward	Backward

The stress terms in **F** and **G** are evaluated using second-order and fourth-order central differences. The first derivative of velocity in viscous term and temperature derivative in heat flux calculation are calculated using second-order central differences, and the mass fraction gradient in the diffusion term is calculated using fourth-order central difference.

2.3.2 Simplifying Assumptions

As discussed in the introduction of this chapter, Direct Numerical Simulations are computationally intensive and valid simplifications are to be made in order to compute the solution in meaningful amount of time. A brief description of simplifications used in this thesis will be given along with the justifications in using them.

2D Turbulence

Direct simulations of three-dimensional turbulent reacting flows is a very expensive task even with the computational power available now or in the near future [45]. As the scale separation is dependent on the Reynolds number and resolution of reaction zone on Damköhler number (Da). The space in "Re-Da" plot that is accessible by 3D-DNS is limited to lower left corner, and this domain can be extended a little bit more by resorting to 2D-DNS (See Figure 4 of reference [55]). But, proper justifications are to be given before one can use two-dimensional turbulence.

The energy and enstrophy conservation equations for two-dimensional turbulence can be given as:

$$\frac{d\sigma_v}{dt} = -2\nu\Omega, \qquad \frac{d\Omega}{dt} = -\eta \tag{2.34}$$

where the total energy, enstrophy and enstrophy dissipation rate are given by

$$\sigma_v = \int_0^\infty E(k) \, dk = \frac{1}{2} \langle u_i u_i \rangle \tag{2.35}$$

$$\Omega = \int_0^\infty k^2 E(k) \, dk = \frac{1}{2} \langle \omega_i \omega_i \rangle \tag{2.36}$$

$$\eta = 2\nu \int_0^\infty k^4 E(k) \, dk = \nu \langle |\nabla \times \omega|^2 \rangle \tag{2.37}$$

and the integral and microscale length scales and Reynolds numbers based on these length scales are defined, analogous to the three-dimensional turbulence as:

$$L = \sigma_v^{\frac{1}{2}}/\eta^{\frac{1}{3}}, \qquad l = (\nu\Omega/\eta)^{\frac{1}{2}}$$
 (2.38)

and

$$Re_L = \sigma_v / (\nu \eta^{\frac{1}{3}}), \qquad Re_l = (l\Omega^{\frac{1}{2}})l/\nu$$
 (2.39)

The differences in two-dimensional turbulence and three-dimensional turbulence are that the second law in Eq. 2.34 implies that the enstrophy can not be generated by non-linear effects and are only dissipated by viscosity. Therefore, the rate of energy dissipation in decaying 2D turbulence is bounded by its initial value. In other words, there is no vortex stretching mechanism in two-dimensional turbulence and the cascade of energy transfer from large to small scales is not complete. Thus, small scales eddies are not as influential as they are in three-dimensional turbulence and they do not follow the Kolmogorov's scaling law. However, Poinsot et al [41] has shown using direct simulations of three-dimensional turbulent premixed combustion that the flame exists as locally two-dimensional sheets with more probability than as three-dimensional structure. So it is somewhat justified to use two-dimensional turbulence with combustion simulations [43].

Simplifications in evaluating molecular properties

It is observed in turbulent combustion simulations that most part of the computational time is spent in calculating molecular properties like diffusion velocity, viscosity and thermal conductivity [1, 20]. In this thesis all the pure species properties were approximated to a fourth-degree polynomial rather than being computed from the basic equations. The resulting coefficients of the polynomial are tabulated and read from a file during simulations, which has reduced a considerable amount of time.

Table 2.3. CPU time requirements for subroutines before and after approximation

No.	Subroutine	Function	% CPU	% CPU
	Name		time	time
			(Before)	(After)
1	Continuity	Solves Continuity	0.020	0.081
2	Y-Momentum	Solves Y momentum	0.013	0.084
3	Energy	Solves energy equation	0.015	0.067
4	Species Eq.	Solves species equation	0.225	1.183
5	Calc. Interm.	Updates intermediate	0.056	0.230
		values		
6	Avg. Mol. Wt.	Calculates average	0.033	0.140
		molecular weight		
7	Calc. Temp	Calculates temperature	0.174	0.972
8	Pressure	Calculates pressure	.002	0.010
9	B. Values	Imposes B. C.s	0.150	0.705
10	Stress	Calculates thermal and	86.024	8.036
		transport properties		
11	Chem. Kin.	Calculates species	13.287	88.492
		reaction rates		

Evaluating the diffusion velocities is the most expensive task as it involves equation 2.18 and solution of a system of linear equations of $3K^2$ unknowns for each grid point and at each time step. A simplification to this equation is to solve the zeroth-order approximation (or mixture-averaged) Eq. 2.20 along with Eq. 2.19. The approximation of evaluating mixture-averaged diffusion coefficient will significantly

reduce the computational time.

The other important transport property which requires huge amount of CPU time is the mixture-averaged viscosity. An acceptable simplification for mixture-averaged viscosity is:

$$\mu = \sum_{k=1}^{K} \frac{X_k \mu_k}{\sum_{j=1}^{K} X_j \Phi_{kj}} \approx \sum_{k=1}^{K} X_k \mu_k$$
 (2.40)

this approximation has been tested for premixed turbulent flames extensively and found to give good results. Before the approximation, the double summation used to take up a huge amount of time.

Table 2.3 shows the percentage of time spent in each of the subroutine in our program before and after making the simplifications in calculating the diffusion velocity and viscosity. About 86% of total computational time is spent in the subroutine "stress", and 87% of time in stress subroutine is used to calculate the diffusion coefficients as shown in Table 2.4.

Table 2.4. Percentage of CPU time in stress subroutine

No.	Subroutine	Function	% CPU	% CPU
	part		time	time
			(Before)	(After)
$\overline{1}$	Temp & Vel. Der.	Calculates velocity and	0.005	0.257
		temperature derivatives		
2	Mass Frac. Der.	Calculates mass	0.126	10.195
		fraction derivatives		
3	Enthalpy	Calculates Enthalpy	0.074	4.161
4	Viscosity	Calculates viscosity	12.192	3.114
5	Diffusion Vel.	Calculates diffusion	87.193	78.008
		velocity		
6	Cond. Heat flux	Calculates Conductive	0.408	8.265
		heat flux		

Reduced Chemistry

Performing simulations using full chemistry is very expensive. Researchers have developed different strategies to overcome this problem. Most important among them are tracking the chemistry with one or two tracking variables, reducing the chemistry based on some assumptions, tabulation of the possible chemical states, etc. In this thesis we use a reduced mechanism that will predict the combustion mechanism very well in many different situations. The chemical reaction mechanism that is used in this study is the 10-step reduced reaction mechanism [14] of methane, which represents the combustion using ten reactions among fourteen species. It has been reduced from a skeletal mechanism which itself is derived from GRI-Mech 2.11 [11]. A validation of this mechanism is given at length in the previous chapter on laminar flames.

Reactions steps are:

$$2H + 2CH_2O \rightleftharpoons O_2 + 2CH_3 \qquad (RI)$$

$$2H + CH_2O \rightleftharpoons OH + CH_3 \qquad (RII)$$

$$H_2 + CH_2O \rightleftharpoons OH + CH_3 \qquad (RIII)$$

$$H + H_2O + CH_2O \rightleftharpoons 2OH + CH_3 \qquad (RIV)$$

$$H + 2CH_2O \rightleftharpoons H_2O + CH_3 + CO \qquad (RV)$$

$$H + CH_4 + CH_2O \rightleftharpoons OH + 2CH_3 \qquad (RVI)$$

$$H + CO + CH_2O \rightleftharpoons CH_3 + CO_2 \qquad (RVII)$$

$$H + H_2O + C_2H_2 \rightleftharpoons H_2 + CH_3 + CO \qquad (RVIII)$$

$$CH_2O + C_2H_4 \rightleftharpoons 2CH_3 + CO \qquad (RIX)$$

$$CH_2O + C_2H_6 \rightleftharpoons OH + CH_3 + C_2H_4 \qquad (RX)$$

After applying the simplifications mentioned in the previous section for molecular properties, maximum CPU time is required in evaluating the reaction rate of the species (See Table 2.3). The reaction rates of the species for 10-step is evaluated by

a CHEMKIN subroutine CKWYP. Each time this subroutine is called it performs iterations to find the mass fractions of steady-state species in the skeletal mechanism, which contains more than 20 species with 150 reactions. This makes the CKWYP subroutine expensive and evaluating reaction rates at every grid point and at each time step will be unnecessarily expensive, especially when the state of the mixture does not change very much. In this study of non-premixed flames, we have air on one side and the fuel on the other side with constant mixture composition, where the temperature does not vary very much. At these locations if we do not compute the reaction rate for every iteration, it can save a huge of computational time. We choose a criteria to calculate the reaction rate in the fuel stream and oxidizer stream only when the temperature is more than 500K. Reaction rates are evaluated on the whole domain only once in every 50 iterations.

2.4 Simulations

In modeling non-premixed and partially-premixed turbulent combustion, it is often assumed that the flame exists as a thin laminar sheet its inner structure is not affected by the turbulence. Such a laminar flame termed as 'flamelet' is stretched and strained by the turbulent field. Study of such assumption along with the general behavior of the flame in turbulent fields is important to the understanding of combustion phenomena. Flame itself will also affect the turbulence in several other ways. Heat release from the flame will cause a volumetric expansion, which will smooth out the vorticity field. It also increases the viscosity, which is dependent on the temperature, and thus reduces the local Reynolds number. The reduced local Reynolds number increases the dissipation of turbulent kinetic energy. In this section the results obtained from the direct numerical simulations of 2D-turbulence interacting with initially laminar flame will be presented. Different statistics are studied which help the understanding of combustion in turbulent flows.

2.4.1 Initialization

The one-dimensional flame obtained from the low-strain laminar opposed-jet simulations is projected into two-dimensions (see Figure 2.2) and is used for initialization of scalar (temperature and mass fraction) fields. A two-dimensional well developed and well resolved isotropic decaying turbulence is then imposed on this flame at the initial time. The resulting turbulent non-premixed/partially-premixed flame will be allowed to develop according to the governing equations. Simulations were performed long enough to remove slight "inconsistency" between the initial turbulence and flame.

Initial turbulence field was generated using integration of the non-dimensional governing equations via the Fourier pseudo-spectral method with periodic boundary conditions. Explicit second-order Adams-Bashforth scheme is used to advance in

time. A random solenoidal, 2D field with zero mean and Gaussian spectral density function is used for initialization of the velocity field [22],

$$E(k) = Ck^4 \exp\left[-2\left(\frac{k}{k_o}\right)^2\right] \tag{2.41}$$

where C is calculated based on initial turbulent kinetic energy and k_o is the wave number at peak in energy spectrum. In our simulations the values $k_o = 5$ and C = 0.8 were taken. The pressure field is initialized by solving the Poison equation using velocity field. The initial velocity and pressure field are then allowed to decay for sufficiently long time such that the enstrophy spectrum at small scales is well developed. The developed field has the characteristics given in Table 2.5. The definitions of the parameters in Table 2.5 are given in Eqs. 2.35 - 2.39.

Table 2.5. Characteristics of developed turbulence field

	σ_v	Ω	η	l	L	Re_l	Re_L
ı	0.359	8.94	2.75	0.06	0.427	9.71	230.32

The above discussed field is non-dimensional, which has the advantage in providing different turbulent fields of different characteristics when multiplied by appropriate scale factors. This will be helpful in generating the desired dimensional turbulence fields from the same set of turbulence data. In the simulations for this thesis three dimensional turbulence fields with characteristics given in Table 2.6 were used. In the table, u' represents the rms of velocity fluctuations, L and l represent the integral and microscale length scales, Re_L and Re_l are the Reynolds numbers based on L and l, respectively and τ_l is the eddy turn-over time. Eddy turn-over time is defined as the time that a fluid particle traveling with rms velocity requires to cover the integral length distance. Reference viscosity is calculated based on the air viscosity at initial temperature (294 K), which is the minimum viscosity in the domain. Length of the domain is 5 centimeters in either direction.

Table 2.6. Dimensional characteristics of turbulence fields

Case	u'	L	l	Re_L	Re_l	$ au_t$
	(cm/s)	(cm)	(cm)			(sec)
I	6000	0.34	0.048	12622	1781	5.66e-5
II	4800	0.34	0.048	10102	1426	7.07e-5
III	3000	0.34	0.048	6311	891	1.13e-4

Very low strain flames produced by three different partial premixing of fuel are used in these simulations. Partial premixing of 0% (pure diffusion flame), 25%, and 75% air in fuel stream are considered. Some of the parameters for these flames and the simulations performed in this thesis are given in Table 2.7. In the table, δ represents the flame thickness and L is the integral length scale of turbulent flow field. The flame thickness can be defined in many ways based on the gradient of mixture fraction, the zone temperature and the species production rate. We chose the flame thickness to be the width of zone whose end-point temperature is 500 K.

Table 2.7. Simulation cases studied

No.	Premixing (%)	δ (cm)	δ/L	Turbulence cases
1	0	0.693	2.04	I
2	25	0.94	2.76	I
3	75	0.82	2.41	I, II, III

All of our turbulent flame simulations were performed on Sun 4 processors workstation with parallelized code. Extended MacCormack scheme is used to time march the variables. Results in the form of contours, statistics and images are presented in the next section. Images in this thesis are presented in color.

2.4.2 Results

DNS results for the cases described in the previous section will be discussed here. Analysis of the data will be performed after at least one eddy turn-over time so as to give the flame sufficient time to adjust itself to the turbulence. We will aim to study the effects of turbulence on the inner structure of initially laminar non-premixed and partially-premixed flames and thus the validation of the use of laminar flamelet models (libraries) in turbulence modeling. These effects can be studied through various means as explained in reference [55]. First the effects on the general structure in physical space is studied through contour plots and y-averaged (y is the homogenous direction) statistics of different variables. Analysis is performed normal to the surface of the stoichiometric line at the flame zone for both burning and locally quenched flame, and profiles of various variables in this (flamelet) direction are compared to the corresponding laminar profiles. Turbulence effects on the flame inner structure can also be studied via the scatter plots of the desired variable in the mixture fraction space (defined in the previous chapter).

Flame Structures

Contour plots of temperature, mixture fraction, and *OH* & *CO* mass fractions at four different times are shown in Figures 2.3-2.6 for 75% partially premixed flame interacting with turbulence of case I. As the time progresses the flame is wrinkled, distorted and stretched. The turbulence field imposes a highly varying strain at some regions of the flame making the local tangential stretch so high that the flame will extinguish locally. Structures similar to edge flames can be observed on either side of the extinction region [5]. Later in time, pockets of burning flame regions can be seen, which are separated by the quenched flame regions. This can be clearly seen in *OH* mass fractions contours in Figure 2.5. The maximum temperature location in Figure 2.3, which approximately represents the flame sheet, follows exactly the stoichiometric mixture fraction line of Figure 2.4. It has been argued that *OH* radical

tracks the flame-front more precisely [1, 46]. Figure 2.5 shows the contours of mass fractions for OH. It can be seen from the contours that the OH profile is close to the stoichiometric mixture fraction location as long as the flame exists. In Figure 2.6 contours of CO mass fraction are plotted, which show similar trends to others profiles.

Temperature and the *OH* mass fraction averaged in y-direction are plotted in Figure 2.7 at four different eddy turn-over times. It is observed that the averaged values of both the temperature and *OH* widens in x-direction and the peak values drops with time. As the results in Figures 2.3-2.6 suggests, the widening of the averaged values due to stretching and wrinkling of the flame. The drop in the peak value is due to the fact that averaging has been performed in periodic direction rather than along the flame. These y-averaged plots cannot be compared with the laminar structures, and the reasonable turbulent counterpart to laminar profiles are the profiles in the direction normal to the flame.

In flamelet models of turbulent non-premixed combustion, it is assumed that a laminar flame is located surrounding the stoichiometric mixture fraction value. It's state (burning or quenched) will depend on the scalar dissipation rate at stoichiometric (χ_{st}). If $\chi_{st} > \chi_q$, then the flame is extinguished, and if $\chi_{st} < \chi_q$ it is assumed to be burning, where χ_q is the quenching limit of scalar dissipation rate. Normal to the stoichiometric mixture fraction line the flame structure will be laminar-like. Profiles for different variables in the mixture fraction space are extracted at various locations and compared with the laminar profiles. The data obtained for 75% partially-premixed methane flame and turbulence case I are used for this analysis.

Figure 2.8(a) shows the contours of mixture fraction and the location where a section of the flame is taken for analysis. Figures 2.8(b) and 2.8(c) show the temperature and the strain rate versus mixture fraction in this section. The temperature plot in mixture fraction space is identical with the low strain laminar temperature

profile. This is because the section considered in Figure 2.8 is in a low strain region of the flow that is characterized with a fully burning flame. This region can be seen to sustain a complete combustion at later times (see Figure 2.5(d)). Figure 2.9 shows similar plots for a section of the flame where the reaction will eventually extinguish at long time. The strain rate plot Figure 2.9(c) shows that at this section the strain rate is much higher than that was in earlier case. Consequently, the maximum temperature is less than 1900 K and the temperature profile in the mixture fraction domain is much different from the initial laminar profile. Figure 2.10 shows similar plots for a quenched flame region. The strain rate is high for the flame at this location and flame is quenched with maximum temperature near 900 K.

Scatter Plots

Scatter plots of temperature, mass fractions and other important flame quantities in mixture fraction space show in one plot the various flame-turbulence states existing in the entire domain. Usually, the temperature peaks near the stoichiometric mixture fraction value for a burning flamelet and follow the laminar profiles depending on the value of tangential strain rate (or scalar dissipation rate) at that location. At a location where the tangential strain is more than the quenching limit, the flame should normally extinguish and the maximum temperature will be lower than the laminar values. Scalar mixture fraction dissipation represents the extent of turbulent mixing. For low levels of strain or scalar dissipation rate, the reaction rate is limited by the mixing. When the scalar dissipation rate is increased, the reaction rates increase. At high scalar dissipation rates the heat is transported away from the reaction zone with a rate faster than the rate it is produced by the chemical reactions. This effectively cools down the flame and in a sustained high strain field will result in low temperature and flame extinction.

Figures 2.11-2.13 show the scatter plots for various variables in the mixture

fraction space for three different types of flames. These flames are produced by 0% air in fuel stream (pure diffusion flame, flame no. 1), 25% air in fuel stream (flame No. 2), and 75% air in fuel stream (flame no. 3) and they all are affected by turbulence case I and are plotted at one eddy turn-over time. Initial laminar profiles (shown as dashed lines) are also plotted in these plots for comparison. For all the three flames, the variables show significant scattering even at shorter times. This scatter is due to the enhanced turbulent mixing because of varying strain field of turbulence, and departure from the flamelet behavior. For laminar flames, as the strain rate is increased, the flame temperature decreases (see chapter 2). The temperature values much lower than the initial laminar values can be attributed to the strong strain or extinction. The over-prediction of radicals like OH, H, and CO as observed here are also seen in earlier studies. Experimental data of Barlow et al [3] and three-dimensional direct numerical simulations of Mahalingam et al [32] show similar scatter for the radicals. For OH a simple step change in the scalar dissipation rate for laminar calculations also showed similar over-prediction [2]. This over-prediction can be attributed to the unsteady strain rate that exists in the turbulence field. The behavior of CO in turbulent flame is different on different side of stoichiometric line as the turbulence mixing enhances its production on the oxidizer side and increases its consumption on the fuel side. Scatter plots for 25% premixing and 75% premixing flame also show similar trends.

Next three Figures 2.14-2.16 show the scatter plots of temperature, *OH* mass fraction, and *CO* mass fraction for the 75% partially premixed flame interacting with turbulence of case I at three different eddy turn-over times. As the time advances the scattering increases due to the local flame extinction. At two eddy turn-over times the flame has extinguished at many places and has been cooled down to temperatures as low as 600 K. The extinguished flamelet will be convected and carried in the flow until the scalar dissipation rate is low enough for it to re-ignite. Sometimes, even though the scalar dissipation rate becomes low, the flamelet will not re-ignite due to the lack of radical species or source of energy. This shows that the re-ignition of

the quenched flamelet depends on many parameters of the flow and chemistry and its modeling/prediction is very complicated. The CO and OH mass fraction scatter plots show similar trends in time. Extinction is marked with increased scatter at stoichiometric value of mixture fraction. The scatter plots are also similar for the flames with other premixing levels of fuel stream provided that the turbulence field remain similar. At lower turbulence intensity levels (turbulent cases II and III) the amount of scatter and flame extinction are less significant as expected.

Turbulence Statistics

Figures 2.17-2.18 show the vorticity, the enstrophy, and the turbulent kinetic energy images for case I and flame No.3. Four subplots in each figure show the images at four different eddy turn-over times. Vorticity images show an isotropic turbulence field with no preferred directional dependency at the initial time. However, as the simulation progresses, the vorticity field is affected by the flame and exhibits peaks near the flame regions. Vorticity will be affected mainly by three mechanisms in reacting flows: (1) due to heat released from the chemical reactions volumetric expansion occurs, which smoothes out the vorticity field, (2) the temperature dependence of viscosity results in higher viscosity near to the flame (this local high viscosity will dissipate the vorticity near the flame), (3) the generation of vorticity due to the baroclinic term and misalignment of the pressure and density gradients. The latest effect is clearly shown in Figures 2.17 and 2.18 where it is observed that there is significant increase in vorticity and enstrophy close to the flame. The volumetric-averaged values of the enstrophy (not shown here) shows an early decay and a sudden increase at later times. The decay is due to viscous dissipation which is more significant in exothermic reacting systems, whereas, the increase is due to baroclinic generation. There is in fact a two-way coupling between flame and turbulence. Vorticity is generated because of the baroclinic effect, which causes the increase in strain rate at the flame location (see Figure 2.20). The increased strain rate will then cause the flame to extinguish as discussed previously.

To better understand the flame effect on turbulence, the y-averaged statistics (denoted by subscript avg) of various turbulent/flame variables are computed. The y-direction is the homogenous (periodic) direction. Figure 2.21 shows the y-averaged vorticity as a function of normalized x direction. After one eddy turn-over time $(t/\tau_t = 1.0)$, it can be seen that the vorticity field is decayed due to the flame. Heat release and viscous dissipation effects are important up to this time as explained in the previous paragraph. At later times $(t/\tau_t = 1.5 \text{ and } t/\tau_t = 2.0)$, there is an increase in the magnitude (in the negative direction) near the flame. This can be observed more clearly in the y-averaged enstrophy plots, which are shown in Figure 2.22. There is a slight decrease near the flame region at $t/\tau_t = 1.0$ and at $t/\tau_t = 1.5$, 2.0 there is a significant increase in the magnitude of enstrophy.

Figures 2.23-2.25 show the vorticity, enstrophy, and turbulent kinetic energy contours at t=0 and $t/\tau_t=1.0$ for various fuel partial premixing levels with air. There is little difference between different fuel premixing results except that the magnitude is larger for 75% case. The trend being same for all the variables. The y-averaged plots (Figures 2.26 and 2.27) also show only small differences near the flame region. These differences can be attributed to the premixing level of fuel stream with air or the flame thickness, which are different in flames with different partial premixing (see Table 2.6).

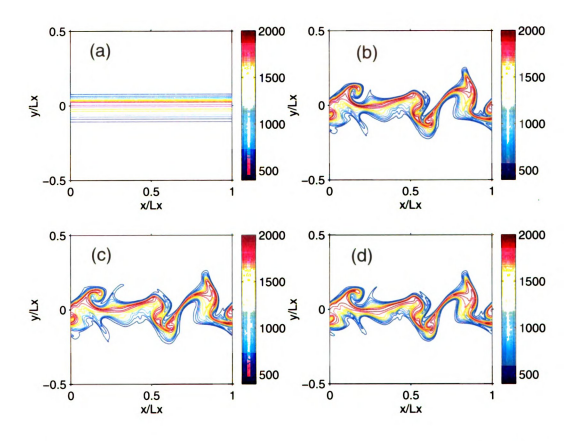


Figure 2.3. Sequence of temperature contours for turbulence case I and flame No. 3 with time; (a) $t/\tau_t=0.0$, (b) $t/\tau_t=1.0$, (c) $t/\tau_t=1.5$, (d) $t/\tau_t=2.0$.

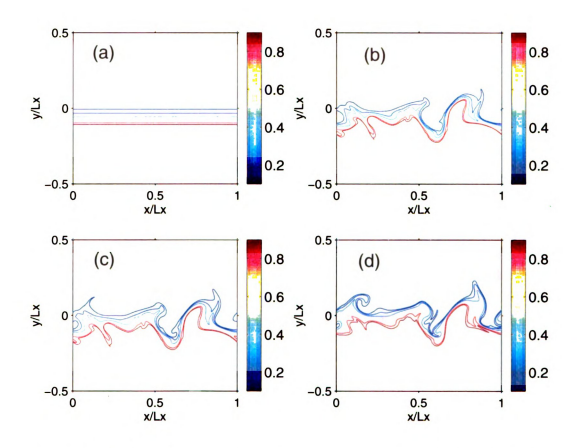


Figure 2.4. Mixture Fraction contours for turbulence case I and flame No. 3 with time: (a) $t/\tau_t=0.0$ (b) $t/\tau_t=1.0$ (c) $t/\tau_t=1.5$ (d) $t/\tau_t=2.0$

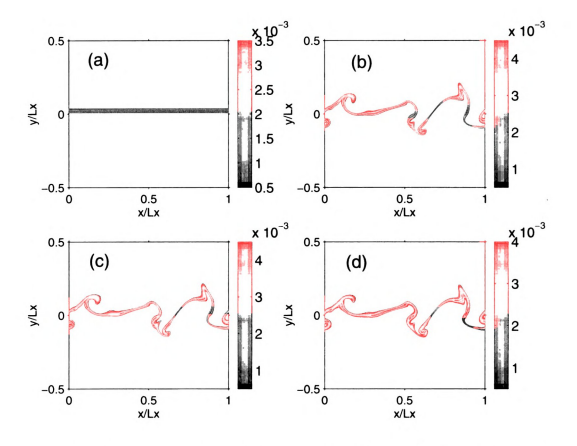


Figure 2.5. Y_{OH} contours for turbulence case I and flame No. 3 with time: (a) $t/\tau_l=0.0$ (b) $t/\tau_l=1.0$ (c) $t/\tau_l=1.5$ (d) $t/\tau_l=2.0$

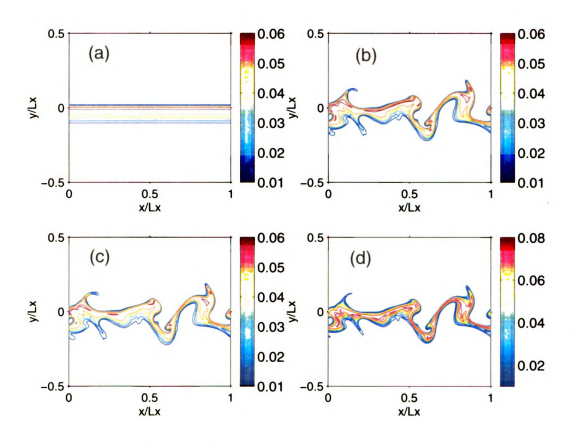


Figure 2.6. Y_{CO} contours for turbulence case I and flame No. 3 with time: (a) $t/\tau_t=0.0$ (b) $t/\tau_t=1.0$ (c) $t/\tau_t=1.5$ (d) $t/\tau_t=2.0$

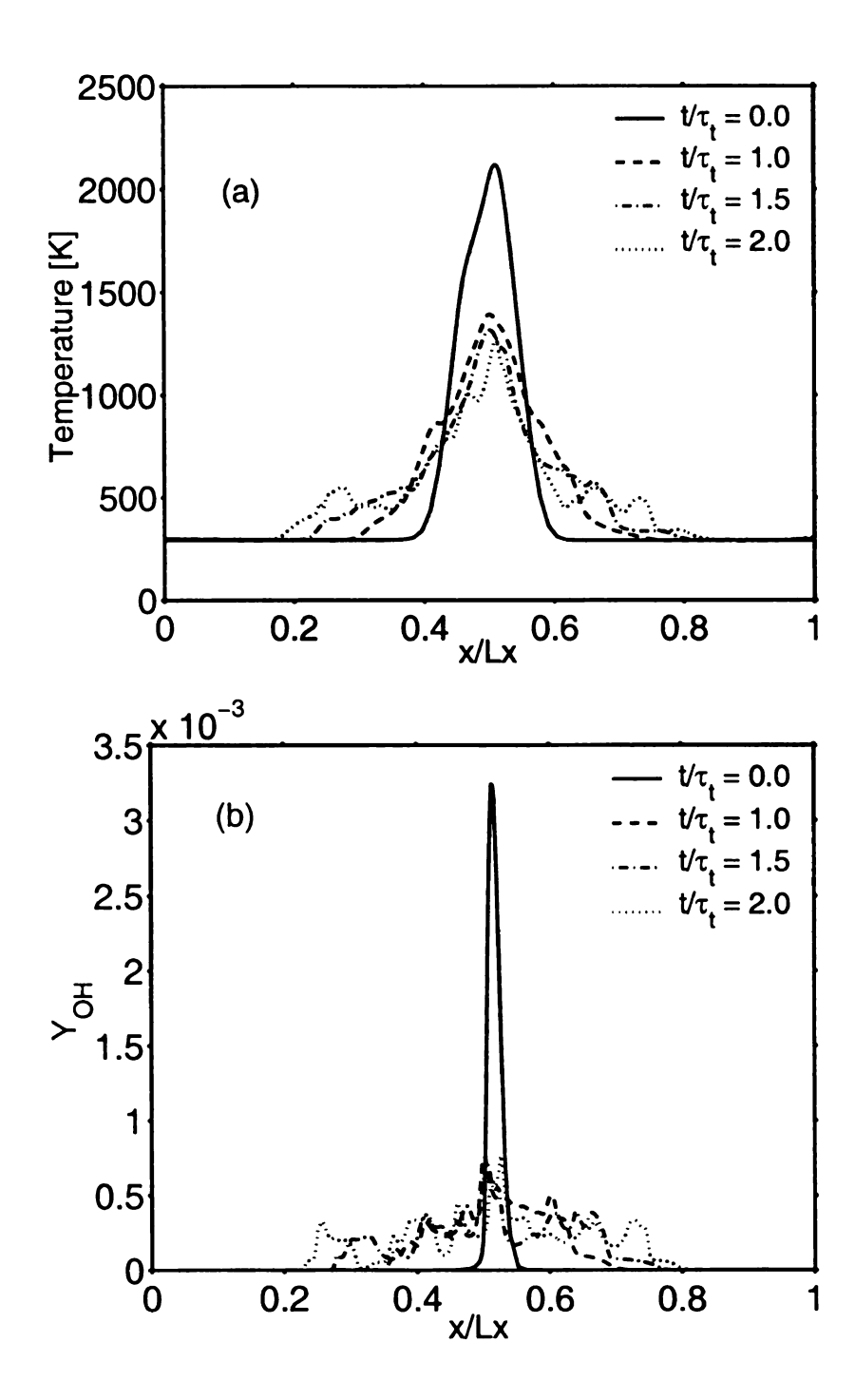


Figure 2.7. Y-averaged plots at different times for (a) Temperature and (b) Y_{OH}

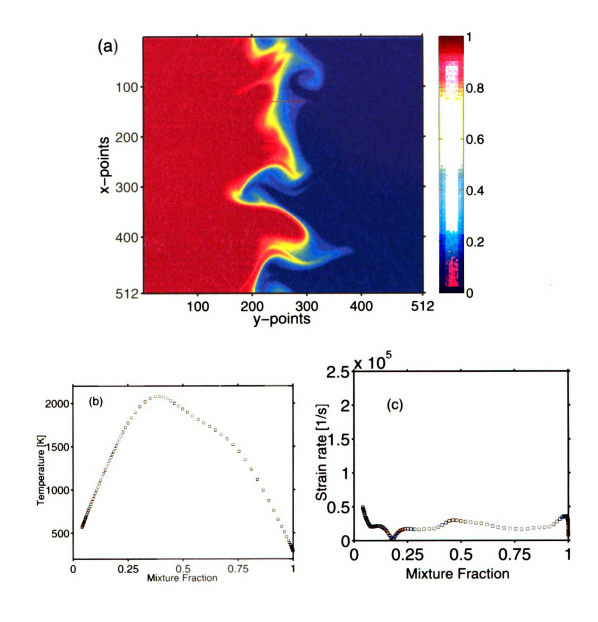


Figure 2.8. Flame normal analysis at a burning region of the flame (a) Mixture fraction contours showing the line of section (b) Temperature (c) Strain rate

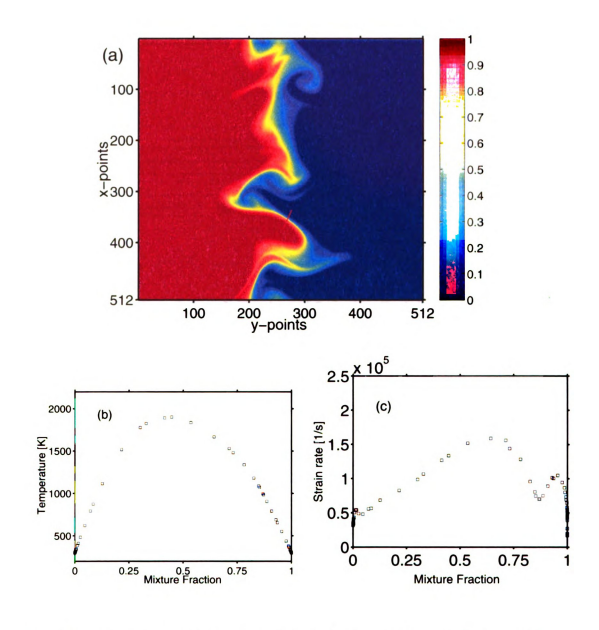


Figure 2.9. Flame normal analysis at a about-to-be-quenched region of flame and for $t/\tau_l = 1.0$ (a) Mixture fraction contours showing the line of section (b) Temperature (c) Strain rate

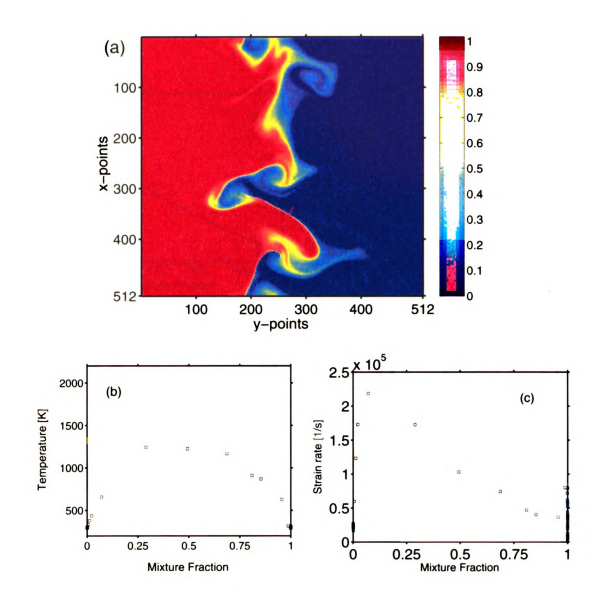


Figure 2.10. Flame normal analysis at a quenched region of flame and for $t/\tau_t=1.5$ (a) Mixture fraction contours showing the line of section (b) Temperature (c) Strain rate

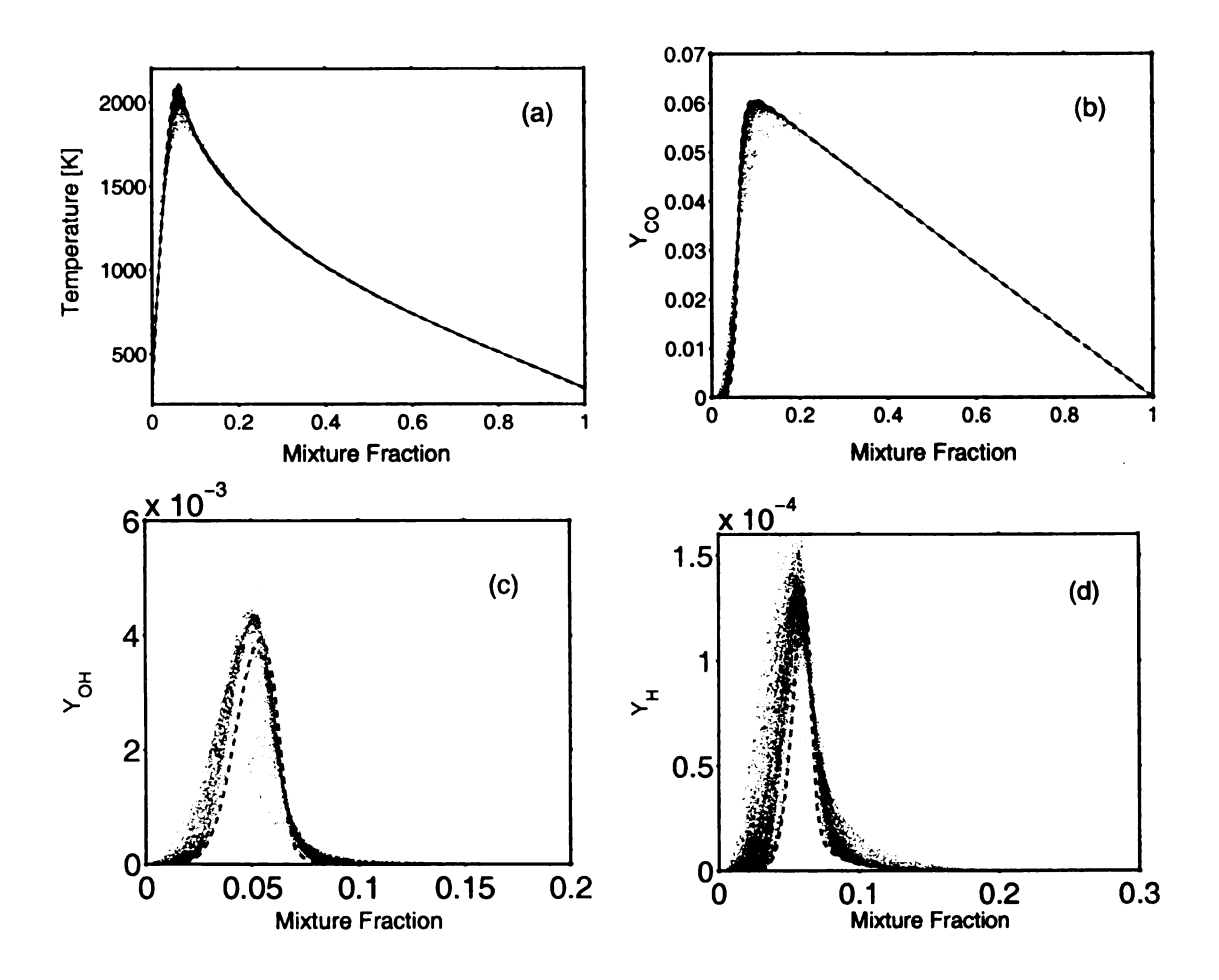


Figure 2.11. Scatter plots in mixture fraction space for turbulence case I and flame No. 1 at one eddy turn-over time. (a) Temperature (b) Y_{CO} (c) Y_{OH} (d) Y_{H} . Dashed lines shows the initial laminar profile

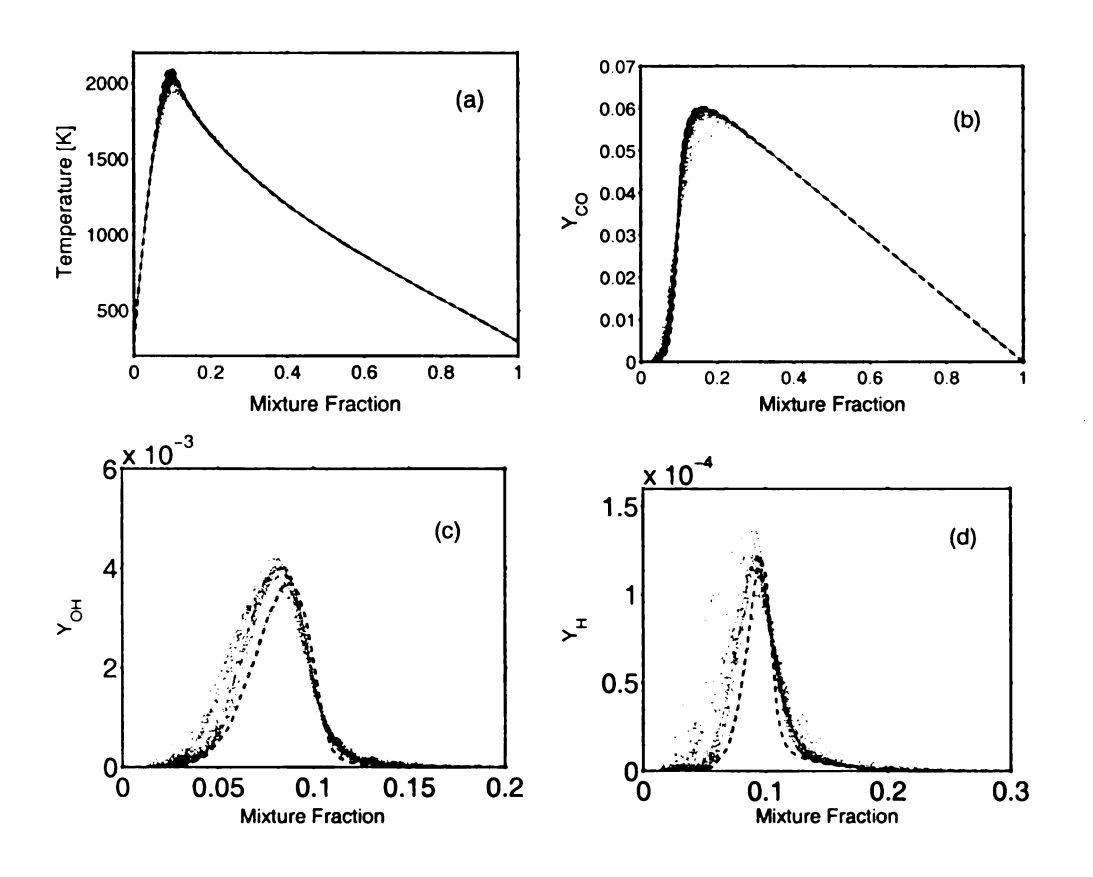


Figure 2.12. Scatter plots in mixture space for turbulence case I and flame No. 2 at one eddy turn-over time. (a) Temperature (b) Y_{CO} (c) Y_{OH} (d) Y_H . Dashed lines shows the initial laminar profile

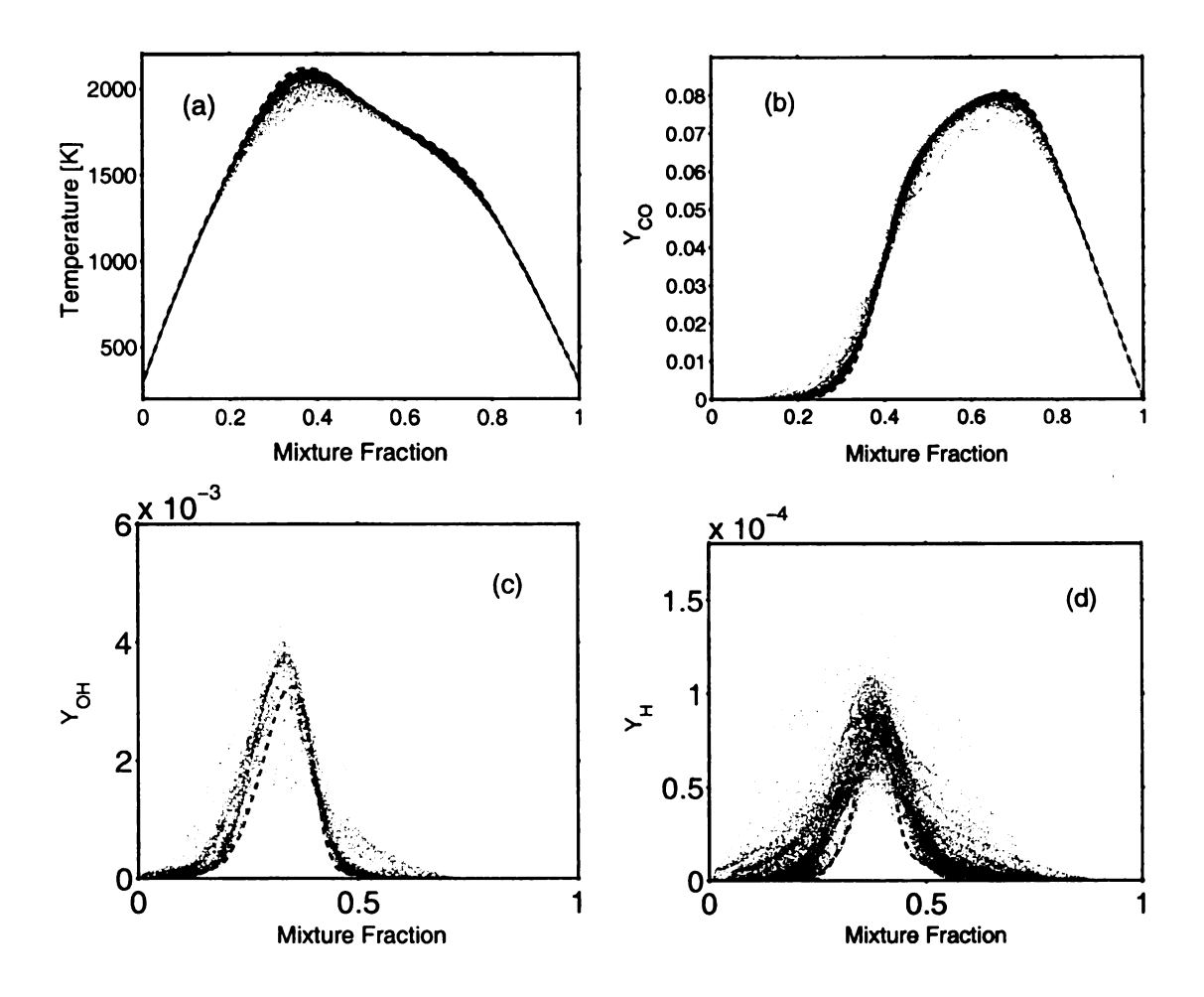


Figure 2.13. Scatter plots in mixture fraction space for turbulence case I and flame No. 3 at one eddy turn-over time. (a) Temperature (b) Y_{CO} (c) Y_{OH} (d) Y_{H} . Dashed lines shows the initial laminar profile

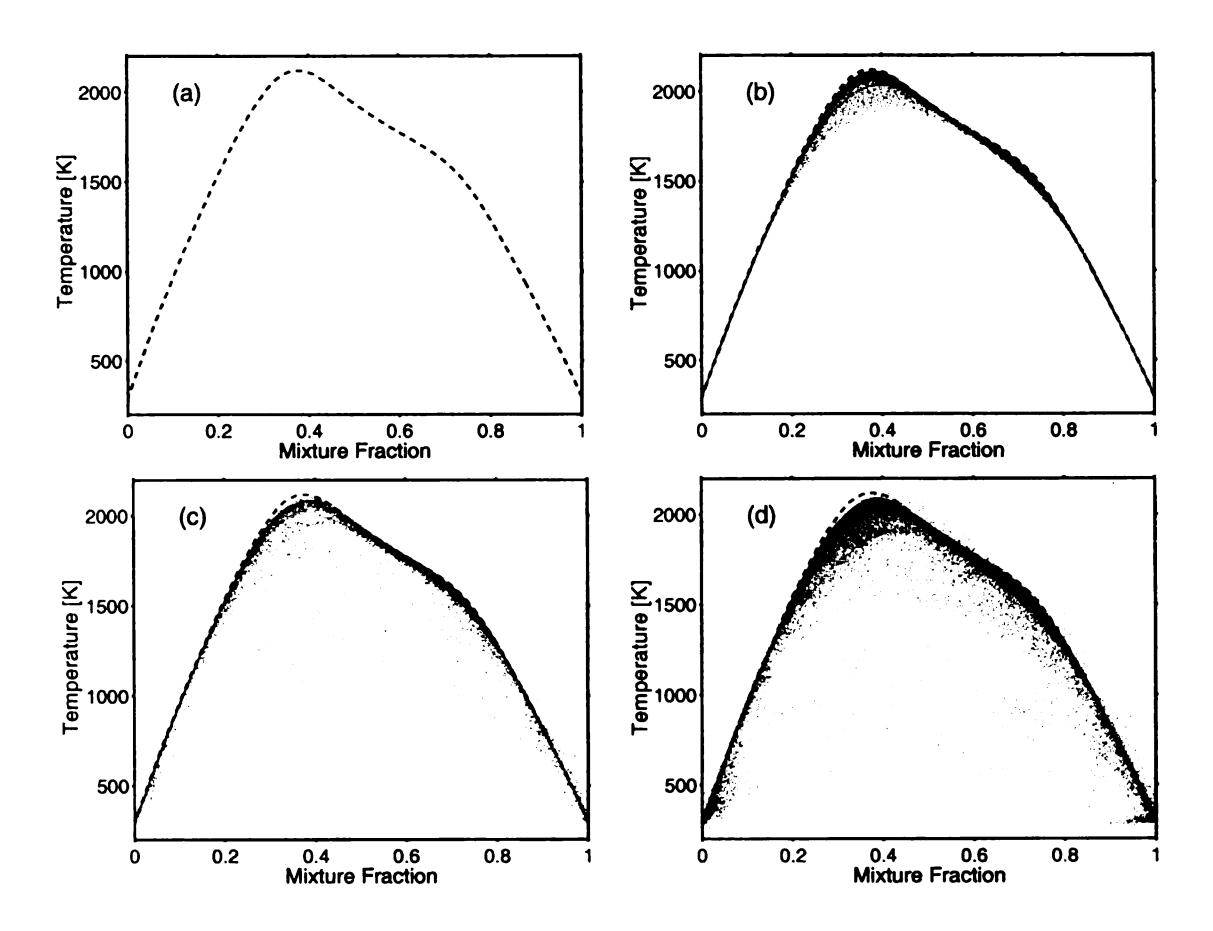


Figure 2.14. Temperature scatter plots for turbulence case I and flame No. 3 for (a) $t/\tau_t = 0.0$ (b) $t/\tau_t = 1.0$ (c) $t/\tau_t = 1.5$ (d) $t/\tau_t = 2.0$ in mixture fraction space. Dashed line shows the initial laminar profile.

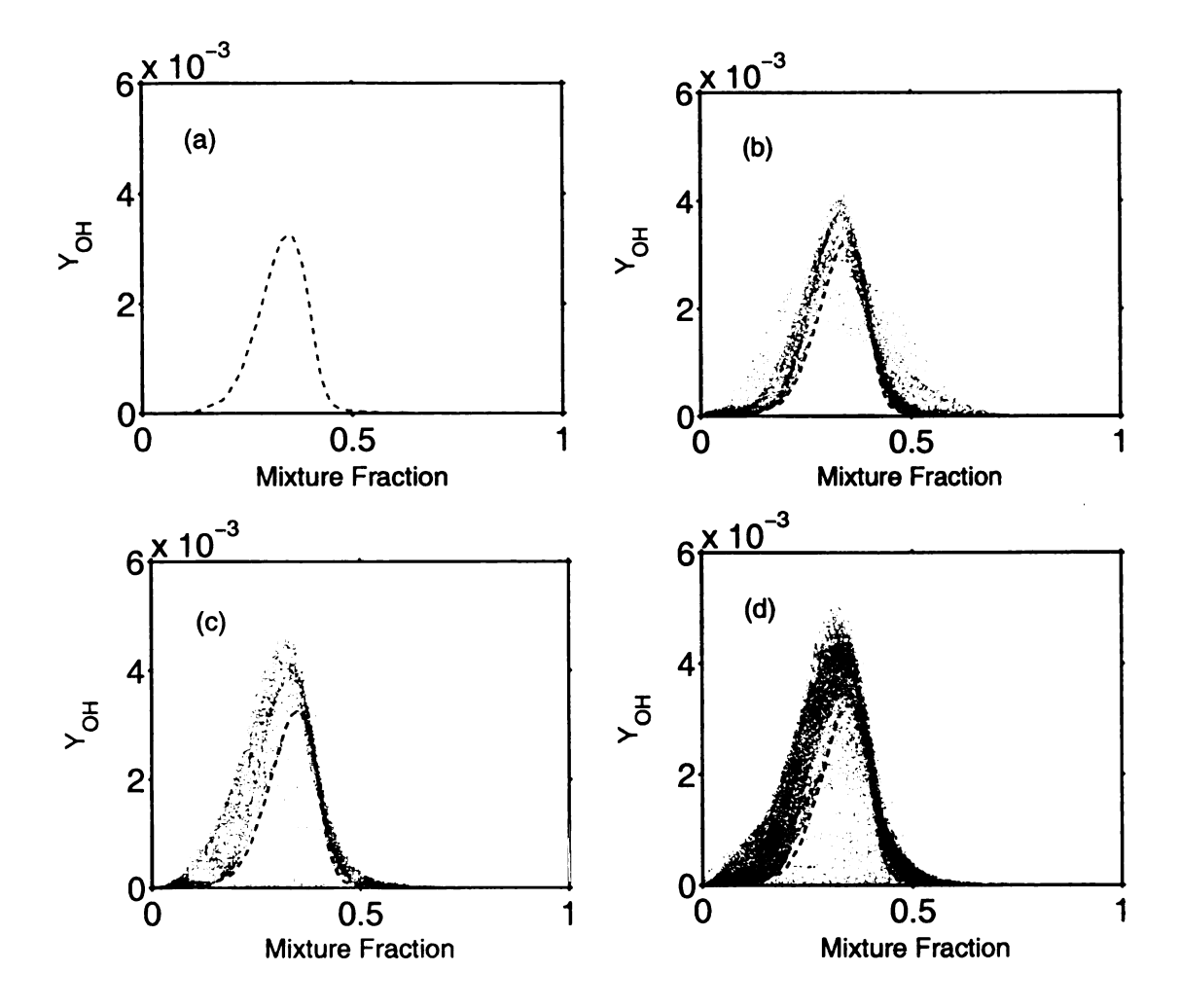


Figure 2.15. Y_{OH} scatter plots for turbulence case I and flame No. 3 for, (a) $t/\tau_t = 0.0$, (b) $t/\tau_t = 1.0$, (c) $t/\tau_t = 1.5$, (d) $t/\tau_t = 2.0$ in mixture fraction space. Dashed line is the initial laminar profile.

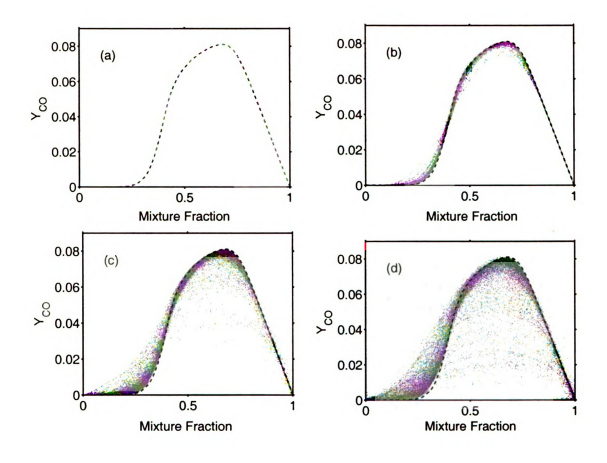


Figure 2.16. Y_{CO} scatter plots for turbulence case I and flame No. 3 for (a) $t/\tau_t=0.0$, (b) $t/\tau_t=1.0$, (c) $t/\tau_t=1.5$, (d) $t/\tau_t=2.0$ in mixture fraction space. Dashed line is the initial laminar profile.

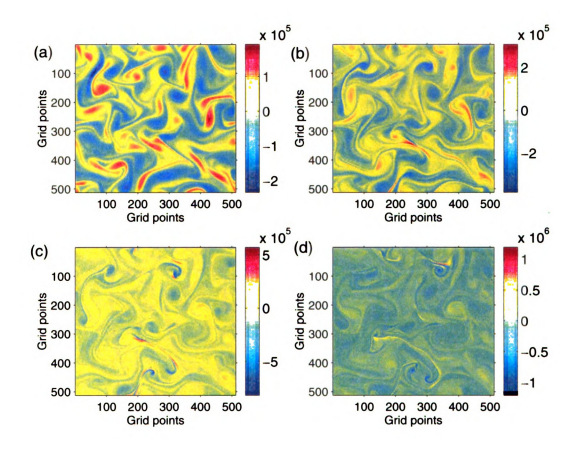


Figure 2.17. Sequence of vorticity images for turbulence case I and flame No. 3 with time: (a) $t/\tau_t = 0.0$, (b) $t/\tau_t = 1.0$, (c) $t/\tau_t = 1.5$, (d) $t/\tau_t = 2.0$.

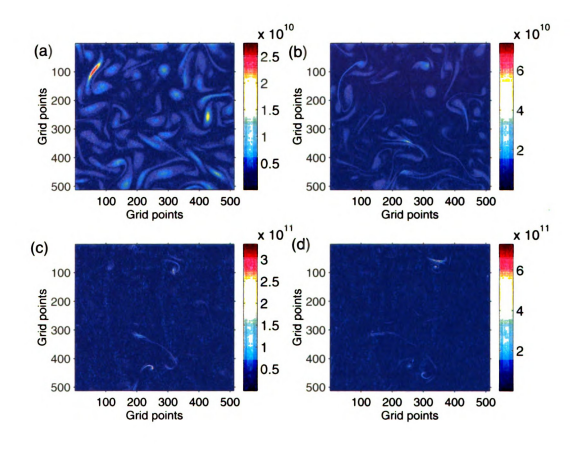


Figure 2.18. Sequence of enstrophy images for turbulence case I and flame No. 3 with time: (a) $t/\tau_t = 0.0$, (b) $t/\tau_t = 1.0$, (c) $t/\tau_t = 1.5$, (d) $t/\tau_t = 2.0$.

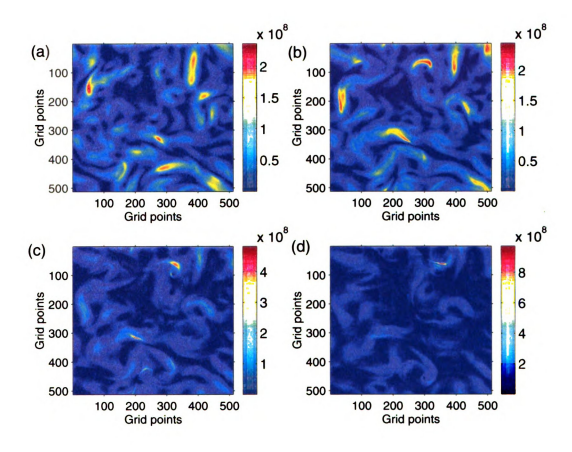


Figure 2.19. Sequence of turbulent kinetic energy images for turbulence case I and flame No. 3 with time: (a) $t/\tau_t=0.0$, (b) $t/\tau_t=1.0$, (c) $t/\tau_t=1.5$, (d) $t/\tau_t=2.0$.

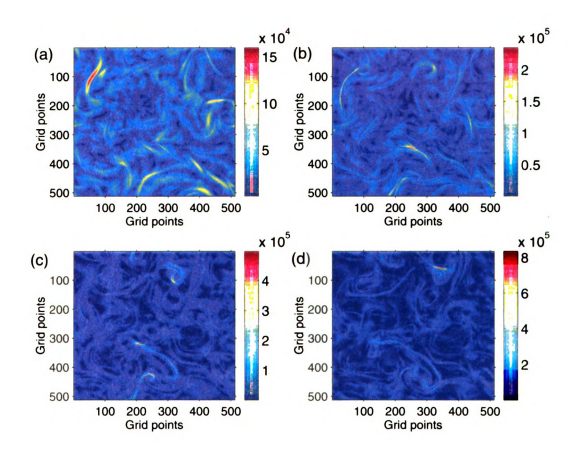


Figure 2.20. Sequence of strain rate images for turbulence case I and flame No. 3 with time: (a) $t/\tau_{\ell}=0.0$, (b) $t/\tau_{\ell}=1.0$, (c) $t/\tau_{\ell}=1.5$, (d) $t/\tau_{\ell}=2.0$.

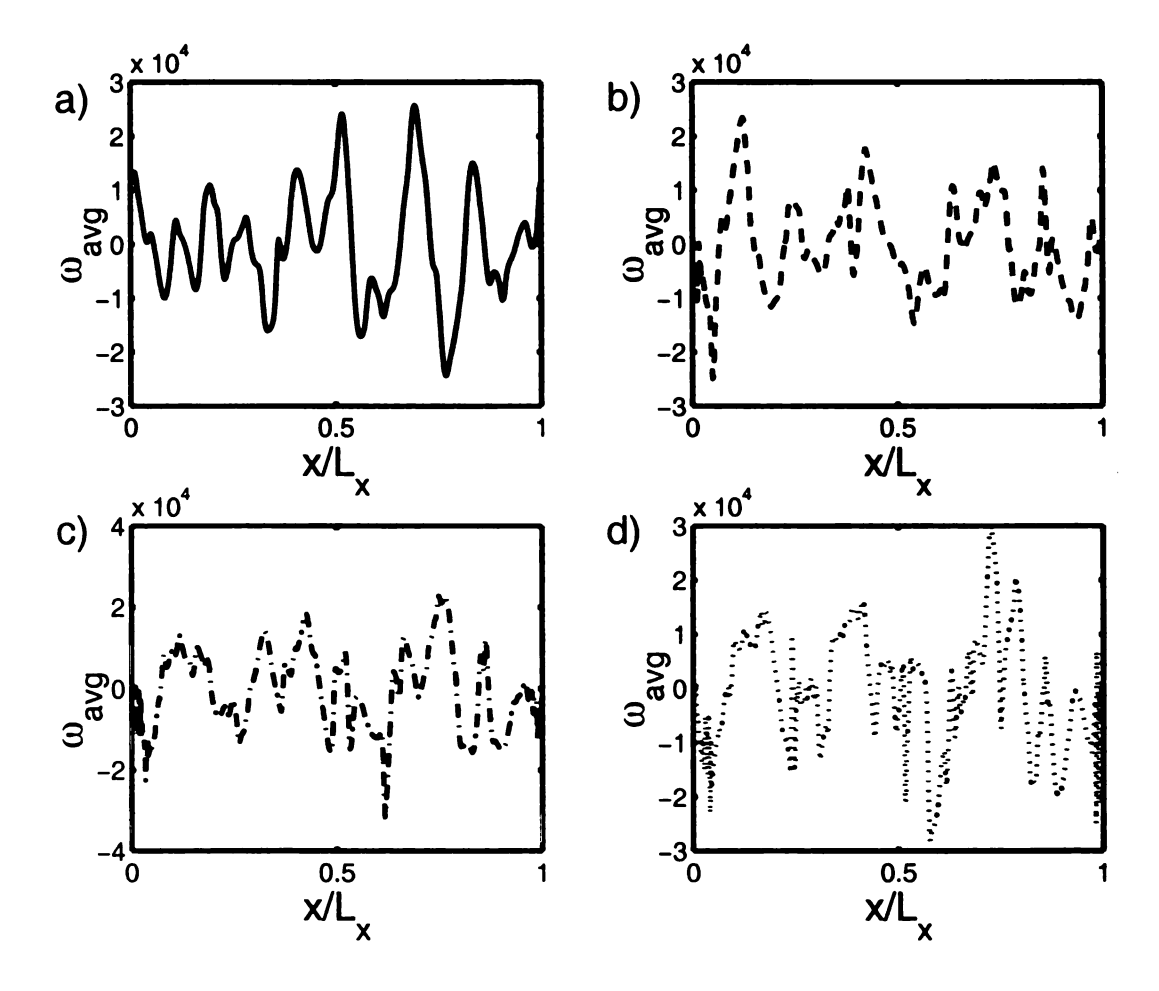


Figure 2.21. Y-averaged vorticity plots at four eddy turn-over times. (a) $t/\tau_t=0$, (b) $t/\tau_t=1.0$, (c) $t/\tau_t=1.5$, and (d) $t/\tau_t=2.0$

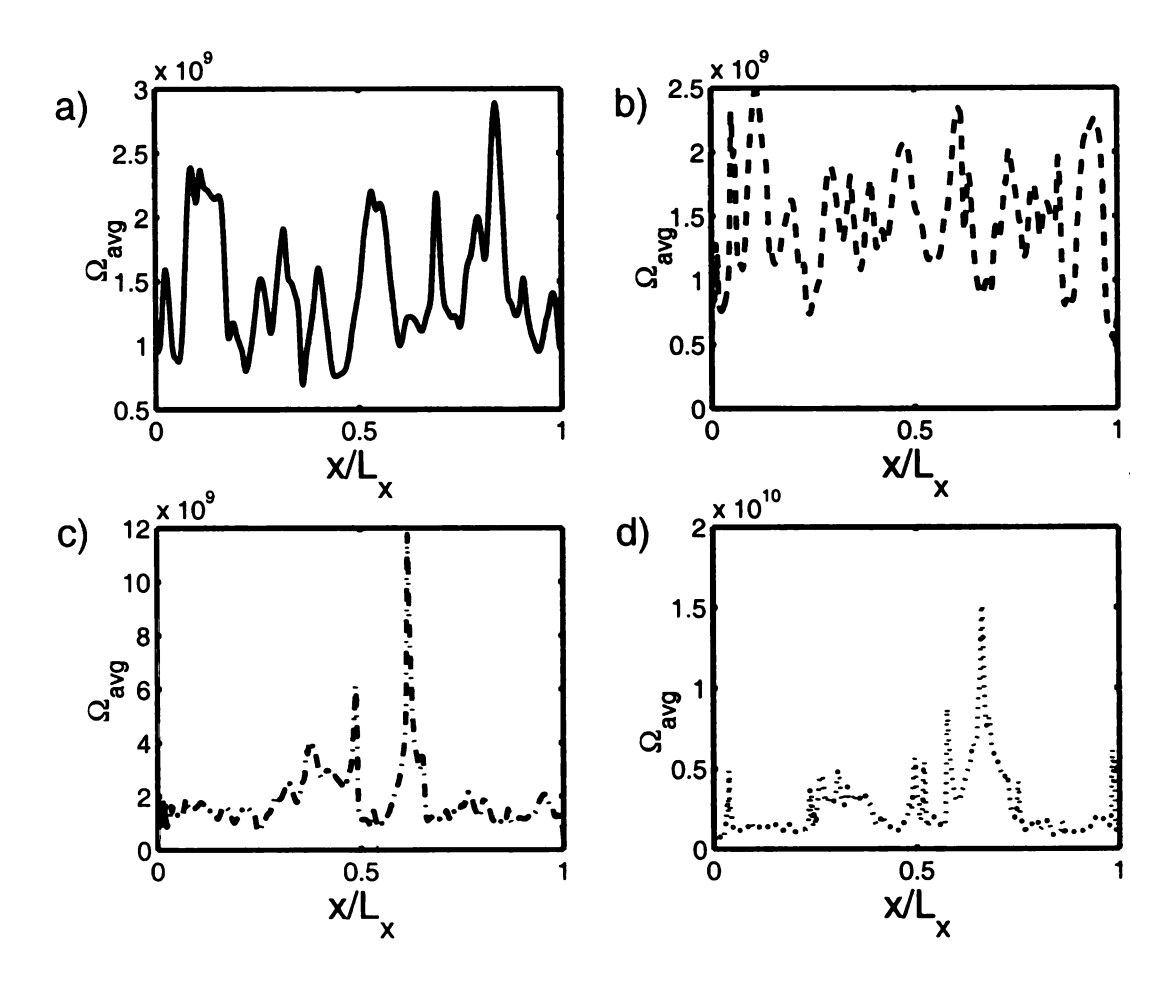


Figure 2.22. Y-averaged enstropy plots at four eddy turn-over times. (a) $t/\tau_t=0$, (b) $t/\tau_t=1.0$, (c) $t/\tau_t=1.5$, and (d) $t/\tau_t=2.0$

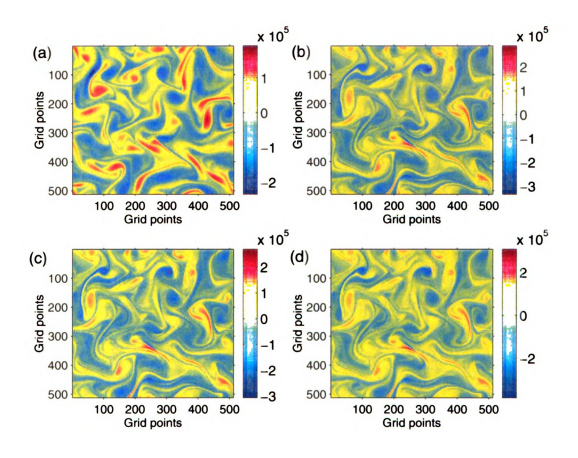


Figure 2.23. Sequence of vorticity images for turbulence case I and flames of various premixing levels. (a) Initial vorticity, (b) A%=0 & $t/\eta=1.0$, (c) A%=25 & $t/\eta=1.0$, (d) A%=75 & $t/\eta=1.0$.

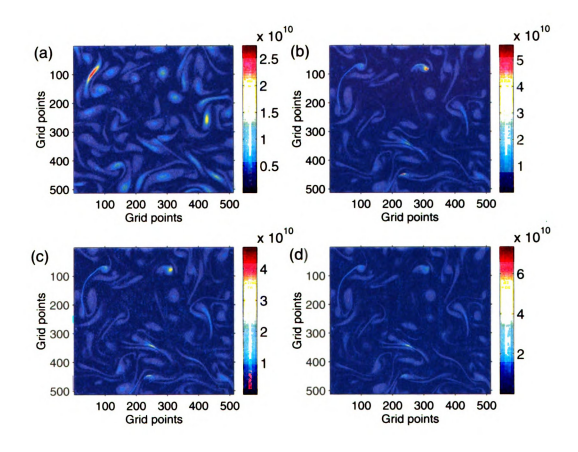


Figure 2.24. Sequence of enstrophy images for turbulence case I and flames of various premixing levels. (a linitial enstrophy, (b) A% = 0 & t/τ_t = 1.0, (c) A% = 25 & t/τ_t = 1.0, (d) A% = 75 & t/τ_t = 1.0.

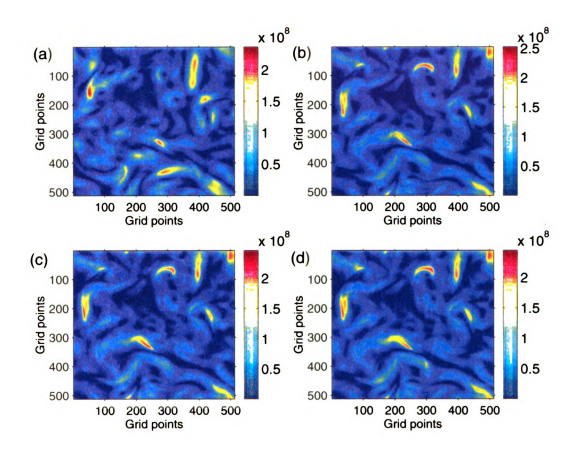
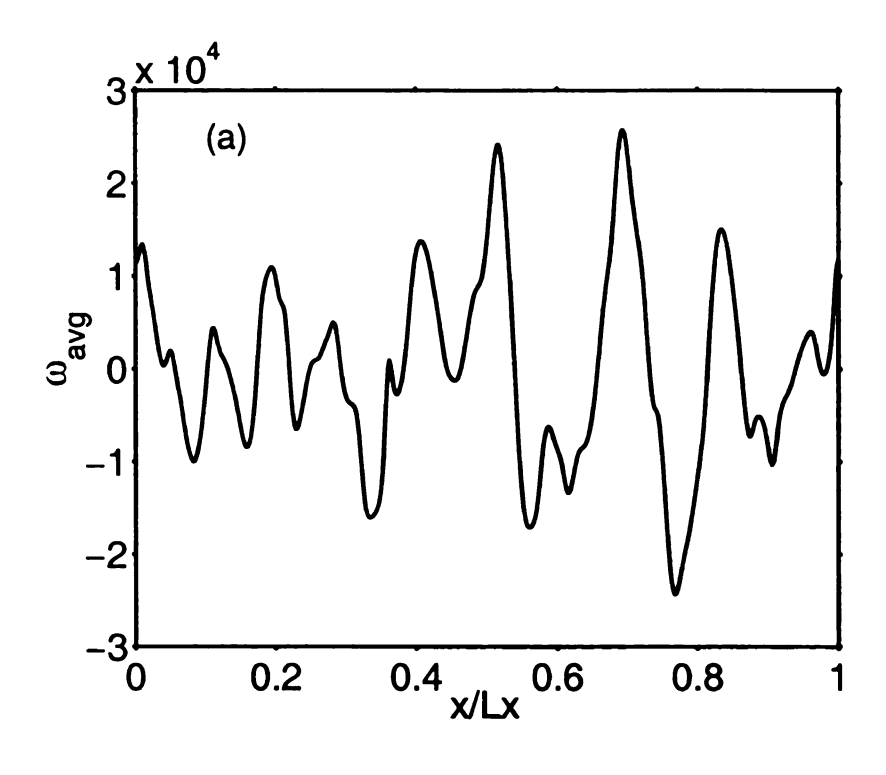


Figure 2.25. Sequence of turbulent kinetic energy images for turbulence case I and flames of various premixing levels. (a) Initial TKE, (b) A%=0 & $t/\eta=1.0$, (c) A%=25 & $t/\eta=1.0$, (d) A%=75 & $t/\eta=1.0$.



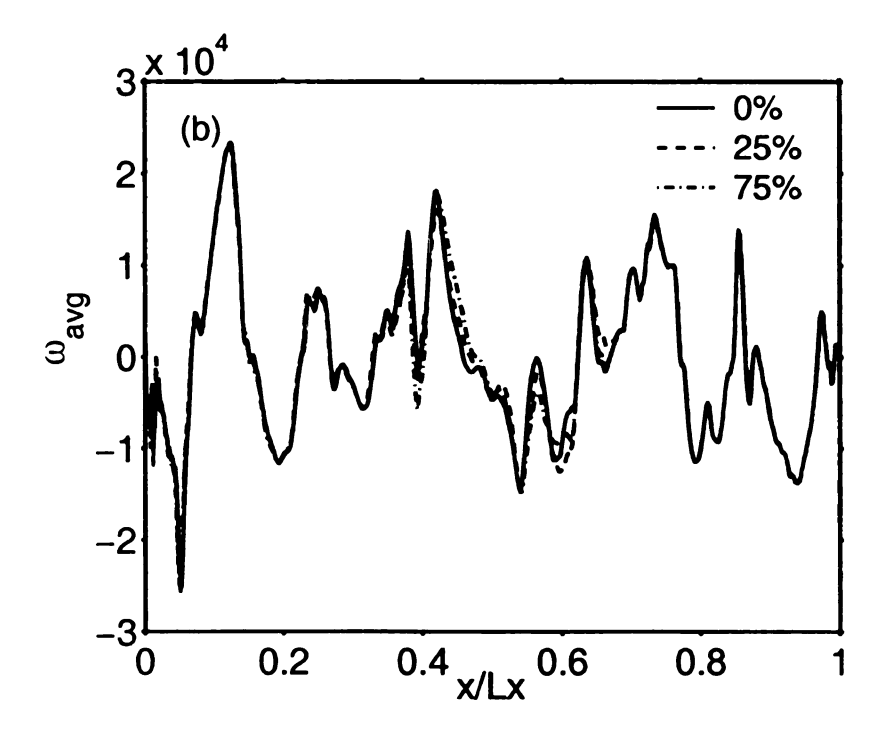


Figure 2.26. Y-averaged vorticity for different partial premixing. (a) Initial profile, and (b) At $t/\tau_t=1.0$.

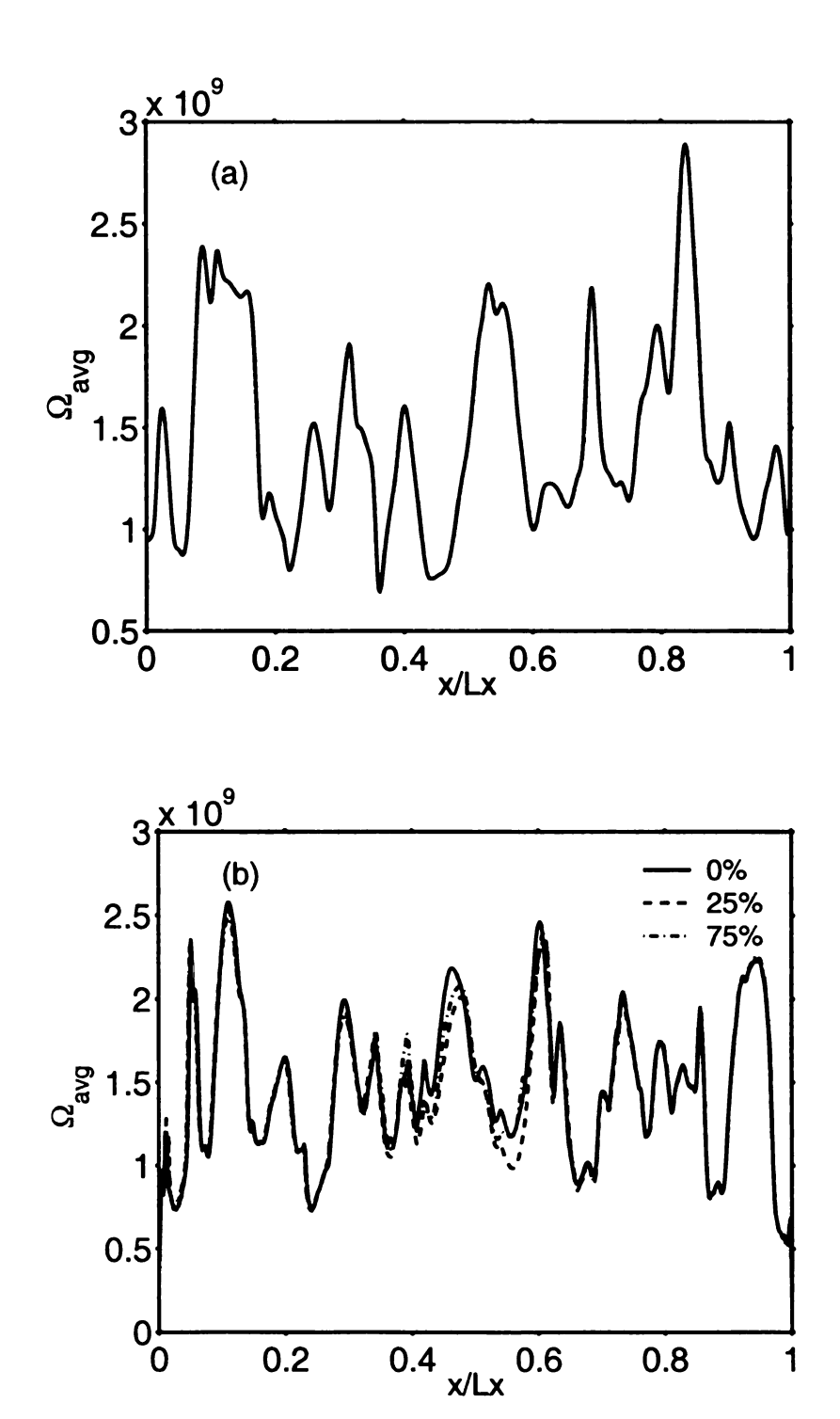


Figure 2.27. Y-averaged enstrophy for different partial premixing. (a)Initial profile, and (b) At $t/\tau_t=1.0.$

0.8

0.6

0.2

CHAPTER 3

Conclusions

Numerical simulations of turbulent combustion involving detailed chemical kinetics mechanisms are computationally very expensive. Even the simplest hydrocarbon fuel, methane needs about 50 species and 300 reactions for a "complete" modeling of its combustion with air. Reduced reaction mechanisms would be a partial remedy for the high computational requirements in such simulations and are usually derived systematically from the original "full" mechanism. These simpler mechanisms should represent the combustion chemistry accurately in all the possible situations of practical importance. In this work, a detailed assessment of methane-air reduced reaction mechanisms is performed in a laminar counterflow flame configuration for various flow/chemistry conditions. The effects of partial premixing of the fuel with air on the compositional and physical structure of the flame are studied via variety of reduced and full reaction mechanisms.

Temperature and species profiles produced by different mechanisms were compared to those obtained by the GRI-Mech 3.0 for wide range of strain rates and partial premixing levels of fuel stream with air. Based on the simulations performed, it was found that the reaction mechanisms that contain reactions involving both the C_1 and C_2 species perform much better than the mechanisms with only C_1 species. Results obtained with 10-step and 12-step mechanisms compare very well with those of the full GRI mechanisms for all values of strain rate, and premixing, and generate the same ignition and extinction characteristics. It is concluded that the 10-step

reaction mechanism with only 14 species and 10 reactions, is a good candidate for modeling of the the chemistry in finite-rate simulations. However, other mechanisms with lesser number of species such as the 4-step, 5-step and 6-step, although perform well in some of the conditions, are not fully accurate. The performance of these reaction mechanisms are found to deteriorate as the strain rate is decreased or the level of fuel premixing with air is increased. Whereas, 4-step mechanism fail to predict the rich premixed flame zone in partially premixed flames, 5-step and 6-step mechanisms predict a premature premixed flame zone. The worst affected species by these improper premixed flame prediction are CO and H_2 species. In fact the trends observed for these species as the strain rate is varied are exactly opposite to what is predicted by all the other mechanisms.

The 10-step mechanism, which was found to be an accurate model in different flow/flame conditions, was used for prediction of ignition temperatures. Prediction of ignition temperature is important in the modeling of quenched flamelet re-ignition process. Our laminar opposed-jet results indicate that the ignition temperatures are increased as the strain rate increase, which is expected. However, the effect that the fuel premixing has on the ignition temperature is not very clear. At low strain rates, the effect is small but at high strain rate the ignition temperature tend to increase as partial premixing decreases.

The 10-step mechanism is also used in a direct numerical simulation (DNS) of isotropic turbulent flow interacting with a diffusion/partially-premixed flame. DNS were conducted to understand the behavior of the flames in realistic flow situations of highly varying unsteady strain field. The effect of the flame on the turbulence field is also studied. Our results show significant changes in the flame structure embedded in a high intensity turbulent field due to the imposed variable strain field and significant flame stretching and distortion. Deviation from the initial (laminar) flame structure in compositional space has been observed accompanied with significant local extinction at the locations where the strain rate was too high for the flame

to be sustained. These effects were reflected in the enhanced scatter in the scatter plots for the temperature and the species mass fractions. At early times, significant vorticity dissipation was observed due to increased viscosity near the flame and due to the volumetric expansion. In the later times, vorticity is seen to be generated by the so called baroglingue term near to the flame.

As the list of reduced reaction mechanism for different fuels are not exhaustive, detailed assessment of available mechanisms including variable diffusivity and radiation models can be performed as a future work. Since it is essential to understand various characteristics of flame-turbulence interactions for combustion modeling, a detailed study with various flame thicknesses, premixing and using different levels of approximations to the transport models can be pursued as an extension to this work. Finally, as the small scale behavior in the two-dimensional turbulence is different from the realistic three-dimensional turbulence, simulations using three-dimensional DNS can be used to understand the flame/turbulence interactions in more realistic flows.

BIBLIOGRAPHY

BIBLIOGRAPHY

- [1] Negin Angoshtari. Direct numerical simulation of premixed turbulent methane flames modeled with various reduced mechanisms. Master's thesis, Michigan State University, 2003.
- [2] R. S. Barlow and J.-Y. Chen. Twenty-Fourth Symposium (International) on Combustion/The Combustion Institute, pages 231–237, 1992.
- [3] R. S. Barlow, R. W. Diblle, S. H. Starner, and R. W. Bilger. Twenty-third Symposium (International) on Combustion/The Combustion Institute, pages 583-589, 1990.
- [4] M. Baum, T. Poinsot, D. Howarth, and N. Darabiha. Direct numerical simulation of $h_2/o_2/n_2$ flames with complex chemistry in two-dimensional turbulent flows. J. Fluid Mech., page 1, 1994.
- [5] B. Bédat, F. N. Egolfopoulos, and T. Poinsot. Direct numerical simulation of heat release and nox formation in turbulent nonpremixed flames. *Combustion and Flame*, 119:69-83, 1999.
- [6] R. W. Bilger. Combust. Flame, 30:277, 1977.
- [7] R. W. Bilger. Twenty-Second Symposium (International) on Combustion/The Combustion Institute, pages 475–488, 1988.
- [8] R. W. Bilger, M. B. Esler, and S. H. Starner. On reduced mechanisms for methane-air combustion. In Mitchell D. Smooke, editor, *Reduced Kinetic Mechanisms and Asymptotic Approximations for Methane-Air Flames*, volume 384, chapter 5, pages 86–110. Springer-Verlag, 1990.
- [9] R. B. Bird, W. E. Stewart, and E. N. Lightfoot. *Transport Phenomena*. Wiley, New York, 1960.
- [10] Linda G. Blevins and Jay P. Gore. Computed structure of low strain rate partially premixed ch₄/air counterflow flames: Implications for no formation. Combustion and Flame, 116:546–566, 1999.
- [11] C.T. Bowman, R.K. Hanson, Jr. D.F. Davidsonand W.C. Gardiner, V. Lissianski, G.P. Smith, D.M. Golden, M. Frenklach, and M. Goldenberg. Gri-mech 2.11. Technical report. Gas Research Institute.

- [12] S. D. Burke and T. E. W. Schumann. Ind. Eng. Chem., 20:S. 998, 1928.
- [13] M. H. Carpenter. A high-order compact numerical algorithm for supersonic flow. In K. W. Morton, editor, Twelfth International Conference on Numerical Methods in Fluid Dynamics, volume 371 of Lecture Notes in Physics, pages 254– 258. Springer-Verlag, 1990.
- [14] W.-C. Chang and J.-Y. Chen. Reduced mechanisms based on gri-mech 1.2.
- [15] J-Y. Chen and R. W. Dibble. Application of reduced chemical mechanisms for prediction of turbulent nonpremixed methane jet flames. In Mitchell D. Smooke, editor, *Reduced Kinetic Mechanisms and Asymptotic Approximations for Methane-Air Flames*, volume 384, chapter 9, pages 193–226. Springer-Verlag, 1990.
- [16] B. Cuenot and T. Poinsot. Effects of curvature and unsteadiness in diffusion flames, implications for turbulent diffusion combustion. Twenty-Fifth Symposium (International) on Combustion/The Combustion Institute, 1994.
- [17] Pascale Domingo, Luc Vervisch, and Ken Bray. Partially premixed flamelets in les of nonpremixed turbulent combustion. *Combust. Theory Modelling*, 6:529–551, 2002.
- [18] C. G. Fotache, T. G. Kreutz, and C. K. Law. Ignition of counterflowing methane versus heated air under reduced and elevated pressures. *Combust. Flame*, 108:442, 1997.
- [19] M. Frenklach, H. Wang, C.-L. Yu, M. Goldenberg, C.T. Bowman, R.K. Hanson, D.F. Davidson, E.J. Chang, G.P. Smith, D.M. Golden, W.C. Gardiner, and V. Lissianski. Gri-mech—an optimized detailed chemical reaction mechanism for methane. Technical Report GRI-95/0058, Gas Research Institute, November 1995.
- [20] R. Hilbert, F. Tap, H. El-Rabii, and D. Thévenin. Impact of detailed chemistry and transport models on turbulent combustion simulations. *Progress in Energy and Combustion Science*, 30:61–117, 2004.
- [21] J. O. Hirscfelder, C. F. Curtiss, and R. B. Bird. Molecular Theory of Gases and Liquids. Wiley, New York, 1954.
- [22] F. A. Jaberi and S. James. Effects of chemical reaction on two-dimensional turbulence. *Journal of Scientific Computing*, 14(1):31–71, 1999.
- [23] R. J. Kee, G. Dixon-Lewis, J. Warnatz, M. E. Coltrin, and J. A. Miller. A fortran computer code package for the evaluation of gas-phase multi-component transport properties. Technical Report SAND86-8246, Sandia National Laboratories, 1986.

- [24] R. J. Kee, F. M. Rupley, and J. A. Miller. Chemkin-II: A fortran chemical kinetics package for the analysis of gas-phase chemical kinetics. Technical Report SAND89-8009B, Sandia National Laboratories, 1989.
- [25] C. A. Kennedy and M. H. Carpenter. Comparison of several numerical methods for simulation of compressible shear layers. Technical Report 3484, NASA, December 1997.
- [26] J. S. Kim, P. A. Libby, and F. A. Williams. On the displacement effects of laminar flames. *Combust. Sci. Technol*, 87:1–25, 1992.
- [27] A.Y. Klimenko and R.W. Bilger. Conditional moment closure for turbulent combustion. *Progress in Energy and Combustion Science*, 25(6):595-687, 1999.
- [28] C. K. Law, D. L. Zhu, T. X. Li, S. H. Chung, and J. S. Kim. Combsution Science and Technology, 64:199-232, 1989.
- [29] A. Liñán. The asypmtotic structure of counterflow diffusion flames for large activation energies. *Acta Astronaut.*, 1:1007–1039, 1974.
- [30] A. E. Lutz and R. J. Kee. A fortran program for computing opposed-flow diffusion flames. Technical Report SAND96-8243, Sandia National Laboratories, 1996.
- [31] Ulrich Maas and Dominique Thévenin. Correlation analysis of direct numerical simulation data of turbulent non-premixed flames. Twenty-Seventh Symposium (International) on Combustion/The Combustion Institute, pages 1183–1189, 1998.
- [32] S. Mahalingam, J. H. Chen, and L. Vervisch. Finite-rate chemistry and transient effects in direct numerical simulation of turbulent nonpremixed flames. *Combustion and Flame*, 102:285–297, 1995.
- [33] H. P. Mallampalli, T. H. Fletcher, and J. Y. Chen. Evaluation of ch4/nox global mechanisms used for modeling lean premixed turbulent combustion of natural gas. Fall Meeting of the Western States Section of the Combustion Institute, October 1996.
- [34] L. Monchick and E. A. Mason. Journal of Chemical Physics, 35:1676, 1961.
- [35] N. Peters. Laminar diffusion flamelet models in non-premixed turbulent combustion. *Prog. Energy Combust. Sci.*, 10:319-339, 1984.
- [36] N. Peters. Partially premixed diffusion flamelets in non-premixed turbulent combustion. *Twentieth Symposium on Combuttion/The Combutton Institute*, pages 353-360, 1984.
- [37] N. Peters. Laminar flamelet concepts in turbulent combustion. Twenty-First Symposium on Combution/The Combution Institute, pages 1231–1250, 1986.

- [38] N. Peters. Reduced mechanisms. In Mitchell D. Smooke, editor, Reduced Kinetic Mechanisms and Asymptotic Approximations for Methane-Air Flames, volume 384, chapter 3, pages 48-67. Springer-Verlag, 1990.
- [39] N. Peters and B. Rogg, editors. Reduced Mechanisms Mechanisms for Applications in Combustion Systems, volume 15 of Lecture Notes in Physics. Springer-Verlag, 1993.
- [40] N. Peters and F. A. Williams. The asymmtotic structure of stoichiometric methane-air flames. *Combust. Flame*, 68:185, 1987.
- [41] T. Poinsot, S. Candel, and A. Trouve. Applications of direct numerical simulations to premixed turbulent combsution. *Progress in Energy and Combustion Science*, 21:531-576, 1996.
- [42] T. Poinsot and S. Lele. Boundary conditions for direct simulations of compressible viscous flows.
- [43] T. Poinsot and L. Vervisch. *Theoretical and Numerical Combustion*. R. T. Edwards, Philadelphia, PA, 2001.
- [44] S. B. Pope. Pdf methods for turbulent reactive flows. *Progress in Energy and Combustion Science*, 11:119–192, 1985.
- [45] Stephen B. Pope. *Turbulent Flows*. Cambridge University Press, Cambridge, UK, 2000.
- [46] J. E. Rehm and N. T. Clemens. The relationsip between vorticity/strain and reaction zone structure in turbulent non-premixed jet flames. Twenty-Seventh Symposium (International) on Combustion/The Combustion Institute, pages 1113–1120.
- [47] B. Rogg, F. Behrendt, and J. Warnatz. Turbulent non-premixed combustion in partially premixed diffusion flamelets with detailed chemistry. *Twenty-First Symposium on Combution/The Combution Institute*, pages 1533-1541, 1986.
- [48] D. Rudy and J. Strikwerda. Boundary conditions for subsonic compressible navier-stokes calculations. *Computers and Fluids*, 1981.
- [49] K. Seshadri and F. A. Williams. Laminar flow between parallel plates with injection of a reactant at high reynolds number. *Int. Journal of Mass and Heat Transfer*, pages 21–251, 1978.
- [50] Gregory P. Smith, David M. Golden, Michael Frenklach, Nigel W. Moriarty, Boris Eiteneer, Mikhail Goldenberg, C. Thomas Bowman, Ronald K. Hanson, Soonho Song, Jr. William C. Gardiner, Vitali V. Lissianski, and Zhiwei Qin. Gri-mech 3.0. Technical report, Gas Research Institute.

- [51] M. D. Smooke and V. Giovangigli. Reduced Kinetic Mechanisms and Asymptotic Approximations for Methane-Air Flames, chapter Formulation of the Premixed and Nonpremixed Test Problems, pages 1–28. Number 384 in Lecture Notes in Physics. Springer-Verlag, 1990.
- [52] M. D. Smooke, K. Sheshadri, and I. K. Puri. Twenty-Second Symposium on Combsution/The Combsution Institute, pages 1555-1563, 1988.
- [53] C. J. Sung, C. K. Law, and J-Y. Chen. An augmented reduced mechanism for methane oxidation with comprehensive global parametric validation. *Twenty-sixth Symposium on Combution/The Combution Institute*, 26:295–304, 1996.
- [54] Michael A. Tanoff and Mitchell D. Smooke. The sensitive structure of partialy premixed methane-air vs. air counterflow flames. *Twenty-sixth Symposium on Combution/The Combution Institute*, pages 1121–1128, 1996.
- [55] Luc Vervisch and Thierry Poinsot. Direct numerical simulation of non-premixed turbulent flames. Annu. Rev. Fluid Mech., 30:655-691, 1998.
- [56] Denis Veyante and Luc Vervisch. Turbulent combustion modeling. *Progress in Energy and Combustion Science*, 28:193–266, 2002.
- [57] C. R. Wilke. A viscosity equation for gas mixtures. *Journal of Chemical Physics*, 18:517, 1950.
- [58] F. A. Williams. Turbulent Reacting Flows. Springer-Verlag, 1980.
- [59] F. A. Williams. *Combustion Theory*. The Benjamin/Cummings Publishing Company, Inc, second edition, 1985.
- [60] H. S. Xue and S. K. Aggarwal. Effects of reaction mechanisms on structure and extinction of partially premixed flames. *AIAA*, 39(4):637–645, 2001.
- [61] H. S. Xue, S. K. Aggarwal, R. J. Osborne, T. M. Brown, and R. W. Pitz. Assessment of reaction mechanisms for counterflow methane-air partially premixed flames. *AIAA Journal*, 40(6):1236–1238, 2002. Tecnical Notes.
- [62] I. Yamaoka and H. Tsuji. Sixteenth Symposium on Combsution/The Combsution Institute, pages 1145–1154, 1977.

